Seamless integration of the coastal ocean in global marine carbon cycle modeling

M. Mathis[1], K. Logemann[1], J. Maerz[2], F. Lacroix[3], S. Hagemann[1], F. Chegini[2], L. Ramme[2,4], T. Ilyina[2], P. Korn[2], and C. Schrum[5]

[1]Helmholtz-Zentrum Hereon, Institute of Coastal Systems, Max-Planck-Str. 1, D-21502 Geesthacht
[2]Max-Planck-Institute for Meteorology, Bundesstr. 53, D-20146 Hamburg
[3]Max-Planck-Institute for Biogeochemistry, Hans-Knöll-Str. 10, D-07745 Jena
[4]International Max Planck Research School on Earth System Modelling, Hamburg, Germany
[5]University of Hamburg, Institute of Oceanography, Bundesstr. 53, D-20146 Hamburg

Key Points:

- We introduce the first global ocean-biogeochemistry model with a dedicated representation of coastal carbon dynamics.
- We globally apply a grid refinement in the coastal ocean to better resolve regional circulation features, including ocean-shelf exchange.
- We explicitly incorporate key physical and biogeochemical processes controlling coastal carbon dynamics.

Corresponding author: Moritz Mathis, moritz.mathis@hereon.de

Abstract

We present the first global ocean-biogeochemistry model that uses a telescoping high resolution for an improved representation of coastal carbon dynamics: ICON-Coast. Based on the unstructured triangular grid topology of the model, we globally apply a grid refinement in the land-ocean transition zone to better resolve the complex circulation of shallow shelves and marginal seas as well as ocean-shelf exchange. Moreover, we incorporate tidal currents including bottom drag effects, and extend the parameterizations of the model's biogeochemistry component to account explicitly for key shelf-specific carbon transformation processes. These comprise sediment resuspension, temperature-dependent remineralization in the water column and sediment, riverine matter fluxes from land including terrestrial organic carbon, and variable sinking speed of aggregated particulate matter. The combination of regional grid refinement and enhanced process representation enables for the first time a seamless incorporation of the global coastal ocean in model-based Earth system research. In particular, ICON-Coast encompasses all coastal areas around the globe within a single, consistent ocean-biogeochemistry model, thus naturally accounting for two-way coupling of ocean-shelf feedback mechanisms at the global scale. The high quality of the model results as well as the efficiency in computational cost and storage requirements proves this strategy a pioneering approach for global high-resolution modeling. We conclude that ICON-Coast represents a new tool to deepen our mechanistic understanding of the role of the land-ocean transition zone in the global carbon cycle, and to narrow related uncertainties in global future projections.

Plain Language Summary

The coastal ocean is an area hardly taken into account by current climate change assessment activities. Yet, its capacity in carbon dioxide (CO_2) uptake and storage is crucial to be included in a science-based development of sustainable climate change mitigation and adaptation strategies. Earth system models are powerful tools to investigate the marine carbon cycle of the open ocean. The coastal ocean, however, is poorly represented in global models to date, because of missing key processes controlling coastal carbon dynamics and too coarse spatial resolutions to adequately simulate coastal circulation features. Here, we introduce the first global ocean-biogeochemistry model with a dedicated representation of the coastal ocean and associated marine carbon dynamics: ICON-Coast. In this model, we globally apply a higher resolution in the coastal ocean and extend the accounted physical and biogeochemical processes. This approach enables for the first time a consistent, seamless incorporation of the global coastal ocean in model-based Earth system research. In particular, ICON-Coast represents a new tool to deepen our understanding about the role of the land-ocean transition zone in the global climate system, and to narrow related uncertainties in possible and plausible climate futures.

1 Introduction

Our current understanding about the role of the coastal ocean in the marine carbon cycle is limited and fragmentary. Considerable knowledge gaps are related to the interaction between the diverse sources and sinks of carbon in the highly heterogeneous and dynamic land-ocean transition zone and their relation to the biogeochemical processes in the open ocean (Regnier et al., 2013; Ward et al., 2017; G. G. Laruelle et al., 2018). Under present-day climatic conditions, the global coastal ocean has been identified as a net sink for atmospheric CO_2 (G. Laruelle et al., 2014; Gruber, 2015). However, to what extent coastal areas around the globe are taking up or releasing carbon, as well as how much of the carbon exported from the coastal areas enters the deep ocean, remains unclear (Bauer et al., 2013; Roobaert et al., 2019). The coastal ocean, thus, is a largely missing component of current global carbon budgeting (Fennel et al., 2019; Hauck et al., 2020), yet its capacity in carbon storage and transformation is crucial to be included in a science-based development

of sustainable mitigation and adaptation strategies to global climate change (Nellemann et al., 2009; Schmidt et al., 2017; Luisetti et al., 2020).

The general view is that in coastal areas of middle and high latitudes, net CO_2 drawdown at the sea surface is induced by high biological productivity and an efficient export of sequestered carbon to the adjacent deep open ocean, which outcompetes outgassing in low latitudes driven by temperature effects and substantial terrestrial carbon inputs (Borges & Frankignoulle, 2005; Cai, 2011). However, observation- and model-based estimates of the carbon fluxes across the boundaries of the coastal ocean, determining the overall budget, are poorly constrained. About $2\,\mathrm{Gt\,C\,yr^{-1}}$ uncertainty is associated with the amount of carbon deposited in coastal sediments, with estimates ranging from 0.2-2.2 $\mathrm{Gt\,C\,yr^{-1}}$ (Krumins et al., 2013). This is about the same amount taken up from the atmosphere by the entire global ocean at present (Park et al., 2010; Landschützer et al., 2016). About $1\,\mathrm{Gt\,C\,yr^{-1}}$ uncertainty is associated with the coastal CO_2 flux at the air-sea interface, ranging from 0.1-1.0 $\mathrm{Gt\,C\,yr^{-1}}$ uptake (G. G. Laruelle et al., 2010; Bourgeois et al., 2016), although more recent studies point rather towards the lower end of this spread (Roobaert et al., 2019; Lacroix et al., 2021b). More accurate estimates of coastal carbon fluxes are thus also needed to robustly quantify the anthropogenic perturbation of the global carbon cycle, which is a key diagnostic of the evolution of climate change and the effectiveness of climate policies (Canadell et al., 2010; Friedlingstein et al., 2020).

Observations of processes relevant to constrain uncertainties in coastal carbon dynamics are methodologically challenging. Moreover, their spatial and temporal coverage is still scarce and often biased towards certain regions, latitudes and seasons (Painting et al., 2020; Ward et al., 2020). Recent studies applied machine learning algorithms to close data gaps by extrapolating collinearities between target and proxy observables (Lee et al., 2019; Gregor et al., 2019). The results, though, are often sensitive to the choice of the specific approach.

Global ocean-biogeochemistry models are powerful tools to gain understanding about the functioning of the marine carbon cycle and to test hypotheses about its response to future scenarios following various socio-economic climate policy directions. To investigate the coastal ocean, however, global ocean-biogeochemistry models are faced with conceptual limitations (Ward et al., 2020), mainly due to two circumstances. First, global models are not designed to capture the diverse energetic processes characterizing biogeochemical shelf sea dynamics such as a strong interaction between the water column and the sediment, strong internal mixing, or a strong influence of matter fluxes from land (Fig. 1). Many of these processes are thus typically underrepresented by global biogeochemistry models, if implemented at all (Allen et al., 2010; Hauck et al., 2020). And second, a comparatively high grid resolution is required to adequately resolve shelf-specific processes as well as ocean-shelf exchange. In the shallow coastal ocean, the horizontal mesh spacing necessary to resolve the characteristic length scale of the ocean circulation ranges between 1/16° and 1/50° (Hallberg, 2013).

Setting up a global model with high grid resolution is not a problem in the first place (e.g. Cheng et al., 2016; Z. Li et al., 2017; Hewitt et al., 2020). The study of global carbon dynamics in the context of contemporary increasing atmospheric pCO2, however, requires simulation periods of at least multiple decades or even centuries, irrespective of still much longer spinup simulations needed to drive the physical and biogeochemical state of the ocean into equilibrium. Running a conventional global biogeochemistry model at the desired mesh spacing of 1/16° or higher for several decades, though, is too resource intensive under today's high-performance computing (HPC) capacities, thus excluding this application for practical reasons. Global ocean-biogeochemistry models contributing to the 6th phase of the Coupled Model Intercomparison Project (CMIP6), for example, were run with nominal horizontal mesh spacings of 1/2° to 1° (Séférian et al., 2020). Model-based investigations of the coastal ocean therefore have mainly pursued the application of regional model systems that enable both, specific process adaptation and finescale grid resolution at lower computational costs. Inconsistencies due to the prescribed forcing at the open lateral boundaries, however, can

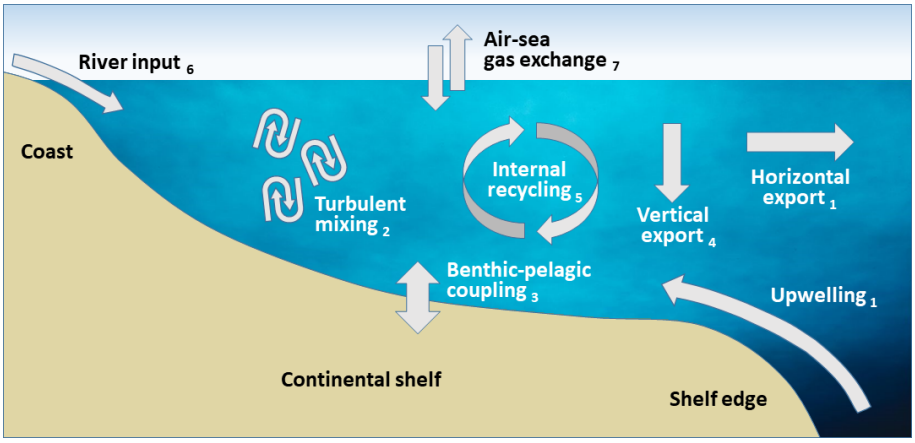

Figure 1: Schematic of key processes controlling coastal carbon dynamics. Attached indices are referred to in the results section 3

lead to spurious artefacts influencing the model results in the interior of the regional domain (Marsaleix et al., 2006; Z. Liu & Gan, 2016; Mathis et al., 2018). Moreover, global budgeting of the coastal ocean requires global coastal coverage, which can hardly be obtained by regional modeling efforts.

In this paper, we present the first global ocean-biogeochemistry model that overcomes these technical barriers of inadequate grid resolution and process representation in the coastal ocean. We build our development on the ocean component ICON-O of the new Earth system model of the Max-Planck-Institute for Meteorology in Hamburg and construct a modified version of this model with a dedicated focus on the land-ocean transition zone: ICON-Coast. For this task, we take advantage of the triangular grid structure of ICON-O and globally apply a regional grid refinement in the coastal ocean. Logemann et al. (2021) have demonstrated a significant improvement of coastal tidal amplitudes simulated with ICON-O when such a regional refinement is used. The advantages of installing variable-resolution grids in global Earth system models to accommodate complex biogeochemical interactions in the terrestrial-aquatic interface were recently emphasized by Ward et al. (2020). Besides, the use of unstructured grids was envisaged the most versatile, efficient and elegant way to improve our understanding of the role of shelf seas in global-scale processes already by Holt et al. (2009). In addition to the regional grid refinement, we incorporate several modifications and extensions of the standard modules of ICON-O, in particular for the biogeochemistry component HAMOCC, to improve the representation of shelf-specific processes related to coastal carbon dynamics (Fig. 1).

The aim of this development is to provide a tool for reducing uncertainties in our understanding of the global carbon cycle and its governing processes via an improved modeling approach. A seamless connection of the open and coastal ocean merged into a global ocean-biogeochemistry model enables a consistent two-way coupling of cross-scale physical and biogeochemical feedback mechanisms in all coastal regions of the world. To lay the grounds for various scientific applications, we here introduce the general concept of ICON-Coast and exemplify the skills and potentials of the model by showing results of simulated physical and biogeochemical key processes related to coastal carbon dynamics.

2 Methods

2.1 Model description of ICON-O

The basis of our development is the global ocean-sea ice-biogeochemistry model ICON-O (Korn, 2017; Korn & Linardakis, 2018; Logemann et al., 2021). The physical core of the model is based on finite volume numerics. The grid structure discretizes the spherical surface of the global ocean by triangular cells with a C-type staggering of variables. The vertical dimension is defined on z coordinates. The primitive equations of fluid motion are solved with applied hydrostatic and Boussinesq approximations. In the setup presented here, the vertical turbulent viscosity and diffusivity are parameterized by a TKE mixing scheme (Gaspar et al., 1990; Gutjahr et al., 2021). Biharmonic operators are used for the velocity closure. Sea ice advection and thermodynamics are included by a coupling with the sea ice model FESIM (Danilov et al., 2015).

The biogeochemistry component of ICON-O is the Hamburg Ocean Carbon Cycle model HAMOCC (Maier-Reimer et al., 2005; Ilyina et al., 2013) in its CMIP6 version (Mauritsen et al., 2019). This version was transferred from the Earth system model MPI-ESM to ICON-O as the ocean component of the upcoming Earth system model ICON-ESM (Jungclaus et al., in prep.). Marine biology dynamics is represented by a NPZD-type approach (Six & Maier-Reimer, 1996). Sequestration of inorganic carbon and nutrients by phytoplankton growth is controlled by light availability, water temperature, and co-limitation of the macro nutrients phosphate and nitrate as well as iron, assuming Redfield stoichiometry (Six & Maier-Reimer, 1996; Kloster et al., 2006). Biogeochemical transformation processes distinguish between oxic, sub- and anoxic conditions, accounting for bacterial decomposition, denitrification, and sulfate reduction. The nitrogen cycle includes a prognostic representation of N-fixation at the sea surface by cyanobacteria (Paulsen et al., 2017). A 3-dimensional sediment module accounts for deposition and dissolution of particulate matter at the sea floor as well as benthic-pelagic pore water exchange (Heinze et al., 1999). In the current setup, tracer advection is calculated by the physical component of the model.

2.2 Model extensions for ICON-Coast

Starting from the model setup described in the previous section, our improvements regarding shelf-specific process representation comprise the incorporation of tidal currents including bottom drag effects, and the implementations of sediment resuspension, temperature-dependent remineralization in the water column and sediment, riverine matter fluxes from land including terrestrial organic carbon, and variable sinking speed of aggregated particulate matter. Because of the diversity of these concepts, brief introductions with respect to their relevance for coastal carbon dynamics are provided in the results section 3 to ease the interpretation of the presented results and the understanding of associated added values.

Tidal currents are used as implemented by Logemann et al. (2021). The tide module accounts for the full luni-solar tidal potential to provide broad frequency tidal dynamics, including non-linear interactions between partial tides. Effects of loading and self-attraction are neglected in this first version of the module.

Sediment resuspension is implemented as described in Mathis et al. (2019). Critical bed shear stresses are calculated from the mean sediment density and grainsize at every time step. The latter are determined by the local sediment composition and the constant density and grainsize assigned to each particle class. The erosion depth is derived from bottom current velocities inducing overcritical bed shear stress. Here, this has been extended to account for mixing of eroded pore water with the tracer concentrations in the bottom layer of the water column, in addition to the erosion and advection of the solid sediment constituents (detritus, opal, calcium carbonate, and dust).

To incorporate a mechanistic representation of the vertical export dynamics of biogenically bound carbon and nutrients from the euphotic zone to the interior of the ocean, we adopted a scheme for marine aggregates following Maerz et al. (2020). The formulation explicitly accounts for the influences of size, microstructure, heterogeneous composition, density, and porosity of marine aggregates on their settling velocities and exposure to biogeochemical transformation processes. Ballasting (biogenic and lithogenic) minerals and particulate organic carbon are tied together, yielding common but variable sinking speeds for all aggregate components.

Water temperature has a non-linear influence on the degradation processes of organic carbon (Yvon-Durocher et al., 2012; Laufkötter et al., 2017; Lønborg et al., 2018) and diatom silica frustules (Hurd, 1972; Dixit et al., 2001; van Cappellen et al., 2002). Together with the explicit representation of marine aggregates, we introduce a consistent temperature dependence for remineralization and dissolution processes of particulate matter. As the aggregated particle compounds in the water column sink with a common settling velocity, they are exposed to a common ambient temperature. Their different degradation length scales, however, interplay in determining e.g. the ballasting and thus the sinking speed (Maerz et al., 2020). In the coastal ocean, this intricate connection between particulate organic carbon and ballasting minerals is especially relevant where deposited matter may become resuspended and transported to distant areas and depths. Also here, we follow Maerz et al. (2020) with a Q10 approach to modify the remineralization rate of detritus and the dissolution rate of opal, and extend this concept to dissolved organic carbon.

Temperature-dependent degradation rates were also reported for the upper sediment, derived from in-situ measurements, diagenetic modeling, and laboratory incubation experiments (Arndt et al., 2013; Franzo et al., 2019). Consistent with the Q10 approach in the water column, we extended the temperature-dependence of the degradation of particulate organic matter and opal to the sediment. Here, we use a Q10 value of 2.3 with a reference temperature of 10 °C for detritus (Provoost et al., 2013) and a Q10 value of 2.3 with reference temperature of 20 °C for opal (Kamatani, 1982; Ridgwell et al., 2002).

River mouths are treated as point sources at individual coastal grid cells, incorporating the work by Lacroix et al. (2020) who investigated the influence of riverine matter fluxes on the preindustrial oceanic CO_2 outgassing with the global Earth system model MPI-ESM. Rivers are discharging prescribed fluxes of fresh water, nutrients, organic and inorganic carbon, and alkalinity. The organic carbon fraction includes terrestrial dissolved organic matter (tDOM), a biogeochemical tracer usually not considered by global models to date (Lacroix et al., 2021b). tDOM is more refractory than oceanic organic matter and has a carbon-to-nutrient ratio that is about 20 times higher (Compton et al., 2000; Aarnos et al., 2018). The tDOM pool in our model is therefore treated with a C:P mole ratio of 2583:1 (Meybeck, 1982; Compton et al., 2000) and a mineralization rate of $0.003\,\mathrm{d}^{-1}$ (Fichot & Benner, 2014) at reference temperature of 10 °C.

All process extensions compared to the standard configuration of HAMOCC (Mauritsen et al., 2019) were individually evaluated during their original developments for the Earth system model MPI-ESM and can be found in the primary references given above, including descriptions of the mathematical formalisms. Our model experiments with ICON-Coast presented here, thus also represent the first simulations where these processes have been consistently integrated in a common ocean-biogeochemistry component.

2.3 Regional grid refinement

The other central concept of ICON-Coast, besides the incorporation of shelf-specific processes, is the application of a regionally refined numerical grid. This is done to resolve shelf sea dynamics more properly, while reducing resource demands compared to simulations with a globally uniform high resolution.

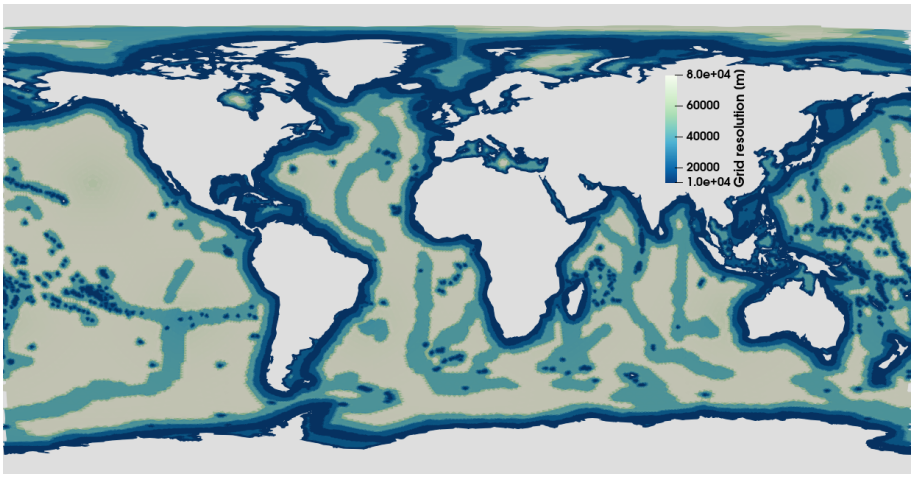

Figure 2: Grid configuration used for the high-res simulations with a horizontal mesh spacing ranging from 80 km in the open ocean to 10 km at the coast lines and continental margins. For the low-res simulations, a qualitatively similar configuration has been used with a horizontal spacing that is coarser by a factor of 2, ranging from 160-20 km

Increasing horizontal resolution is assigned locally according to three geometric criteria (Logemann et al., 2021): decreasing distance to the coast, decreasing water depth, and increasing slope of the bottom topography. By combining these criteria we obtain higher resolution in the near-coastal zones as well as the shallow shelves, broadly including the shelf breaks as the transition to the open ocean. Areas of different resolutions are connected by cell bisection and subsequent local spring optimization to assure smooth grid spacing and avoid critically distorted cell geometries. The grid configuration with maximum resolution used in this study is shown in Fig. 2 (high-res; see section 2.4).

The grid refinement accounts for a more detailed discretization of topographic features in the coastal ocean, enabling a better representation of the general circulation in shelf and marginal seas. In particular, many ocean-shelf exchange mechanisms such as cross-slope bottom transport, instabilities of frontal boundary currents, or eddy-shelf interaction are strongly influenced by ageostrophic processes which can be significantly better resolved by mesoscale grid resolutions (Karakaş et al., 2006; Oguz et al., 2015; Brink, 2016; Graham et al., 2018b; Thévenin et al., 2019; Combes et al., 2021; Kämpf, 2021). Moreover, an increased grid resolution permits the local development of high horizontal temperature and salinity gradients which enhances the baroclinic components of the general circulation. As all biogeochemical tracers in the model are subject to advection, the better representation of the circulation is vital for improving the simulated biogeochemical state of the coastal ocean.

Due to the applied slope criterion, a moderate refinement is also assigned to mid-ocean ridges, seamounts, and submarine banks (Fig. 2). This accounts for a better representation of the abyssal circulation in the open ocean, associated with tidal mixing (Simmons et al., 2004; Dale & Inall, 2015) as well as transport of heat and biogeochemical tracers parallel to the ridge's flanks (Lavelle et al., 2012). Moreover, the capture of bathymetric gaps, such as fracture zones, determines how much deep water can pass between ocean basins and where this exchange occurs (Gille et al., 2004).

The spatial positioning of variables within the numerical grid follows an Arakawa C-grid staggering, with scalar variables at the cell centre and normal components of the velocity vector at cell boundaries. This staggering type is numerically advantageous. For triangular cells, however, it is associated with spurious discontinuities in the divergence field of the

horizontal flow (Stuhne & Peltier, 2009; Danilov, 2010). To overcome this problem, the discretization of the primitiv equations of fluid motion is based on a novel technique developed by Korn (2017), which provides an efficient way to control divergence noise without violating conservation conditions. The numerical stability of strongly irregular grids as used in our simulations was demonstrated by Logemann et al. (2021), who conducted comprehensive test simualtions with the core model ICON-O.

2.4 Experiment design

In this paper, we show results from two ICON-Coast simulations with different horizontal grid configurations. The first one spans a mesh spacing of 160-20 km (low-res) and has been run in coupled physics-biogeochemistry mode. The resolution of the second configuration is higher by a factor of 2, spanning a mesh size of 80-10 km (high-res; Fig. 2), and has been run in physics-only mode to assure reasonable simulation progress and computational cost. The advantage of including the high-res simulation, albeit in a light version, is that we can better demonstrate the benefit of a regional grid refinement for the representation of relevant hydrodynamic features in the coastal ocean that provide the background conditions for the biogeochemical processes. In particular at the upper end of the resolution range (mesh size 10 km), we reach or come close to the first baroclinic radius of deformation in many shelf seas and ocean-shelf transition zones, thus incorporating mesoscale activity more extensively than in the low-res simulation (Hallberg, 2013; Hewitt et al., 2017). Representing the mesoscale explicitly was shown to tangibly improve the simulated mean ocean state as well as the temporal variability (Hewitt et al., 2020). For both grid configurations, the vertical dimension is resolved by 40 layers with a surface layer thickness of 16 m, a layer thickness of 10 m in the remaining upper 100 m of the water column, and increasing thicknesses below. The high surface layer thickness is necessary in this model setup to allow for critical tidal amplitudes and sea ice formation, as a wetting-drying algorithm is not yet included. Internal model time steps are 400 s for the low-res and 100 s for the high-res setups.

The simulations were driven with ERA-Interim reanalysis data (Dee et al., 2011) of 6-hourly atmospheric forcing fields for the period 1990-2010. River runoff data are taken from a hindcast reconstruction by the global hydrological discharge model HD (Hagemann & Dümenil-Gates, 2001) for the period 1979-2009 and applied as monthly climatological means. The hindcast was generated by applying the HD model (vs. 1.10) to a simulation of the land surface scheme JSBACH (Ekici et al., 2014) forced by bias corrected ERA-Interim data (Hagemann et al., 2020). Lateral discharge fluxes were calculated globally at 0.5° resolution and comprise about 2000 catchments areas. Riverine inputs of DIP, DIN, DSi, DFe, DIC, Alk, tDOM (terrestrial dissolved organic matter) and POM are derived from Lacroix et al. (2020, 2021b) for about 850 rivers under 1980-2010 conditions (Table 1). In these studies, historical river loads for the period 1905-2010 were reconstructed based on a hierarchy of weathering and terrestrial organic matter export models as well as the global data set NEWS2 (Seitzinger et al., 2010). Non-weathering sources of nutrients, C and Alk from fertilizer, sewage, and allochthonous inputs were also considered.

Both simulations, low-res and high-res, were initialized by temperature and salinity fields taken from the 0.25° resolution World Ocean Atlas 2013 data set (Locarnini et al., 2013; Zweng et al., 2013) and an ocean at rest. Because of high computational resource demands, we so far have only performed comparatively short simulations of maximum 20 consecutive years. The biogeochemical initial state of the low-res run was therefore taken from previous test and calibration runs in order to reduce effects of long-term drift as much as possible. As the process extensions for HAMOCC were done consecutively, we originally started from the biogeochemical state of the year 1979, simulated by the CMIP6 version of MPI-ESM-LR (Mauritsen et al., 2019), and continued until the year 2010 with several repetitions of intermittent periods to adjust new biogeochemical parameters. To apply this strategy, we could not yet account for contemporary increasing atmospheric pCO_2 but used

Table 1: River inputs for the period 1981-2010 used in the presented ICON-Coast simulations as derived by Lacroix et al. (2020, 2021b), and contemporary observation- and model-based estimates from literature.

Compounds	**ICON-Coast**	**Contemporary estimates**	**References**
DIP [Tg P yr^{-1}]	1.2	0.8-1.4	Meybeck (1982); Compton et al. (2000); Seitzinger et al. (2010)
DIN [Tg N yr^{-1}]	17.6	12-19	Meybeck (1982); Seitzinger et al. (2010)
DSi [Tg Si yr^{-1}]	328	170-490	Beusen et al. (2009); Dürr et al. (2011); Tréguer & De La Rocha (2013); Tréguer et al. (2021)
DIC/Alk [Tg C of HCO_3^- yr^{-1}]	370	260-550	Berner et al. (1983); Amiotte Suchet & Probst (1995); Hartmann et al. (2009); M. Li et al. (2017)
DOM [Tg C yr^{-1}]	216	130-240	Meybeck & Vörösmarty (1999); Seitzinger et al. (2010); M. Li et al. (2019)
POM [Tg C yr^{-1}]	115	100-230	Meybeck & Vörösmarty (1999); Seitzinger et al. (2010); Galy et al. (2015)

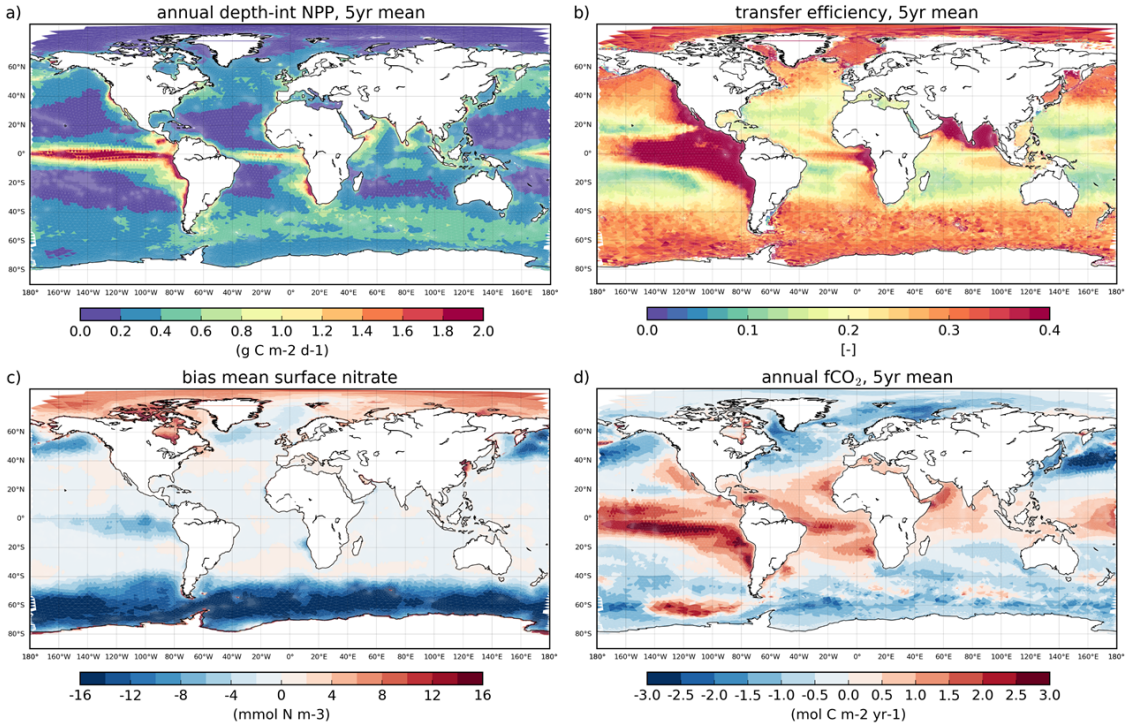

Figure 3: Global distributions of simulated annual depth-integrated net primary production (a), transfer efficiency of organic carbon to the deep ocean (1000 m, b), bias in surface nitrate concentration (c), and ocean-atmosphere CO_2 flux (d), obtained from ICON-Coast with low-res configuration. Positive values in (d) refer to oceanic outgassing.

a constant preindustrial level of 278 ppm. The simulated CO_2 fluxes at the sea surface are thus expected to be biased towards weaker uptake and stronger outgassing compared to observational products of the recent past. The results shown here finally stem from a repetition of the period 2000-2010, where no model parameters have been adjusted further. While being aware of associated limitations, with this approach we aim for a first-order understanding of the added value of the global coastal setup and resulting dynamics therein.

3 Results

3.1 Global biogeochemical patterns

Simulated global patterns of net primary production, transfer efficiency, nutrient concentrations (biases), and ocean-atmosphere CO_2 flux are shown in Fig. 3. The general distributions reflect the persistent large-scale features and global patterns known from observational products and global ocean-biogeochemistry models.

High biological productivity in the open ocean is linked to favorable light conditions and continuous or seasonal nutrient supply to the euphotic zone via upwelling or deep mixing. Thus, enhanced primary production is found in the equatorial Pacific, the eastern upwelling areas, and the subpolar gyres, whereas the oligotrophic subtropical gyres are substantially less productive throughout the year (Fig. 3a; Boyd et al., 2014; Kulk et al., 2020). In the Arctic Ocean, phytoplankton growth is generally weak due to the sea ice cover and limited light availability (Randelhoff et al., 2020). In the greater Arctic (north of the polar circle), ICON-Coast simulates a mean productivity of $32\,\mathrm{g\,C\,m^{-2}\,yr^{-1}}$, which is underestimated compared to 36-39 $\mathrm{g\,C\,m^{-2}\,yr^{-1}}$ estimated from model experiments and remote sensing products by Terhaar et al. (2021) and K. R. Arrigo & van Dijken (2015),

respectively. As largest deviations are found in the coastal ocean, the lower productivity might be attributed to terrestrial nutrient supply from coastal erosion, which sustains around 20% of Arctic net primary production (Terhaar et al., 2021), but is not yet taken into account in the simulations presented here. The simulated global net primary production amounts to 49-52 $\mathrm{Gt\,C\,yr^{-1}}$ (min-max during the simulation period) with a positive drift of about 0.09 $\mathrm{Gt\,C\,yr^{-1}}$ (derived from linear regression). Contemporary observation-based estimates range between 39-58 $\mathrm{Gt\,C\,yr^{-1}}$ (Buitenhuis et al., 2013; Richardson & Bendtsen, 2019; Kulk et al., 2020) and model results show a wide spread of 20-80 $\mathrm{Gt\,C\,yr^{-1}}$ (Laufkötter et al., 2015; Séférian et al., 2020). Compared to MPI-ESM, which was run with the standard version of HAMOCC, our simulated large-scale structures in the open ocean basins are rather similar (Fig. A2a).

The simulated global export of organic matter out of the euphotic zone is 8.0 $\mathrm{Gt\,C\,yr^{-1}}$ and is comparable to the particle flux of 9.1 $\mathrm{Gt\,C\,yr^{-1}}$ derived from data assimilation by DeVries & Weber (2017). The amount of carbon reaching the deep ocean is influenced by the variable sinking speed of aggregated organic and mineral particles. Another critical parameter is the temperature dependence of the compound's degradation rates, as it determines the sensitivity of aggregates to extensive biogeochemical transformation. The strong temperature gradients in the upper ocean across latitudes and seasons thus promote spatially and temporally heterogeneous recycling rates and export fluxes, with maximum ranges being observed in the shallow coastal areas (Guidi et al., 2015; Xie et al., 2019). The combination of the aggregate sinking scheme and temperature-dependent degradation processes applied in ICON-Coast has been shown to induce a global shift in the vertical carbon transfer to the deep ocean towards the poles (Maerz et al., 2020), which is also simulated by ICON-Coast (Fig. 3b). In particular the temperature influence promotes shallower remineralization at low latitudes and deeper remineralization at high latitudes (Laufkötter et al., 2017), enabling the reproduction of latitudinal characteristics of the POC transfer efficiency investigated by Weber et al. (2016) and DeVries & Weber (2017). In addition, the transfer efficiency is regionally modulated by low oxygen concentrations, leading in our model to maximum values exceeding 50% in the oxygen minimum zone of the Equatorial Tropical Pacific. The simulated values, however, are generally overestimated, with a minimum of about 10% transfer efficiency in the subtropical gyres and about 30% in high latitudes, compared to 5% and 25% estimated from inverse modeling of phosphate fluxes by Weber et al. (2016), respectively.

Surface nutrient concentrations show low biases in most ocean basins compared to World Ocean Atlas 2018 Boyer et al. (2018). A mismatch, though, can be seen in the Southern Ocean with deviations of about -14 $\mathrm{mmol\,N\,m^{-3}}$, -0.8 $\mathrm{mmol\,P\,m^{-3}}$, and +20 $\mathrm{mmol\,Si\,m^{-3}}$ in annual mean nitrate, phosphate and silicate concentrations, respectively (Fig. 3c and Fig. A1). Besides, nitrate concentrations are slightly too high in the Arctic. The spatial structures of these biases are also prominent features of the previous HAMOCC implementation in MPI-ESM and have been linked to coarse grid resolution, overestimated vertical velocities, and too low iron limitation (Ilyina et al., 2013). In the Southern Ocean, though, nutrient biases are generally less pronounced in MPI-ESM (Fig. A2b and Müller et al., 2018).

Regarding surface CO_2 fluxes, low latitudes are dominated by strong outgassing in particular in upwelling areas, with maximum net fluxes in the equatorial Pacific (Park et al., 2010; Landschützer et al., 2016). Middle and high latitudes, by contrast, function as net sinks for atmospheric CO_2, governed by surface cooling and high seasonal biological export production. The spatial distribution and zonal averages of simulated fCO_2 (Fig. 3d and Fig. 4) qualitatively capture these latitudinal characteristics, e.g. as derived from field measurements of the recent past (Takahashi et al., 2009; Landschützer et al., 2016; Bushinsky et al., 2019). Deviations lie well within the model spreads of CMIP5/6 (Séférian et al., 2020) and the Global Carbon Project (Hauck et al., 2020), with our model showing biases of overestimated outgassing in low latitudes and underestimated outgassing in the Southern Ocean. The global integral amounts to 0.1-0.2 $\mathrm{Gt\,C\,yr^{-1}}$ outgassing with a negative drift

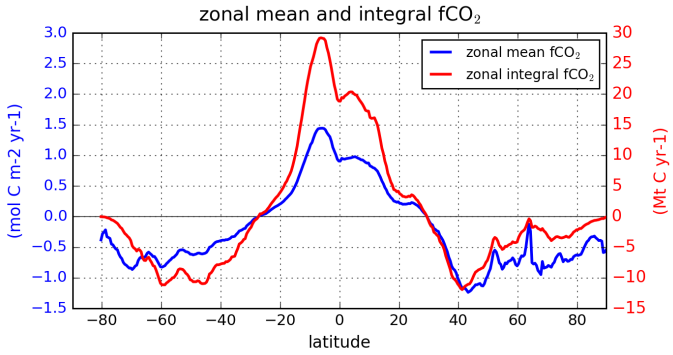

Figure 4: Zonally averaged (blue) and integrated (red) ocean-atmosphere CO_2 flux, simulated with low-res configuration. Positive values refer to oceanic outgassing.

of about -0.03 $\mathrm{Gt\,C\,yr^{-2}}$. Note that the observed contemporary global uptake in the order of 2 $\mathrm{Gt\,C\,yr^{-1}}$ is not met because we have run ICON-Coast with constant preindustrial pCO_2 in the atmosphere (section 2.4), thus approaching equilibrium conditions with net surface CO_2 fluxes driven by river inputs. The oceanic uptake signal due to historical rising atmospheric pCO_2 alone was estimated 1.7 $\mathrm{Gt\,C\,yr^{-1}}$ (during 1905-2010) in a model sensitivity experiment by Lacroix et al. (2021b). A more accurate quantification, however, would require consistent transient ICON-Coast simulations initialized by an equilibrated ocean state at preindustrial conditions.

In general, the main biogeochemical features of the global open ocean are reasonably well represented, in particular compared to earlier model studies. It is thus worth turning the emphasis to the core of ICON-Coast, the coastal and shelf sea regions, to assess the added value of the presented approach.

3.2 Shelf sea dynamics

The primary motivation behind the development of ICON-Coast is to improve the traditional global modeling approach by enabling a better representation of coastal and shelf sea carbon dynamics (Fig. 1). The added value of ICON-Coast, thus, has to be assessed mainly by comparison to conventional ocean-biogeochemical models in capturing the general ranges and orders of magnitue of key biogeochemical parameters in the coastal ocean. We therefore directly compare our results to the global Earth system model MPI-ESM, which used the standard version of HAMOCC (Mauritsen et al., 2019), and verify remaining biases against available observations and regional modeling studies. In particular, we focus on three temperate coastal regions that share the large influence of tidal currents but differ through their embedding in the large-scale ocean circulation (Fig. 5): the Northwest European Shelf (NWES), the Patagonian Shelf (PS), and the East China Shelf (ECS). The NWES is connected to the eastern boundary current system of the North Atlantic subpolar gyre (SPG). The physical and biogeochemical characteristics of water masses flushing the shelf are strongly influenced by the strength of the SPG and the wintertime mixed layer depth in the Northeast Atlantic (Hátún et al., 2017; Koul et al., 2019). The PS is connected to the Antarctic Circumpolar Circulation (ACC) passing through the Drake Passage, and the northward flowing Malvinas Current (MC) branching off the ACC. Shelf water mass characteristics are modulated by the inflow of Subantarctic water and shelf break upwelling induced by the variability of the MC (Combes & Matano, 2018). The ECS is connected to the western boundary current of the North Pacific subtropical gyre. The water masses of this shelf sea mainly originate from the Kuroshio Current and are strongly influenced by the strength of the Yellow Sea Warm Current branching from the Kuroshio Current during

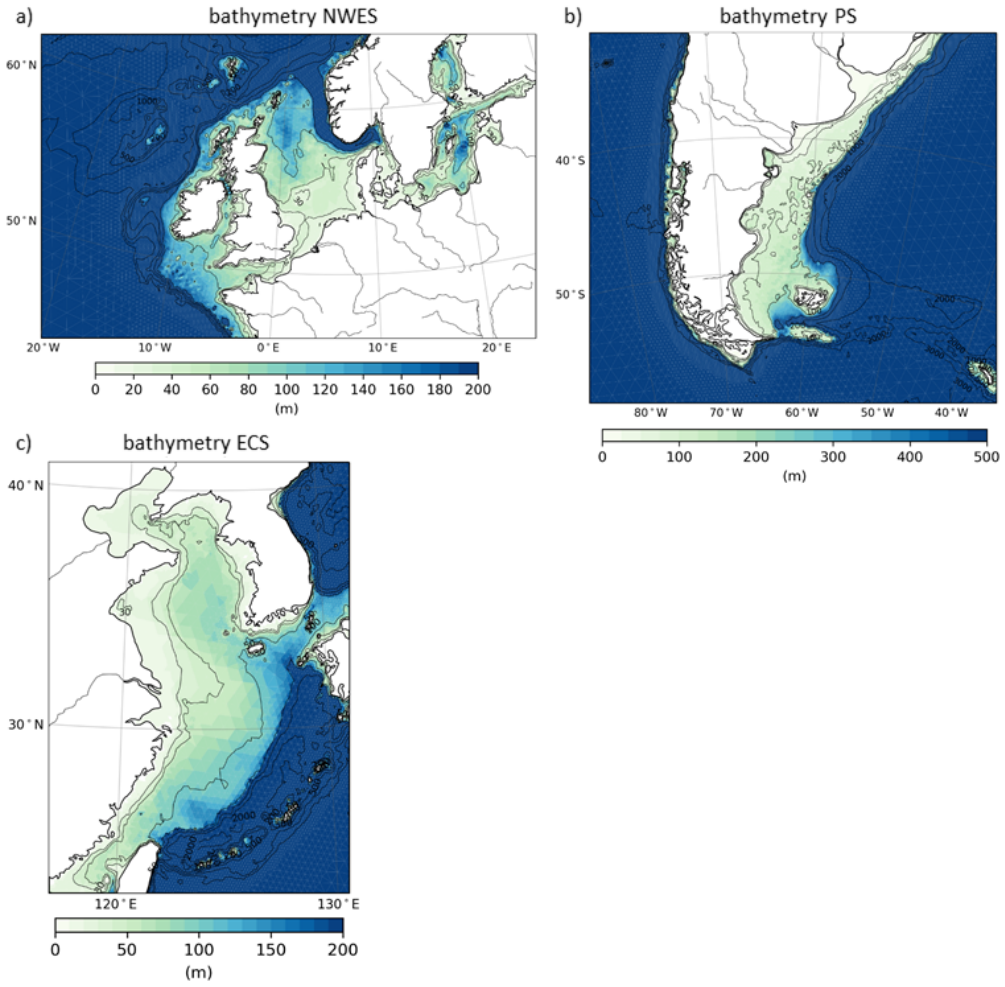

Figure 5: Model bathymetry of the Northwest European Shelf (a), Patagonian Shelf (b) and East China Shelf (c). Isobaths correspond to water depths of 30, 50, 100, 200, 500, 1000, 2000, and 3000 m.

boreal winter (Yuan et al., 2008; Lie & Cho, 2016). All three shelf regions are known to be net sinks for atmospheric CO_2 under present-day climatic and environmental conditions, driven by high biological carbon sequestration and an efficient export of respiratory CO_2 to the adjacent deep ocean (e.g. Becker et al., 2021; Kahl et al., 2017; Jiao et al., 2018). Moreover, they are subject to a strong seasonality of both the atmospheric forcing and the response of the physical and biogeochemical conditions in the ocean, and were extensively investigated by observational and regional modeling studies. These shelf areas thus serve as pivotal regions to test and evaluate our new model implementations.

In general, we show results of biogeochemical parameters from the low-res simulation but physical parameters from the high-res simulation (see section 2.4). This is done to best emphasize the potentials of ICON-Coast in regional high-resolution modeling at the global scale, as well as to demonstrate the ability of the model to simulate key processes of marine coastal carbon dynamics. Differences between high-res and low-res physics are discussed in section 4. The following examples given for the three focus regions are monthly, seasonal, or annual means over the last 5 years of our simulations, that is 2006-2010. These results are opposed to the ensemble mean over 10 realizations of the same period simulated by the Earth system model MPI-ESM (Mauritsen et al., 2019) in low-resolution version (LR) as it contributed to CMIP6. This model has a nominal mesh size in the ocean of 1.4° and

thus a resolution which is comparable to the coarsest parts in the open ocean of the low-res ICON-Coast grid. Furthermore, MPI-ESM hosts the standard version of HAMOCC prior to the process extensions made here. In this comparison, we thus demonstrate the added value gained from a model extension towards a process-oriented and integrative representation of the coastal ocean. Nevertheless, MPI-ESM has also been run at a higher horizontal resolution with a mesh size of 0.4° (HR, Müller et al., 2018). For the evaluation of the coastal circulation and transport rates, we therefore also compare to results from MPI-ESM-HR.

3.2.1 General circulation

The general circulation of shelf seas governs the advective export of sequestered carbon from the coastal to the open ocean as well as the import of nutrient-rich water masses from deeper levels via shelf break upwelling and vertical mixing (Fig. 1 index 1; Painter et al., 2016; Legge et al., 2020; Luisetti et al., 2020). The circulation in the proximal coastal zone determines the distribution of river discharge and nutrient loadings in the inner shelf areas, as the position of river plumes is typically more sensitive to the wind direction than to the river outflow variability (Pimenta et al., 2005; Kastner et al., 2018; Kerimoglu et al., 2020). The strength and structure of the general circulation therefore sensitively influences the residence times of imported water masses on the shelves, and hence the local physical and biogeochemical water mass characteristics (Pätsch et al., 2017; X. Liu et al., 2019; Lacroix et al., 2021a). A proper representation of the general circulation is thus key for investigating coastal carbon dynamics and constraining budget uncertainties.

On the NWES, the simulated mean circulation shows all characteristic features of the well-studied North Sea circulation (Fig. 6a). The pathways of the Fair-Isle Current, East-Shetland Flow, the inflow along the western side of the Norwegian Trench which recirculates in the Skagerrak and leaves the North Sea via the Norwegian Coastal Current, the Dooley Current, and the weak cyclonic circulation in the southern North Sea (Holt & Proctor, 2008; Sündermann & Pohlmann, 2011) can be well identified. The irregularities in the south-western area are probably related to influences of interannual variability in the inter-gyre region on the shown 5-yr mean. Transport rates of prominent North Sea sections are evaluated in Table 2. In the shown high-res configuration, the net transport through the North Sea simulated by ICON-Coast varies between 1.6-1.8 Sv and lies within the range of 0.9-2.3 Sv found in the literature (Mathis et al., 2013; Quante et al., 2016; Pätsch et al., 2017). In the low-res version, the circulation pattern is rather similar (Fig. A4), while in MPI-ESM the structure of the circulation is underrepresented and the transports through several sections are too weak (Fig. A5 and Table 2).

The circulation on the PS is more homogeneous than on the NWES (Fig. 6b). Part of the Cape Horn Current turns onto the shelf between the South American mainland and the Falkland Islands and generally flows northward to meet the La Plata river plume and the Brazil Malvinas Confluence (Combes & Matano, 2018). The inflow of the Cape Horn Current to the shelf is about 2.5 Sv simulated by ICON-Coast and has been quantified by a high-resolution regional model study to about 1.7 Sv (Guihou et al., 2020). This is a reasonable agreement, assuming similar variability and uncertainty ranges as for the well-studied NWES. Also here, MPI-ESM shows distinctly lower transport rates of 1.1 Sv in LR (Fig. 6d) and 0.6 Sv in HR.

On the ECS, distinct seasonal circulation patterns are driven by the characteristic monsoon wind regimes. In winter, the Yellow Sea Warm Current branches from the Kuroshio Current and flows northward into the Bohai Sea (R. Wu et al., 2016). This ECS inflow is balanced by the southward flowing Korean and Chinese coastal currents. In summer, the whole pattern changes into a cyclonic recirculation through the entire Yellow Sea and Bohai Sea (Zhu et al., 2015). ICON-Coast is able to capture the main features of this marked seasonality with great detail (Fig. 7). We can even identify the anticyclonic circulation in the northern part of the Bohai Sea in winter and its cyclonic turn in summer (Yang et al.,

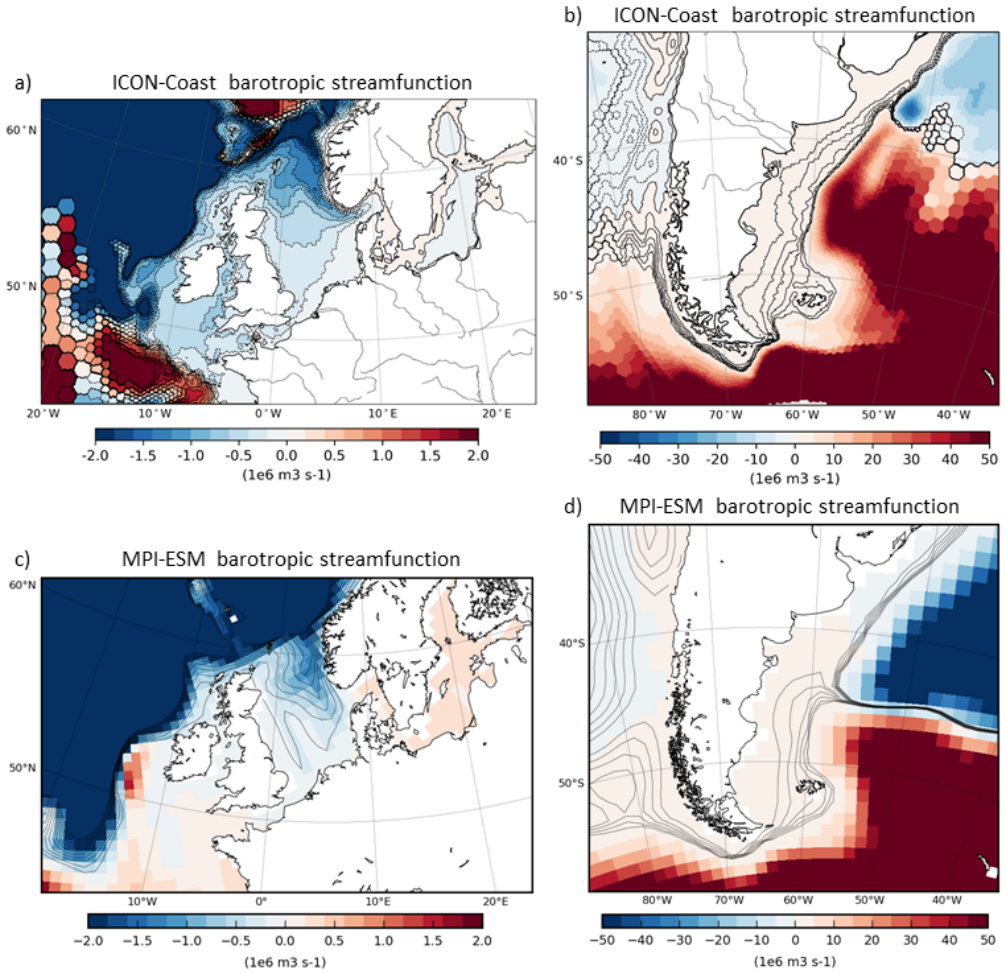

Figure 6: Annual mean barotropic stream function on the Northwest European Shelf (a,c) and Patagonian Shelf (b,d), simulated with ICON-Coast high-res configuration (a,b) and MPI-ESM-LR (c,d). Increments of shown streamlines are 0.2 Sv for (a,c) and 0.5 Sv for (b,d). Hexagonal structures in (a,b) emerge from the calculation and mapping of net volume fluxes through the triangular grid cells.

Table 2: Volume transports ($10^6\,m^3\,s^{-1}$) through selected transects in the North Sea simulated by ICON-Coast, MPI-ESM as well as estimates from observational products and regional model systems presented in Pätsch et al. (2017), Mathis et al. (2013) and references therein. Identifiers in brackets refer to the section descriptions used in Pätsch et al. (2017). Missing values for the Skagerrak recirculation in MPI-ESM indicate that this circulation feature is not captured by the model.

North Sea section	**ICON-Coast low-res/high-res**	**MPI-ESM LR/HR**	**Observ.**	**Reg. model spread**
Fair-Isle inflow (S1)	0.5/0.3	0.2/0.4	0.3-0.7	0.4-0.6
Inflow at 60°N	0.8/0.7	0.8/0.4	0.6-1.5	0.2-1.1
Outflow at 60°N	1.6/1.4	1.0/0.9	1.0-2.3	0.4-1.3
Skagerrak recirculation (S10)	0.6/0.8	-/-	0.5-1.5	0.4-1.7
Jutland Current (S8)	0.28/0.20	0.33/0.04	-	0.19-0.33
English Channel (S6)	0.11/0.18	0.01/0.10	0.06-0.17	0.01-0.15

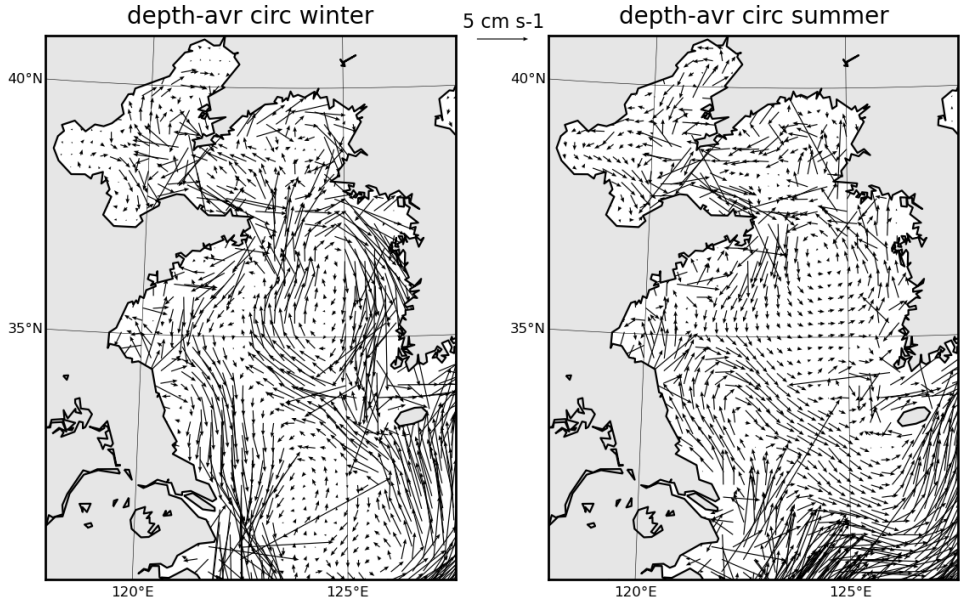

Figure 7: Depth-averaged current velocities on the East China Shelf for winter (left) and summer (right), simulated with high-res configuration.

2019). The throughflow of the Taiwan and Tsushima Straits act as the origination and destination of the mean ECS circulation, respectively (Z. Liu, Gan, et al., 2021). The mean transport rate in the Taiwan Strait is simulated 1.3 Sv, with observations ranging between 1.3-2.0 Sv and a regional modeling spread of 0.4-2.3 Sv (J. Hu et al., 2010; H. W. Chen et al., 2016; Z. Liu, Gan, et al., 2021). The main outflow through the Tsushima Strait into the Sea of Japan seems underestimated, with a simulated tranport of 1.8 Sv and observations of about 2.6 Sv (Z. Liu, Gan, et al., 2021). The region of coastal water diluted by the Yangtze river (salinity less than 28) mainly spreads eastward and northward into the East China and Yellow Seas with a maxium extension to about 123°E and 35°N in summer, in good agreement with 124°E and 35°N during Jul/Aug 1998-2010 derived from remote sensing by Bai et al. (2014). For the ECS we abstain from a correlate of Fig. 7, as in MPI-ESM-LR the entire region is covered by only a dozen grid cells (see e.g. Fig. 9). In MPI-ESM-HR, the ECS is resolved with a mesh spacing of about 45 km (larger than ICON-Coast by a factor of 2.2 for low-res and 4.5 for high-res), which is still too coarse to capture the circulation features shown in Fig. 7.

3.2.2 Tidal waves

The most energetic flows in the coastal ocean are generated by tidal waves, with maximum current speeds exceeding 60 cm/s twice a day (Poulain & Centurioni, 2015). The interaction with the topography in shallow areas induces energy dissipation via bottom friction and leads to high bed shear stresses and turbulent mixing in the water column (Fig. 1 index 2; Wilson & Heath, 2019). These effects are known to play an important role in the coastal nutrient and carbon dynamics (Cadier et al., 2017; Zhao et al., 2019).

In our model, tidal waves are calculated from the full luni-solar tidal potential. As shown by Logemann et al. (2021), who have run variable-resolution grids with ICON-O, the simulated amphidromic patterns as well as tidal amplitudes for both the open ocean and coastal areas generally agree with tidal charts derived from gauge measurements and satellite altimetry data (e.g. Egbert & Erofeeva, 2002). Here, we exemplify simulated M2

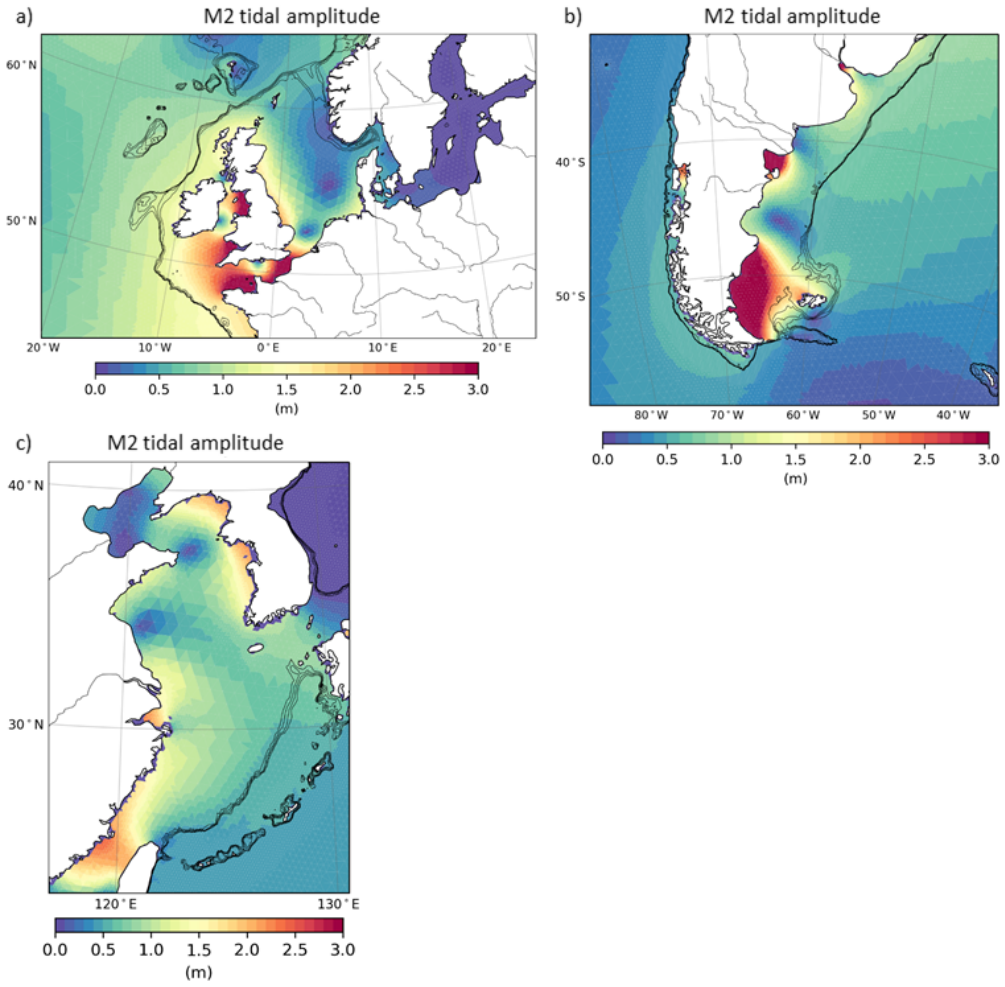

Figure 8: Tidal amplitudes of the semi-diurnal component M2 on the Northwest European Shelf (a), the Patagonian Shelf (b), and East China Shelf (c), simulated with high-res configuration. Isobaths illustrate the shelf break at water depths of 200-500 m.

amplitudes for the three shelf seas under consideration (Fig. 8) and elaborate more on the effects of tide-induced currents related to carbon dynamics in the following sections. A comparison with MPI-ESM cannot be provided here as this model was not run with tides.

ICON-Coast is able to reproduce complex tidal systems in the coastal ocean, as those of the NWES and ECS (Fig. 8). The positions of the amphidromic points of the M2 constituent are well captured. On the NWES, tidal amplitudes reach around 1.5 m in the German Bight area, between 1.5-2 m along the British North Sea coast and maximum heights exceeding 3 m in the English Channel and Celtic Sea (e.g. Reynaud & Dalrymple, 2012). On the ECS, pronounced sea surface elevations of up to 2 m in the Taiwan Strait and along the Korean coast are realistically simulated (e.g. H. Wu et al., 2018), as well as the low amplitudes in the Bohai Sea which do not exceed 0.5 m. The amphidromic pattern of the PS is well captured likewise. Amplitudes, however, are simulated too high by a factor of about 1.5 compared to satellite altimetry data (Birol et al., 2017) and regional tidal modeling (Ke & Yankovsky, 2010; Carless et al., 2016), with simulated maximum values of 6 m in the southern PS.

3.2.3 Seasonal stratification

On temperate shelves, tidal mixing is able to break the summer stratification and in many shallow areas the water column stays vertically mixed throughout the year (van Leeuwen et al., 2015). In deeper areas, the characteristic seasonal stratification prevents respiratory CO_2 below the pycnocline to exchange with the atmosphere (Thomas et al., 2004; Bianchi et al., 2005; Rippeth et al., 2014). Sharp changes in ocean-atmosphere ΔpCO_2 of up to 150 ppm across tidal fronts are often observed (Bianchi et al., 2005). The strength of the stratification as well as its spatial extension and timing in the year thus are key elements of the shelf carbon pump, promoting net horizontal carbon export to the deep open ocean.

Conventional global ocean models are typically run without tides (Taylor et al., 2012; Eyring et al., 2016). Tidal waves mainly transport energy but very little mass (Toffoli & Bitner-Gregersen, 2017), and in the open ocean the local net effects of tides are negligibly small for most applications. Hence, tides are usually omitted in global simulations to save resources. As a consequence, the simulated summer stratification on temperate shelves is too strong and its spatial extension too large, covering also the shallow areas otherwise subject to strong tidal mixing (Fig. 9d-f; Holt et al., 2017; Mathis et al., 2018).

The strength of the seasonal stratification as simulated by ICON-Coast (Fig. 9a-c) is in good agreement with regional high-resolution model studies (Graham et al., 2018b; Guihou et al., 2018) as well as observation-based estimates of the position of the tidal front (Bianchi et al., 2005; Yao et al., 2012; Kahl et al., 2017). For the North Sea, Pätsch et al. (2017) provide a comparison of the potential energy anomaly (PEA) between observations and state-of-the-art regional model systems for August of the period 1998-2009. The PEA quantifies the amount of energy required to vertically mix the entire water column, and hence is often used to evaluate vertical density distributions. The PEA of August calculated for ICON-Coast well reflects the main characteristics given in Pätsch et al. (2017), with values of 100-200 $J\,m^{-3}$ in the stratified areas of the central and northern North Sea, maxima exceeding 500 $J\,m^{-3}$ in the Norwegian Trench, 10-50 $J\,m^{-3}$ in most parts of the weakly stratified southern North Sea, and minima below 1 $J\,m^{-3}$ in the Southern Bight. On the PS, the stratification seems too weak on the southern shelf compared to Kahl et al. (2017) but fits better with the pattern derived by Bianchi et al. (2005). Both studies analyze observational data of 5-7 year periods prior to our analysis period 2006-2010. Nevertheless, the transition from stratified to vertically mixed conditions is mainly determined by the local tidal current speed, the water depth, and the thermal forcing depending on the time of the year. The positions of tidal fronts are therefore rather stable with low interannual variability (E. A. Acha et al., 2004; Holt & Proctor, 2008). The rather weak stratification on the southern PS thus can be attributed to the overestimated tidal currents (section 3.2.2). In the ECS, the summer stratification is exceptionally strong due to cold water transported by the Yellow Sea Warm Current to the central ECS in winter (Z. Liu, Gan, et al., 2021).

Nevertheless, local features like intermittent stratification in shallow coastal areas (van Leeuwen et al., 2015) or a distinct haline stratification in river plumes might not be captured adequately due to the relatively coarse vertical resolution with layer thicknesses of 10 m in the upper 100 m and 16 m in the surface layer (section 2.4). Simulated maximum vertical salinity gradients in the vicinity of large rivers, such as the Yangtze on the ECS and the La Plata north of the PS, reach about 0.25 m^{-1}, in contrast to observations and high-resolution regional modeling studies, reporting values of 0.25-1.0 m^{-1} in the first 10 m of the water column (e.g. M. Acha et al., 2008; Z. X. Zhou et al., 2019; Z. Liu, Zhang, et al., 2021). In more open shelf areas with a pronounced summer thermocline, the vertical resolution used here has been shown to be sufficient to capture the vertical structure of the water column relevant for coastal biogeochemistry modeling (Pätsch et al., 2017). In the northern North Sea, for instance, maximum vertical temperature gradients are simulated 0.4 $°C\,m^{-1}$ by ICON-Coast, which is well comparable to the state-of-the-art regional models evaluated in Pätsch et al. (2017) with layer thicknesses ranging between 0.4-5.0 m.

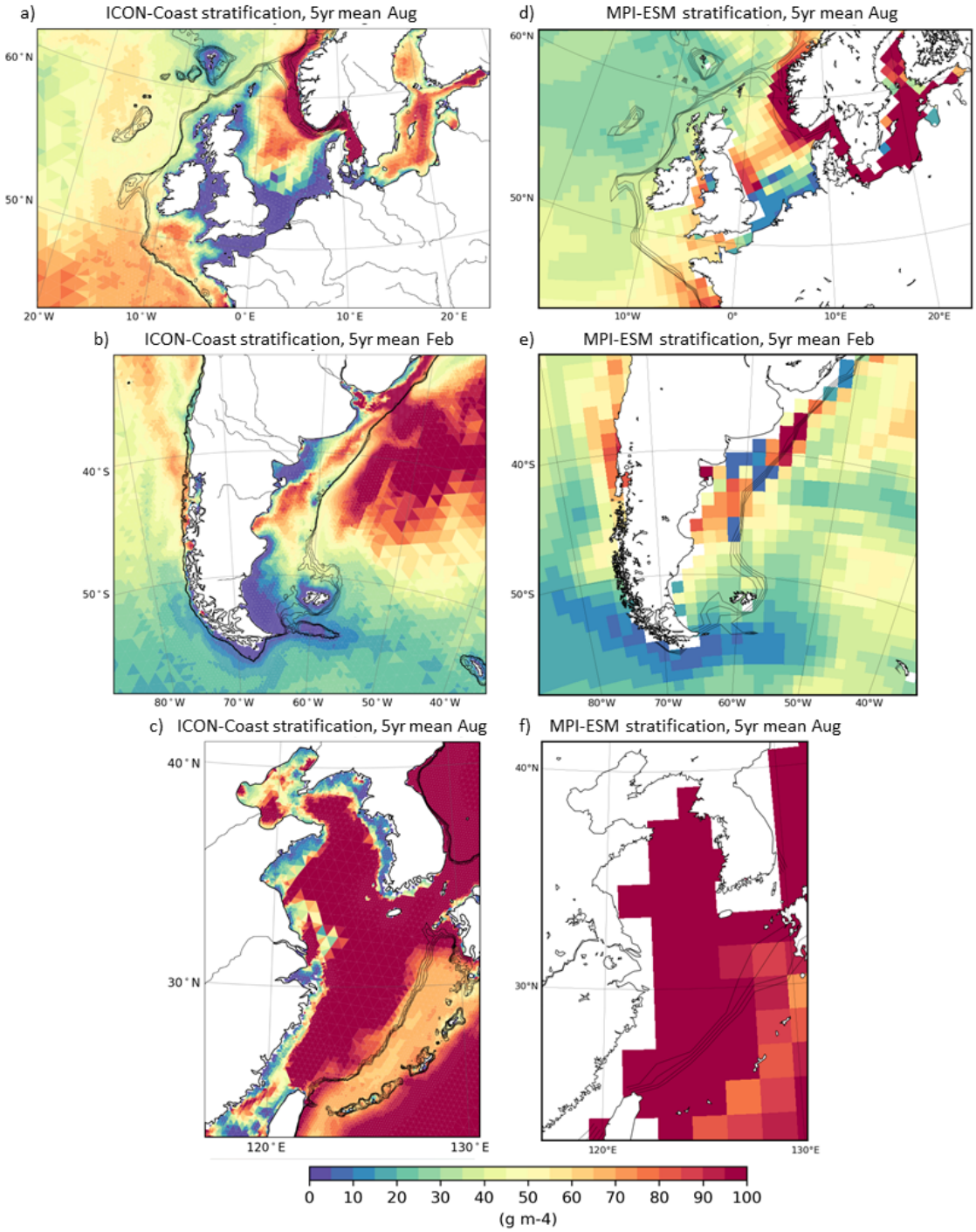

Figure 9: Strength of summer stratification (maximum vertical density gradient) on the Northwest European Shelf (a,d), Patagonian Shelf (b,e) and East China Shelf (c,f), simulated with ICON-Coast high-res configuration (a-c) and MPI-ESM (d-f). Isobaths illustrate the shelf break at water depths of 200-500 m.

3.2.4 Sediment resuspension

Another important effect of tidal currents is their contribution to the strong benthic-pelagic coupling of temperate shelves (Fig. 1 index 3). Elevated flow speeds near the bottom are known to induce critical bed shear stresses that lead to resuspension of deposited particulate matter (Wilson & Heath, 2019). Areas with strong tidal currents thus typically have very low carbon stocks in the sediment ($< 1\%$ TOC dry weight in the upper 10 cm) and essentially net zero accumulation rates (Legge et al., 2020; Diesing et al., 2021). As a consequence, such areas do not function as significant long-term carbon storage. The resuspension of settled organic material and nutrient-rich pore water from sediments back to the water column, though, delivers nutrients for pelagic organisms (F. Liu et al., 2014). This mechanism contributes to the high biological productivity and CO_2 uptake in tidally mixed areas of temperate shelves in summer. The enhanced turbidity due to resuspended particulate matter, however, also reduces irradiance and thus can negatively affect phytoplankton growth (Loebl et al., 2009; Su et al., 2015; Zhao et al., 2019).

In ICON-Coast, we have implemented a sediment resuspension scheme following Mathis et al. (2019). Critical bed shear stresses and the fraction of deposited material that is eroded are inferred from the near-bottom flow speed and the mean density and grainsize of the sediment composition. This dynamical approach enables the simulation of the seasonal cycle of sediment stability and wind-induced resuspension. For our developments, we have initialized the sediment from one of the historical simulations by MPI-ESM used here for direct comparison. This model, however, did not account for resuspension processes and therefore maintained a largely uniform distribution of highly overloaded carbon contents in coastal sediments, exceeding 20% TOC dry weight (Fig. 10d-f).

During the first decades simulated by ICON-Coast, much of the deposited carbon gets eroded from the sediment and remineralized in the water column (Fig. 10a-c). As we started the model development by implementing the resuspension scheme, the sediment distribution shown from ICON-Coast results from an integration time of about 40 years in total (see section 2.4). The patterns of low carbon content ($< 1\%$ TOC dry weight) on the NWES are generally in line with measured distributions shown in Legge et al. (2020) and tide-induced high bed shear stresses reported by Wilson & Heath (2019). On the PS, the simulated carbon content reflects the observed sediment composition given in Violante et al. (2014). Over large PS areas, the sediment is dominated by sands and gravels, associated with low carbon concentrations (Diesing et al., 2017). Muddy sediments with high carbon concentrations are found along the shelf break and in the coastal bays between 39-48°S. Similarly in ICON-Coast, the shelf break as well as the coastal bays on the PS are less affected by resuspension and hence keep elevated carbon fractions in the sediment. Maximum simulated concentrations in these accumulation areas reach up to $220\,\mathrm{kg\,C\,m^{-3}}$ in the uppermost sediment layers. L. M. Hu et al. (2011) and Yang et al. (2014) provide identifications of mud deposition centers on the ECS based on sediment core sampling. As indicated in Fig. 10c, ICON-Coast is able to capture the large deposition area in the center of the Yellow Sea as well as the higher carbon contents in the Bohai Sea.

In deeper shelf areas, bed shear stresses are generally weaker and critical values are rather caused by wind events (e.g. Wilson & Heath, 2019). Accordingly, net erosion rates are lower and the adjustment of the simulated sediment state takes more time. This is reflected by a longer drift in the carbon content for instance in the north-eastern part of the North Sea (Fig. 10a) and the outer shelf areas of the ECS (Fig. 10c). In these regions, relative organic carbon concentrations are still higher than in observations by a factor of about 5. Similarly, POC burial rates in the southern and western North Sea are less than $2\,\mathrm{g\,C\,m^{-2}\,yr^{-1}}$, and vary around 40-70 $\mathrm{g\,C\,m^{-2}\,yr^{-1}}$ in the Norwegian Trench, which is comparable to the rates derived from sediment cores, ranging from 0.02 to 66.18 $\mathrm{g\,C\,m^{-2}\,yr^{-1}}$ (Diesing et al., 2021). In the central and northeastern parts of the North Sea, where the sediment is still overloaded in our experiments, burial rates are simulated about 10-30 $\mathrm{g\,C\,m^{-2}\,yr^{-1}}$, in contrast to less than $5\,\mathrm{g\,C\,m^{-2}\,yr^{-1}}$ found by Diesing et al. (2021). The model drift in global carbon burial

rates are shown in Fig. 11. At the end of the presented low-res simulation, burial rates of particulate organic and inorganic carbon on the shelves (0-500 m depth) amount to 0.62 and 0.15 $\mathrm{Gt\,C\,yr^{-1}}$, respectively. The POC burial rate, however, seems overestimated compared to observation-based upscalings, which are not well constrained, though, ranging between 0.04 and 0.3 $\mathrm{Gt\,C\,yr^{-1}}$ (Duarte et al., 2005; Burdige, 2007). The relative contribution of 75% simulated global POC burial occurring on the shelves is similar to about 80% estimated by Burdige (2007) and Bauer et al. (2013).

3.2.5 Sinking of marine aggregates

As another process extension of ICON-Coast, we have included an aggregate sinking scheme for particulate matter in the water column, following Maerz et al. (2020). Sinking organic and inorganic particles in the ocean tend to stick together by physical aggregation and form particulate assemblages known as marine aggregates. The variable buoyancy of marine aggregates, determined by their size and density, is associated with variable settling velocities that affect the vertical export of sequestered carbon out of the biologically productive euphotic zone (Fig. 1 index 4; Francois et al., 2002). This mechanism crucially contributes to the drawdown of atmospheric CO_2, as any resulting imbalance in sea water pCO_2 near the ocean surface induces CO_2 gas exchange with the atmosphere (Volk & Hoffert, 1985; Kwon et al., 2009).

Global models usually parameterize the attenuation of vertical POC fluxes through an empirical fit to observations (Gloege et al., 2017). Power law parameterizations or exponential decay rates are most widely used. Such approaches, however, lack a mechanistic understanding and are aligned to present-day relations between primary production and remineralization processes. The sinking scheme of ICON-Coast explicitly represents the main structural and compositional characteristics of marine aggregates, and ties ballasting mineral and POC fluxes together. In this way, the model is able to capture main seasonal characteristics of marine aggregates in middle and high latitudes (Fig. 12; Fettweis et al., 2014; Maerz et al., 2016; Schartau et al., 2019). In winter, marine primary production is weak and thus little organic carbon is available to assemble large aggregates. The composition, therefore, is dominated by high-density mineral components, leading to comparatively small aggregate sizes and high sinking speeds (Fig. 12a). During summer, high productivity delivers organic carbon to form biogenic aggregates of larger sizes but lower excess densities, and thus reduced sinking speeds (Fig. 12b). In the open ocean and stratified shelf areas (Fig. 12 north of 54°N), the carbon content gets remineralized while the aggregates sink to deeper levels, and accordingly the aggregates decompose, become more compacted and achieve higher settling velocities. In tidally mixed areas (Fig. 12 south of 54°N), by contrast, sediment resuspension prevents mineral components such as plankton shells and terrestrial dust to become deposited (Babin & Stramski, 2004; Vantrepotte et al., 2012). The aggregates therefore accommodate larger fractions of mineral components, keeping sizes smaller and sinking speeds higher throughout the year. It is worth mentioning that all simulated seasonal aspects of aggregate composition, size and sinking speed emerge from the internal model formulation without prescribing any element of seasonality.

Another factor controlling the turnover rates of organic carbon in the coastal ocean is the age of organic material settled to the sediment. Fresh, dead material in sediments of shallow areas is generally more attractive as source of carbon and energy for benthic organisms than older, more refractory material typically found in deeper areas (Arndt et al., 2013; O'Meara et al., 2018). The heterotrophic recycling of carbon and nutrients is thus accelerated in sediments of shallow areas, potentially stimulating high biological productivity by the resupply of nutrients to otherwise depleted surface waters (Fig. 1 indexes 3 and 5). As our model does not incorporate metabolic reworking of organic matter by benthic communities, we approximate this age effect by a modification of the remineralization rate constant of detritus deposited at water depths of up to 500 m, assigning linearly decreasing values with increasing depth from 0.06 to 0.013 $\mathrm{d^{-1}}$ at a reference temperature of 10 °C.

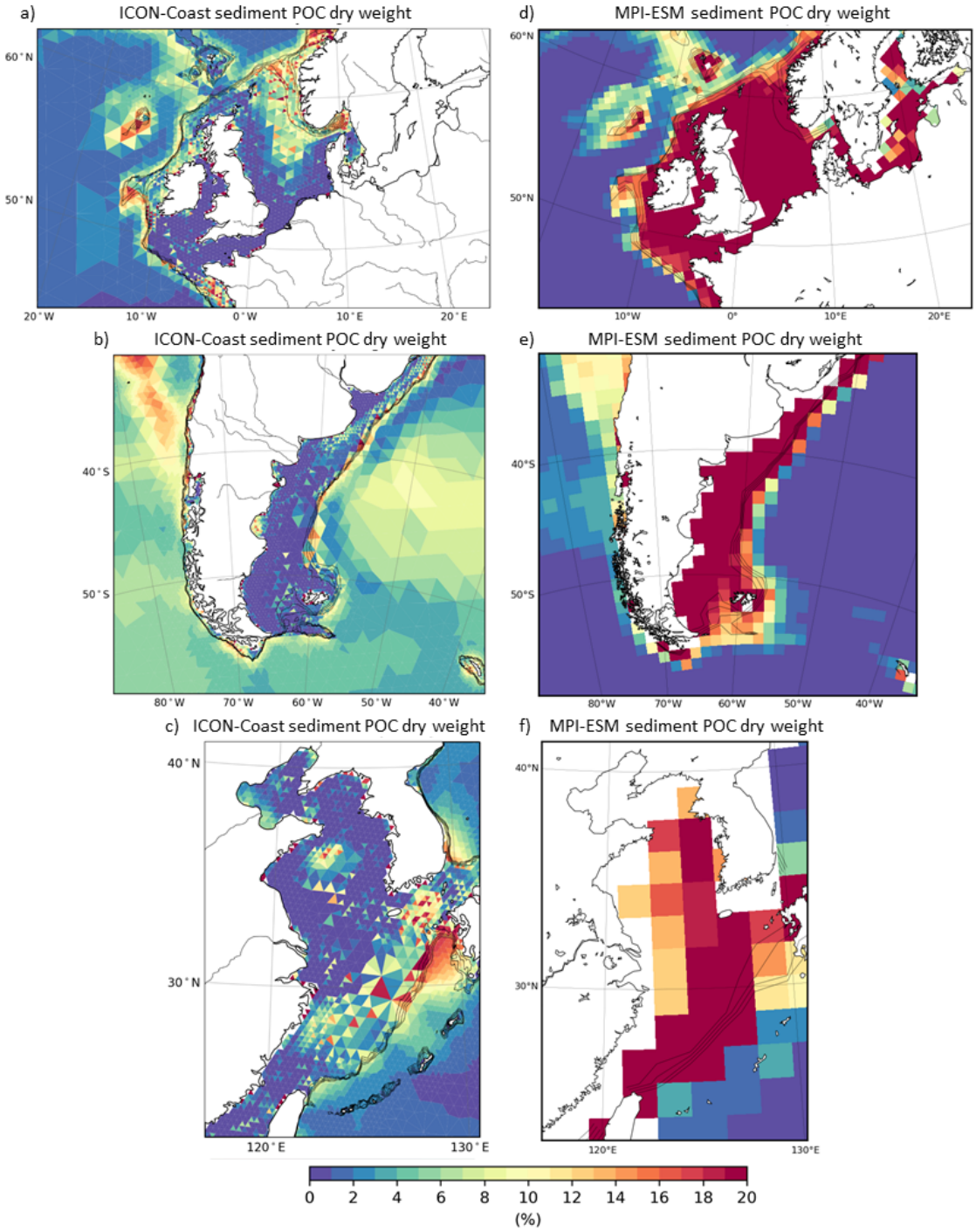

Figure 10: Dry weight of organic carbon in the upper 10 cm of the sediment on the Northwest European Shelf (a,d), Patagonian Shelf (b,e) and East China Shelf (c,f), simulated with ICON-Coast low-res configuration (a-c) and MPI-ESM (d-f). Isobaths illustrate the shelf break at water depths of 200-500 m.

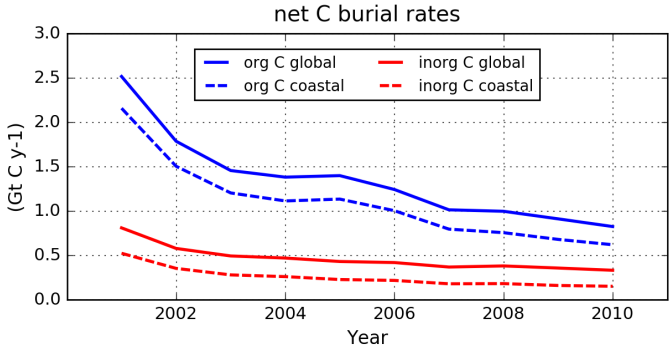

Figure 11: Time series of annual sediment burial rates of particulate organic (blue) and inorganic (red) carbon, simulated by the low-res configuration. Solid lines: global average; dashed lines: coastal ocean (0-500 m depth).

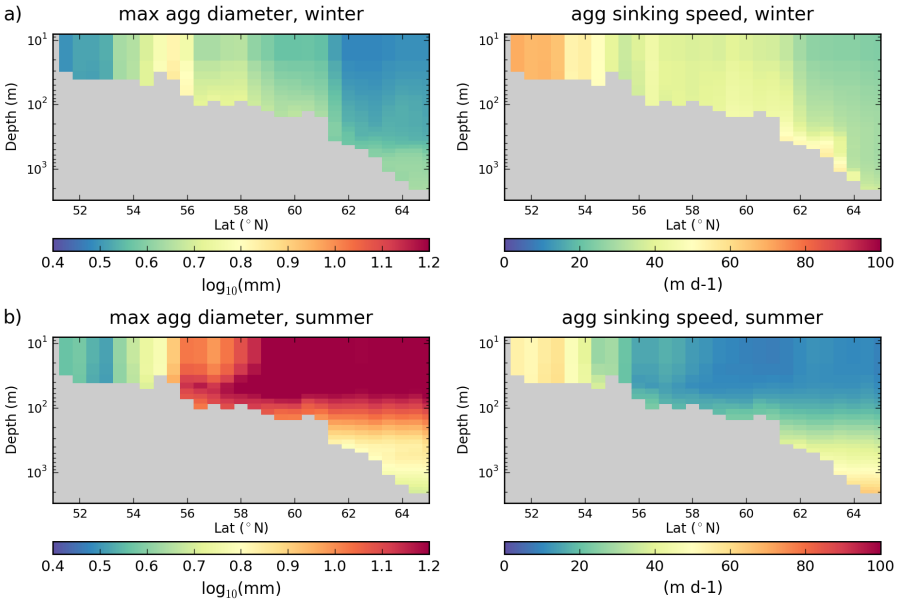

Figure 12: Maximum diameter (left) and mean sinking speed (right) of marine aggregates in winter (a) and summer (b) along a meridional transect through the North Sea at 2.5°E, simulated with low-res configuration.

These values are aligned to the range investigated by Lacroix et al. (2021a), though a more mechanistic parameterization including bioturbation in the upper sediment, as e.g. proposed by Stolpovsky et al. (2015) or Zhang & Wirtz (2017), would be a further improvement.

3.2.6 River inputs

The importance of riverine carbon, alkalinity, and nutrient inputs for addressing regional carbon dynamics at the global scale was recently highlighted by Hauck et al. (2020) and Lacroix et al. (2020, 2021b). In conventional global biogeochemistry models, net particulate export fluxes to the sediment would violate the conservation of global budgets and induce long-term inventory drift as well as artificial gas exchange with the atmosphere. Burial losses are therefore typically balanced by instantaneous remineralization and diffusive resupply to the water column (Najjar et al., 2007) or by prescribed uniform weathering fluxes at the sea surface (Ilyina et al., 2013). In ICON-Coast, weathering fluxes and anthropogenic nutrient loadings are provided by spatially explicit river inputs (Fig. 1 index 6). This approach accounts for the influences of matter fluxes from land on the coastal carbon dynamics and allows to integrate regional, inter-compartmental fluxes as well as imbalances in global inventories under different environmental conditions and human activities (Tamburini & Föllmi, 2009; Wallmann, 2010; Beusen et al., 2016).

Rivers are responsible for the largest export of tDOM to the ocean with an annual flux of about $200\,\mathrm{Tg\,C\,yr^{-1}}$ (Bauer et al., 2013; Kandasamy & Nath, 2016), thus significantly increasing the pCO_2 of the coastal ocean (Lacroix et al., 2020). In our simulations, about 50% of the global terrestrial carbon input is decomposed in the coastal ocean (water depth $< 200\,\mathrm{m}$), lying well within the estimated range of 35-55% given in the literature (Fichot & Benner, 2014; Kaiser et al., 2017; Aarnos et al., 2018). In the broad shelf seas considered here, decomposition proportions are higher due to longer residence times of near-coastal waters (Lacroix et al., 2021a), with simulated values of 58% (of $2.1\,\mathrm{Tg\,C\,yr^{-1}}$) on the NWES, 67% (of $0.8\,\mathrm{Tg\,C\,yr^{-1}}$) on the PS, and 85% (of $6.4\,\mathrm{Tg\,C\,yr^{-1}}$) on the ECS. Other riverine substances directly affecting the surface CO_2 flux are the loadings of alkalinity and dissolved inorganic carbon. As these rarely deviate from each other by more than 10% (Araujo et al., 2014; Middelburg et al., 2020), we use a mole ratio of 1:1 following Lacroix et al. (2020), which leads to a further increase in near-coastal pCO_2.

3.2.7 Primary production

A characteristic feature of many shelf seas is their exceptionally high biological productivity, which is one of the most essential drivers to lower pCO_2 in coastal surface waters of middle latitudes and foster CO_2 ingassing (Muller-Karger et al., 2005; Gattuso et al., 1998). Key processes mediating enhanced phytoplankton growth are: import of nutrient-rich water masses from the adjacent open ocean, additional continuous nutrient supply via river loads, fast internal nutrient recycling, and often strong tidal mixing, which prevents deposition of biologically bound nutrients in the sediment (Dai et al., 2013; Cao et al., 2020). In addition to river loads from land, we prescribe atmospheric dust (Fe) and nitrogen deposition following Mauritsen et al. (2019), which provides another source of inorganic nutrients for marine primary production.

The simulated annual net primary production on the NWES (Fig. 13a) well captures the high phytoplankton growth rates in the near-coastal zones around the British Islands and along the continental coast of the southern North Sea, as well as the strong gradients to the open shelf areas of the central and northern North Sea (Moll, 1998; Provoost et al., 2010; Holt et al., 2012, 2016; Williams et al., 2013). Similarly, the seasonal cycle averaged over the southern and northern North Sea (Fig. 14), separated by the 50 m isobath, well reflects the spring bloom and summer growth seasons (compare to Moll, 1998; Lemmen, 2018). Simulated annual primary production of the entire North Sea is about $160\,\mathrm{g\,C\,m^{-2}\,yr^{-1}}$, falling within the range of 100-230 $\mathrm{g\,C\,m^{-2}\,yr^{-1}}$ given in the cited ob-

servational and regional model studies. Satellite-derived primary production is shown in Fig. A3a,b, with an estimated North Sea productivity of about 150-160 $g\,C\,m^{-2}\,yr^{-1}$. These estimates, however, are sensitively dependent on the utilized satellite data and NPP algorithms (Campbell et al., 2002; Carr et al., 2006), e.g. varying by a factor of 2-4 in coastal primary production among the products provided by the Ocean Productivity service (http://sites.science.oregonstate.edu/ocean.productivity/index.php). Maximum simulated annual productivity in the southern North Sea is about 330 $g\,C\,m^{-2}\,yr^{-1}$, compared to 270-380 $g\,C\,m^{-2}\,yr^{-1}$ measured by Capuzzo et al. (2018), and the simulated spring bloom peaks at 580 $g\,C\,m^{-2}\,yr^{-1}$ in the Southern Bight, which is associated with a considerable observational range of 180-730 $g\,C\,m^{-2}\,yr^{-1}$ reported in Moll (1998). Locally reduced phytoplankton growth measured close to the continental coast (e.g. Capuzzo et al., 2018), however, is not captured by ICON-Coast, as the impact of suspended particulate matter on light conditions is not yet implemented.

The PS is another highly productive shelf sea with an annual net primary production of about 350 $g\,C\,m^{-2}\,yr^{-1}$ according to measurements by Gonçalves-Araujo et al. (2016); Piola et al. (2018), and 180-210 $g\,C\,m^{-2}\,yr^{-1}$ derived by satellite products (Fig. A3c,d). A comparably high phytoplankton growth of 240 $g\,C\,m^{-2}\,yr^{-1}$ is simulated by ICON-Coast (Fig. 13b). In observations, a persistent local maximum of Chl-a concentrations is found along the northern part of the PS shelf break, caused by shelf break upwelling of the northward flowing Malvinas Current (Carreto et al., 2016; Franco et al., 2017). In the low-res simulations, elements of enhanced primary production along the shelf break are also indicated, in spite of slope currents and upwelling transports being underestimated due to unresolved mesoscale processes.

On the ECS, the productivity in the near-coastal zone is strongly influenced by riverine nutrient loads (Fig. 13c), similar to the NWES. In observational products as well as in our simulations, local maxima in net primary production of up to 700 $g\,C\,m^{-2}\,yr^{-1}$ are found in the river plumes of the Yangtze and Yellow Rivers, discharging at the Chinese coasts of the Yellow Sea and Bohai Sea, respectively (Tan & Shi, 2006). Also the seasonal cycle with two pronounced phytoplankton blooms in spring and late summer is captured by ICON-Coast (not shown), with a spring bloom though understimated by about 20% compared to G. Li et al. (2004); Tan & Shi (2012) and Luo (2014). Annual productivity is simulated about 250 $g\,C\,m^{-2}\,yr^{-1}$, compared to 180-360 $g\,C\,m^{-2}\,yr^{-1}$ by the two satellite products shown in Fig. A3e,f.

In conventional global biogeochemistry models, missing factors sustaining enhanced coastal primary production, such as river inputs, sediment resuspension and often the influence of temperature on particulate matter decomposition, lead to substantially underestimated primary production in shelf and marginal seas (Fig. 13d-f). Regions are less biased where import of nutrient-rich water masses from the open ocean are the main source of nutrients, as e.g. on the PS (Fig. 13e).

3.2.8 Surface CO_2 flux

In temperate shelf seas, the high biological productivity and export of dissolved inorganic carbon is typically associated with a net heterotrophic state and CO_2 uptake from the atmosphere (Fig. 1 index 7; Kühn et al., 2010; Becker et al., 2021; Tseng et al., 2011). In the near-coastal zone, river loads play an important role for the air-sea gas exchange at the global scale, as a substantial amount of the CO_2 uptake is caused by biological consumption of riverine inorganic nutrients and the resulting alkalinity production (Hauck et al., 2020; Lacroix et al., 2020). Moreover, the mixing of high-pCO_2 river runoff with low-pCO_2 sea water has been found to induce strong CO_2 uptake in brackish waters of several large river plumes across latitudes, such as the Yangtze and Mississippi plumes (Tseng et al., 2011; Huang et al., 2015; Kealoha et al., 2020). In most high- and low-latitude coastal regions, the temperature effect on the CO_2 solubility of sea water exceeds the biological

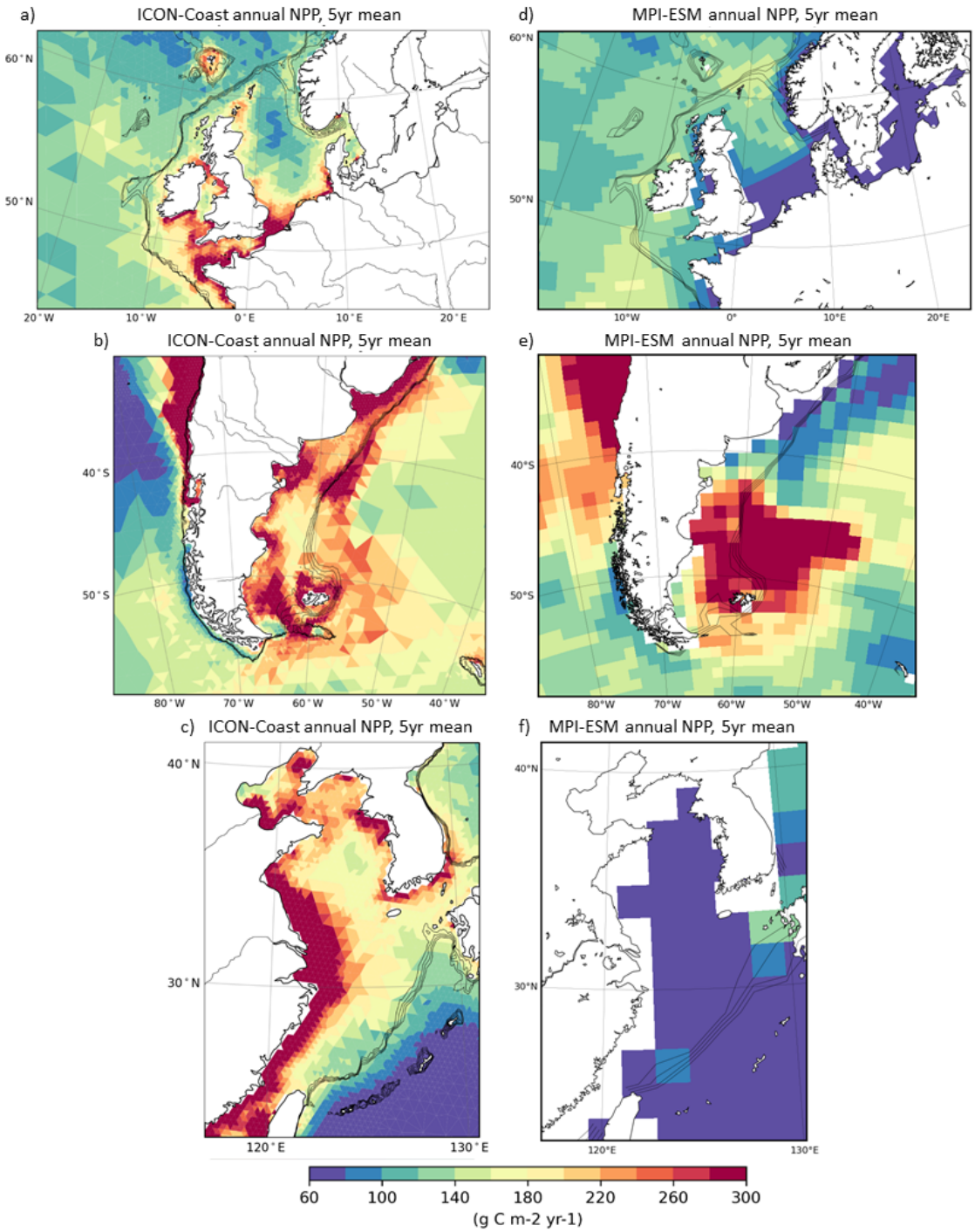

Figure 13: Annual depth-integrated net primary production on the Northwest European Shelf (a,d), Patagonian Shelf (b,e) and East China Shelf (c,f), simulated with ICON-Coast low-res configuration (a-c) and MPI-ESM (d-f). Isobaths illustrate the shelf break at water depths of 200-500 m.

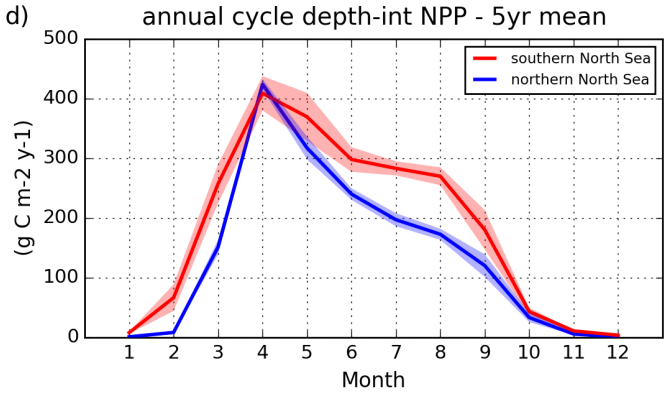

Figure 14: Seasonal cycle in the northern and southern North Sea, simulated with low-res configuration.

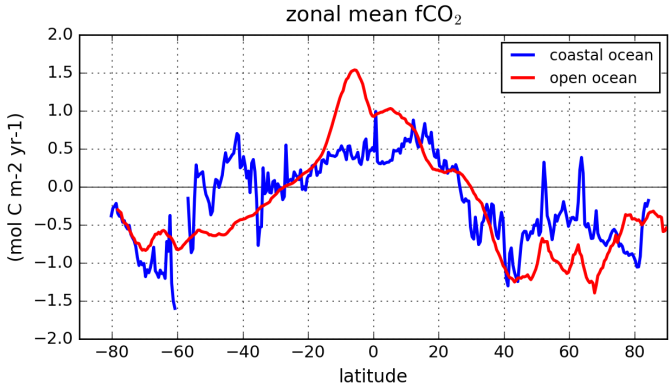

Figure 15: Zonally averaged ocean-atmosphere CO_2 flux for open (red) and coastal (blue; water depth $< 500\,m$) ocean, simulated by the low-res configuration. Positive values refer to oceanic outgassing. The zonal average for the entire ocean is shown in Fig. 4.

CO_2 drawdown, leading to net CO_2 outgassing in low latitudes (G. G. Laruelle et al., 2010; Mayer et al., 2018) and net uptake in high latitudes (K. Arrigo et al., 2008; Yasunaka et al., 2016, 2018). This characteristic is generally captured by ICON-Coast (Fig. 15). The range between CO_2 uptake and outgassing, though, is smaller in the coastal ocean than in the open ocean. Riverine carbon input weakens the uptake in coastal regions of northern high latitudes, whereas continuous productivity in low latitudes has a net weakening effect on the CO_2 flux to the atmosphere. On the southern hemisphere, zonally integrated shelf areas south of about 20°S are comparatively small. Here, the indicated deviations between the coastal and open ocean fCO_2 are thus probably overestimated due to the positive bias on the PS (see below) and the negative bias in the open Southern Ocean (see section 3.1).

For the three focus areas, simulated surface CO_2 fluxes (fCO_2) are shown in Fig. 16. Because of the mixture of driving the model with a modern climate but preindustrial pCO_2 (see section 2.4), the resulting fCO_2 are not fully comparable with present-day observations. In our experiments though, the spatial structures of fCO_2 in the coastal ocean are relatively insensitive to variations in atmospheric pCO_2 ranging from preindustrial to present-day levels. We therefore focus more on the qualitative fCO_2 distributions and gradients here and reflect on the magnitudes of the fluxes in the discussion section 4.

The northern North Sea and outer shelf areas of the NWES are known to be net sinks for atmospheric CO_2 under present-day climatic conditions, while the shallow southern North

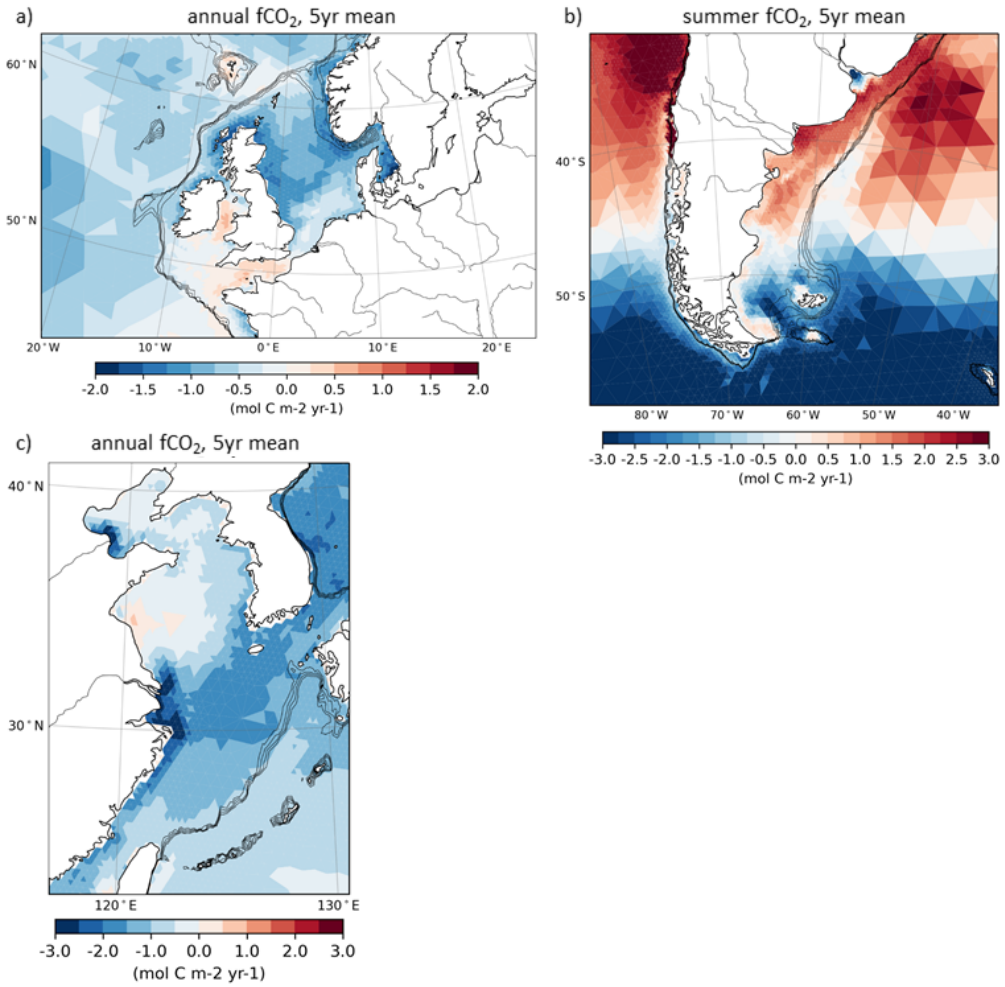

Figure 16: Ocean-atmosphere CO_2 flux for (a) the Northwest European Shelf (annual), (b) Patagonian Shelf (summer), and (c) East China Shelf (annual), simulated by the low-res configuration. Positive values refer to oceanic outgassing. Isobaths illustrate the shelf break at water depths of 200-500 m.

Sea is close to neutral (Thomas et al., 2004; Marrec et al., 2015; Kitidis et al., 2019; Becker et al., 2021). This structure is qualitatively reproduced in our ICON-Coast simulations (Fig. 16a) with an annual mean uptake in the North Sea of about $0.8\,\mathrm{mol\,C\,m^{-2}\,yr^{-1}}$. For the anthropogenic contribution due to rising CO_2, Lacroix et al. (2021b) estimated about $0.5\,\mathrm{mol\,C\,m^{-2}\,yr^{-1}}$. Accounting for this missing component in ICON-coast, we obtain a total uptake consistent with observational estimates of 1.1-1.5 $\mathrm{mol\,C\,m^{-2}\,yr^{-1}}$.

The PS is a significant net carbon sink likewise (Kahl et al., 2017). Tidally mixed coastal areas, however, are dominated by CO_2 outgassing in austral summer (Bianchi et al., 2005). This seasonal feature is also captured by ICON-Coast (Fig. 16b). In the northern part of the PS, though, the outgassing signal is overestimated and extends into the stratified area of the open shelf.

The ECS is simulated as an efficient shelf carbon pump (Fig. 16c). The East China Sea acts as a strong carbon uptake area and the Yellow Sea and Bohai Sea as rather weak ones, which is consistent with observations (Tseng et al., 2011; Jiao et al., 2018; Song et al., 2018). Moreover, the seasonal cycle of fCO_2 in the East China Sea measured by Tseng et al. (2011) is qualitatively well captured by ICON-Coast, with a simulated maximum uptake

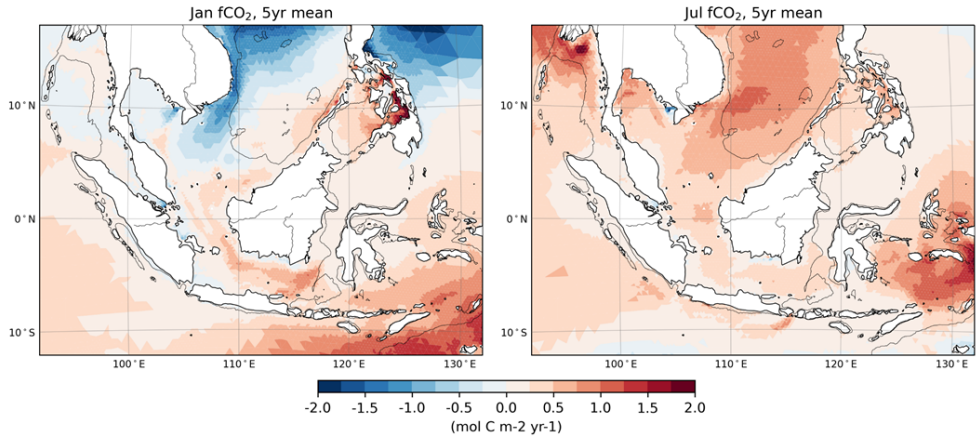

Figure 17: Ocean-atmosphere CO_2 flux on the Sunda Shelf for January (a) and July (b), simulated by the low-res configuration. Positive values refer to oceanic outgassing. The isobath indicates a water depth of 500 m.

of about $3\,\mathrm{mol\,C\,m^{-2}\,yr^{-1}}$ in winter (bias -1.5 $\mathrm{mol\,C\,m^{-2}\,yr^{-1}}$) and a weak outgassing of maximum $0.5\,\mathrm{mol\,C\,m^{-2}\,yr^{-1}}$ (bias -0.1 $\mathrm{mol\,C\,m^{-2}\,yr^{-1}}$) in summer, averaged over the same region investigated in that study. Also here, the underestimated net CO_2 uptake might be attributed to the missing anthropogenic fCO_2 signal which can be estimated to about $0.4\,\mathrm{mol\,C\,m^{-2}\,yr^{-1}}$ according to Lacroix et al. (2021b).

The CO_2 flux at the sea surface is a sensitive metric of the coastal carbon dynamics, as it is affected directly or indirectly by all physical and biogeochemical processes discussed in this section. To provide an outlook of the model skills also in coastal areas other than the temperate shelves, we briefly elaborate on the simulated fCO_2 for the Sunda Shelf (as an example of a large low latitude shelf) and the coastal ocean of the Arctic (as an example of a high latitude region).

In our simulations, the whole Sunda Shelf is releasing CO_2 to the atmosphere on annual means, consistent with observations and regional model studies (Kartadikaria et al., 2015; Mayer et al., 2018; Y. Zhou et al., 2021). The winter and summer monsoon winds drive distinct seasonal circulation regimes on the shelf and lead to a reversed fCO_2 in the northern part in winter (Mayer et al., 2018). ICON-Coast captures this seasonality (Fig. 17) with an uptake of up to $1\,\mathrm{mol\,C\,m^{-2}\,yr^{-1}}$ near the Gulf of Thailand in winter and an outgassing of up to $0.8\,\mathrm{mol\,C\,m^{-2}\,yr^{-1}}$ in summer, while the southern shelf areas show continuous outgassing of 0.3-0.7 $\mathrm{mol\,C\,m^{-2}\,yr^{-1}}$ throughout the year. The annual net outgassing for the entire Sunda Shelf is $0.22\,\mathrm{mol\,C\,m^{-2}\,yr^{-1}}$, compared to $0.65\,\mathrm{mol\,C\,m^{-2}\,yr^{-1}}$ simulated by Mayer et al. (2018), who accounted for anthropogenic pCO_2 rise but not for carbon fixation by phytoplankton. The anthropogenic signal here might further weaken the outgassing by about $0.1\,\mathrm{mol\,C\,m^{-2}\,yr^{-1}}$, estimated from Lacroix et al. (2021b).

The Arctic ocean accomodates the world's largest continental shelves, extending up to 1500 km from the coast of Siberia into the ocean. Most of these areas draw down atmospheric CO_2 via biologically mediated pCO_2 reduction during phytoplankton blooms and cooling of warm water masses intruding from the North Atlantic and Pacific (Bates & Mathis, 2009). Strong net uptake fluxes exceeding $2\,\mathrm{mol\,C\,m^{-2}\,yr^{-1}}$ are simulated by ICON-Coast in the Barents Sea and the deep water formation sites of the Greenland-Iceland-Norwegian Seas (Fig. 18), in agreement with multi-year observations by Yasunaka et al. (2016, 2018). Regionally enhanced uptake of more than $1\,\mathrm{mol\,C\,m^{-2}\,yr^{-1}}$ is also indicated in the Chukchi Sea, both in our simulations and field measurements e.g. by Bates (2006) and Cai et al. (2010). The gradient along the Eurasian Arctic shelves from high uptake in the western part (Barents Sea) to relatively weak fluxes in the eastern part was also observed by Pipko

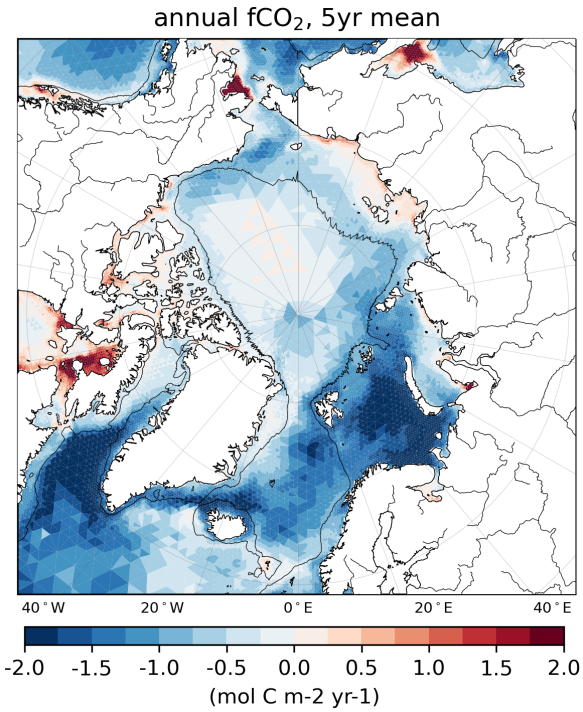

Figure 18: Ocean-atmosphere CO_2 flux for the greater Arctic, simulated by the low-res configuration. Positive values refer to oceanic outgassing. The isobath indicates a water depth of 500 m.

et al. (2017), who measured a regional difference in outer shelf pCO_2 of about 50-100 ppm during fall, compared to about 50 ppm simulated by ICON-Coast. In the same study, the outgassing along the coasts of the eastern part was attributed to the influences of river runoff and terrestrial carbon loads. While the spatial pattern of Arctic fCO_2 seems qualitatively well represented, the simulated uptake is generally weaker than contemporary observations of comparable periods. In the Arctic area used by Yasunaka et al. (2018), that is north of 65°N, excluding the Greenland and Norwegian seas and Baffin Bay, the ocean takes up 73 $\mathrm{Tg\,C\,yr^{-1}}$ in our simulation, compared to the observational spread of 80-200 $\mathrm{Tg\,C\,yr^{-1}}$ obtained by Bates & Mathis (2009) and Yasunaka et al. (2018). Here, the missing anthropogenic fCO_2 signal is difficult to conclude from Lacroix et al. (2021b) as the related fluxes are spatially rather heterogenous, ranging locally between $\pm 0.7\,\mathrm{mol\,C\,m^{-2}\,yr^{-1}}$.

Overall, the spatial patterns of seasonal and annual fCO_2 simulated by ICON-Coast for various regions are qualitatively consistent with the observational products cited here. In particular the skill in capturing seasonality is a remarkable achievement, contrasting the large model-data mismatch on the seasonal time scale of conventional global biogeochemistry models until now (Hauck et al., 2020). Nevertheless, the net uptake fluxes in middle and high latitudes are systematically underestimated, which can be attributed to the lower atmospheric pCO_2 of preindustrial levels used in our simulations. First-order model estimates of the change in CO_2 flux solely resulting from the pCO_2 rise during the 20th century (Lacroix et al., 2021b) show a weak intensification of the CO_2 flux into the global coastal ocean by $0.16\,\mathrm{mol\,C\,m^{-2}\,yr^{-1}}$ and a clear latitudinal structure, with stronger increases at higher latitudes. We therefore are optimistic that the magnitudes of the net fluxes simulated by ICON-Coast will get closer to observations of the recent past when we increase atmospheric CO_2 concentrations to present-day values. This might also reduce the regional and seasonal fCO_2 biases e.g. on the PS, as these are consistently resulting from too high pCO_2 in the ocean relative to the atmosphere.

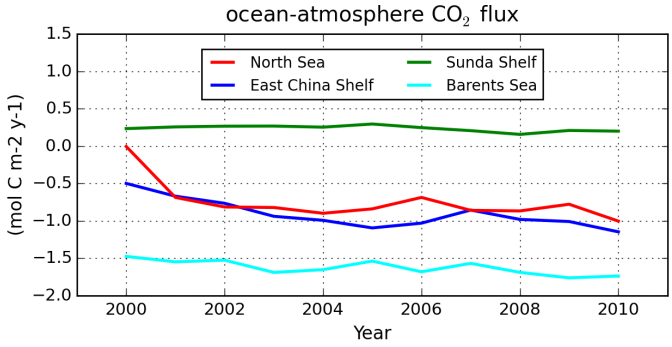

Figure 19: Time series of annual ocean-atmosphere CO2 flux in various shelf seas, simulated by the low-res configuration. Positive values refer to oceanic outgassing.

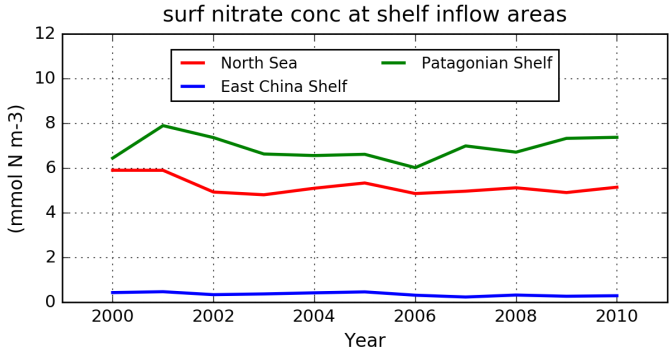

Figure 20: Time series of annual surface nitrate concentrations in main inflow areas of the North Sea (lon 2-4°W, lat 59-61°N), PS (lon 62-64°W, lat 55-57°S) and ECS (lon 123-125°E, lat 25-27°N), simulated by the low-res configuration.

4 Discussion

We have introduced a new global modeling approach aiming to reduce uncertainties in the marine carbon cycle via increased grid resolution in the land-ocean transition zone and enhanced process representation of physical and biogeochemical shelf sea dynamics. Our evaluation therefore focused on the coastal ocean, whereas in the open ocean we expect the global patterns shown in Fig. 3, as well as their spatial integrals, to be still significantly influenced by the initial conditions because of the comparatively short simulation periods of 10-20 years. In particular the state of the deep ocean, including the sediment composition, is subject to long-term model drift (Heinze et al., 1999; Palastanga et al., 2011). In many coastal regions, however, the ocean circulation and tracer distribution are rather dominated by short-term regional-scale and even local-scale processes such as tidal mixing, river loads, and the regional atmospheric forcing. In our test simulations, accordingly, most variables on the shelves show a quick response to the external forcing already in the first few years, without a strong discernable drift but a high sensitivity to changes in model-specific parameters (Fig. 19). In particular the spatial patterns and gradients are rapidly developing. Also the nutrient concentrations of open ocean water masses flushing the shelves are relatively stable over the simulated period (Fig. 20). These characteristics allow us to gain a basic understanding about the performance of the model in various shelf and marginal seas, although the currently available model runs are relatively short.

As known from regional model studies, an increased horizontal resolution in the coastal areas generally improves the spatial manifestation of the implemented physical and bio-

geochemical processes (e.g. Mathis et al., 2015; Graham et al., 2018a, 2018b; Guihou et al., 2018; de Souza et al., 2020). Moreover, the structure and strength of the general circulation, including ocean-shelf exchange, gets more realistic, which affects the distribution of water masses and associated residence times (Pätsch et al., 2017; X. Liu et al., 2019; Lacroix et al., 2021a). The transport rates of boundary and slope currents, for instance, are underestimated in our low-res runs but become more energetic in the high-res simulation, e.g. with increases of the Malvinas Current along the PS by 20% (high-res mean 20.7 Sv at 45°S, literature 20-25 Sv by Frey et al., 2021), the NWES slope current by 35% (high-res mean 2.4 Sv at 58°N, literature 1-4 Sv by Marsh et al., 2017; Clark et al., 2021), and shelf break upwelling velocities by a factor of 4. On the shelves, the general patterns of the circulation and seasonal stratification are comparatively similar in both configurations (Fig. A4), though become more structured and confined in high-res. Resulting residence times of about 1 yr for the North Sea and East China Sea and 1.8 yr for the Patagonian Shelf are comparable to Lacroix et al. (2021a), who used a mesh spacing of 0.4°, and observational estimates given therein. The representations of the bottom topography and the orography of coastlines are further improved in ICON-Coast by the unstructured triangular grid due to the smoother horizontal discretization of topographic features compared to the typical staircase approximation by rectilinear grids. In MPI-ESM (in particular LR), by contrast, the coarser grid resolution in the coastal ocean leads to a systematic underestimation of shelf sea circulations (Fig. 6c, d). While the general flow pattern is partly captured in outer shelf areas, the structure and strength of individual currents, in particular in the inner areas, is not adequately represented. Moreover, in the south-western Atlantic, the position of the Brazil Malvinas Confluence is simulated too far to the south by about 10°(Fig. 6d), disturbing water mass properties in the northern part of the PS with biases of up to +5 ℃ in surface temperature and +0.7 in salinity (+1 ℃ and +0.4 in ICON-Coast). Overall we therefore expect for ICON-Coast in particular the influences of cross-shelf transport, coastal upwelling and baroclinic instabilities on net carbon deposition and export rates in the coastal ocean to improve further when we include the biogeochemistry component also in the high-res setup. In the open ocean, our simulations show that the increase in resolution from a mesh spacing of 160 km (low-res) to 80 km (high-res) leads to a better representation of the large-scale gyre system (Fig. 21), reduced biases in winter mixed layer depths, and more realistic locations of deep and bottom water formation sites (Fig. 22) in particular in the North Atlantic. The strength of the Atlantic meridional overturning circulation at 26°N is simulated 16.0 Sv with high-res, compared to 11.2 Sv with low-res and 16.8 Sv during 2005-2017 measured by the RAPID time series (Moat et al., 2020), which indicates a generally underestimated large-scale circulation in low-res. These differences reflect the typical behavior of global Earth system models to increased resolution (Hewitt et al., 2020). The improved circulation should then also affect the global distribution of biogeochemical tracers such as nutrients (Fig. 3c and Fig. A1), dissolved carbon, and alkalinity. In this original model version and low-res configuration of ICON-Coast, the global biogeochmical patterns and biases are overall similar to MPI-ESM simulations evaluated in Giorgetta et al. (2013), Müller et al. (2018) and Mauritsen et al. (2019). An exception is the transfer efficiency of biogenically bound carbon from the upper to the deep ocean, which shows a more realistic latitudinal distribution in ICON-Coast due to the implemented variable sinking speed and temperature-dependent remineralization of particulate organic matter (as also obtained by Maerz et al., 2020).

The concept of using unstructured variable-resolution meshes to enhance the quality of a simulation in the region of interest was developed about 1-2 decades ago (e.g. C. Chen et al., 2003; Pain et al., 2005; Piggott et al., 2008; Behrens & Bader, 2009) and has seen substantial progress in recent years concerning optimization, stability, and complexity (Weller et al., 2016; Remacle & Lambrechts, 2018). Applications of global grid configurations with regional refinement in the coastal ocean, however, were focused on physical ocean modeling so far (D. V. Sein et al., 2017; Hoch et al., 2020; Logemann et al., 2021). Our simulations thus provide a proof-of-concept for an extension of this strategy to include global biogeochemistry modeling. For the investigation of single target regions of the coastal ocean, an innovative

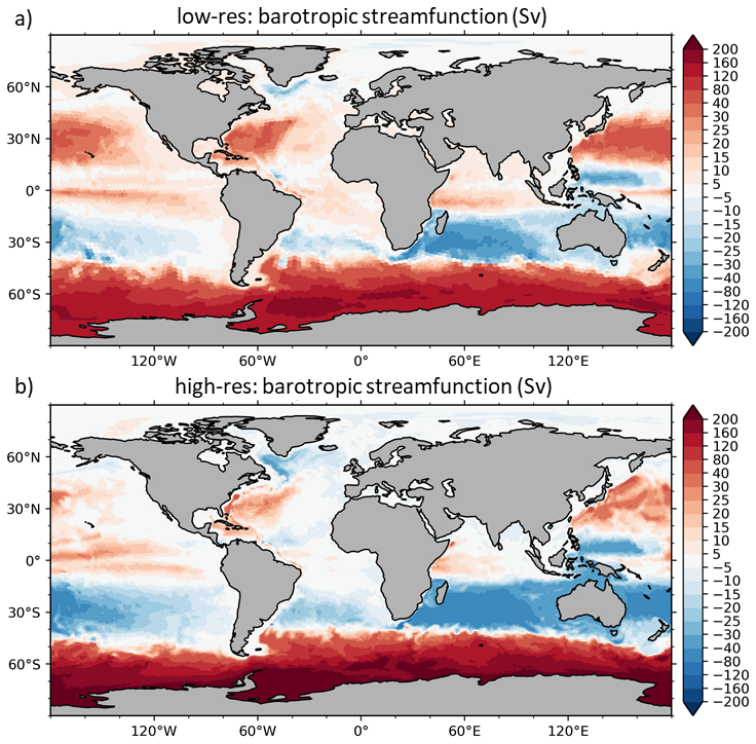

Figure 21: Barotropic streamfunction simulated by the low-res (a) and high-res (b) configurations.

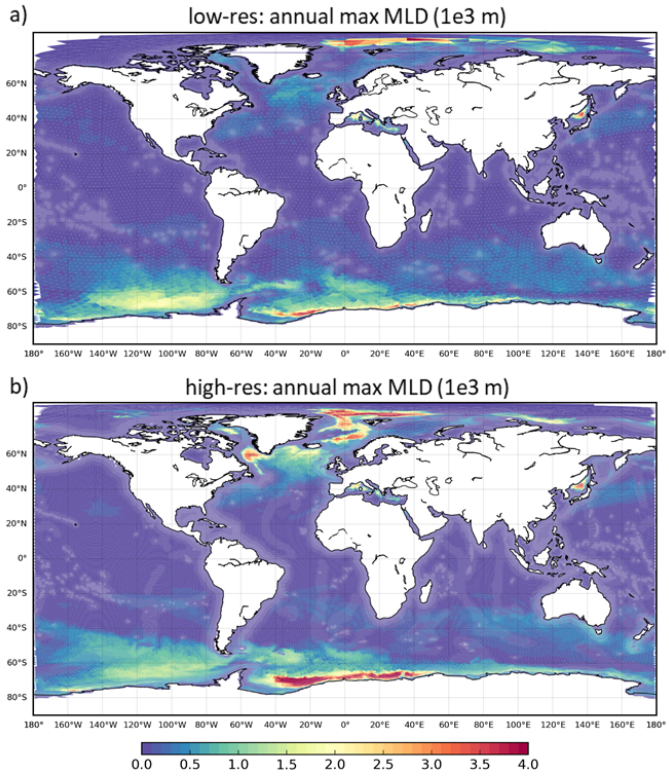

Figure 22: Annual maximum mixed layer depth simulated by the low-res (a) and high-res (b) configurations. Values in the northern and southern hemispheres represent March and September conditions, respectively.

approach including biogeochemistry was achieved by using stretched global rectilinear grids, utilizing the naturally higher resolution in the vicinity of grid poles (Gröger et al., 2013; D. Sein et al., 2015). The sediment resuspension scheme adapted for ICON-Coast, for example, was first developed for such a system (Mathis et al., 2019). The flexibility of the grid generator used here (Logemann et al., 2021) also allows an assignment of increased resolution to spatially confined areas only, without the limitation of too coarse resolution in pole-distant regions that comes with stretched rectilinear grids. In the vertical, however, we are obliged to use a comparatively thick surface layer (16 m) in our global setup to accomodate exceptional negative sea level anomalies in coastal grid cells, resulting from the total of high tidal amplitudes, wind-induced off-shore transport and local sea ice thickness. As a further development, though, we are considering z* coordinates as an alternative vertical grid structure of the model, following work in progress at the Max-Planck-Institute for Meteorology. In a z* system, the free surface elevation is distributed among all grid layers, thus avoiding critical surface layer thicknesses and enabling higher vertical resolution also in shallow, tidally active regions. We expect this to facilitate improvements of simulated stratification dynamics in the near-coastal zone, such as intermittent stratification (van Leeuwen et al., 2015), and related vertical and frontal fluxes of carbon, oxygen and nutrients, which were shown to impact e.g. phytoplankton dilution and phenology (Zhao et al., 2019). Furthermore, in combination with a high horizontal resolution, the model might better represent estuarine-like circulations and associated nutrient trapping in coastal regions of fresh water influence (Algeo & Herrmann, 2018). Air-sea gas exchange could also be affected, as surface fluxes are governed by saturation pressures in the surface layer. In the presented setup, the limited vertical resolution may particularly affect the shallowest areas with a bathymetry < 26 m, which are currently represented by only 2 grid layers. The total fraction of such areas corresponds to about 6% of the global coastal ocean (water depth < 500 m) in both configurations, low-res and high-res.

The additional processes generalized in ICON-Coast, compared to ICON-O and its standard version of HAMOCC, are all crucially linked to the cycling of carbon and nutrients in the coastal ocean (Fig. 1). Tidal waves induce mixing and sediment resuspension, the aggregation of particulate matter affects vertical export fluxes, the temperature dependencies of remineralization and dissolution rates modify the internal recycling, and river inputs act as relevant sources of allochthonous organic and inorganic material. We evaluated these add-ons with respect to the ability of the model to simulate key physical and biogeochemical parameters influencing the surface CO_2 flux in the coastal ocean as well as the resulting CO_2 flux itself (yet under idealized conditions). The necessity to accurately reproduce tidal circulation, stratification, exchange flows, and sediment diagenesis for embedding coastal interface biogeochemistry in global ESMs was pointed out recently by Ward et al. (2020). Irrespective of remaining model biases and a yet unmature spinup history, the added value of ICON-Coast stands out in the shown comparison of simulated coastal carbon dynamics with the Earth system model MPI-ESM. Owing to its coarser resolution and the lack of the additional processes integrated here, MPI-ESM is treating coastal areas essentially like a shallow version of an open ocean basin, leading to an inherent misrepresentation of the land-ocean transition zone in the marine carbon cycle. Note that for these structural differences, the ocean-atmosphere coupling included in MPI-ESM is of minor relevance. In fact, surface fluxes are often better balanced in coupled simulations, inducing more realistic gradients and lower biases (e.g. Small et al., 2011; Wang et al., 2015; Xue et al., 2020). Nevertheless, as mentioned above, MPI-ESM has also been run at a higher nominal resolution with a mesh size of 0.4°. The globally higher resolution of the uniform grid, though, is associated with a substantial increase in computational cost (by a factor of about 10 according to Mauritsen et al., 2019), making applications to investigate the coastal ocean at climatic time scales inefficient. In our variable-resolution approach, the number of surface grid cells is reduced by 77% compared to a uniform grid with the same resolution in the coastal ocean, and even the low-res configuration used here has a mesh spacing in many coastal areas that is higher than MPI-ESM-HR by a factor of 2. Moreover, while the circulation improves in MPI-ESM-HR compared to LR (Fig. A5a), the deficiencies in

simulating coastal carbon dynamics essentially remain the same due to the oversimplified process representation (Fig. A5b). The conceptual extension by ICON-Coast thus links to the prospected reduction of uncertainties associated with global modeling exercises. The increased degree of freedom that results from both the higher resolution and extended process representation allows the coastal system to respond to external perturbations, while at the same time feeding back to the adjacent open ocean. Continuous global warming, for instance, would affect local stratification, carbon and nutrient recycling rates as well as the composition and sinking speed of particulate matter. Changes in sea level or wind surge would affect tidal currents and thus net carbon deposition in the coastal sediments. In conventional global models, by contrast, projections for the carbon budget of the coastal ocean are essentially determined by changes in the stratification and large-scale circulation of the open ocean, as without the process extensions made here, import of open ocean water masses represents defacto the only variable nutrient supply mechanism for coastal primary production.

One of the main challenges in the model development of ICON-Coast is to bridge the dynamic scales from the deep and open ocean to the shallow shelves and marginal seas by applying globally implemented parameterizations to both eddying and non-eddying regions. ICON-Coast uses a biharmonic horizontal dissipation scheme that is dependent on the mesh spacing and thus, in combination with the regional refinement, accounts for the transition of pertinent scales. The implemented TKE vertical mixing scheme is also scale-dependent but could be further improved to better represent mixing at the bottom boundary layer as suggested e.g. by Holt et al. (2017). In our simulations, we have intentionally deactivated the eddy parameterization (Korn, 2018) because first, the combination of eddy closure with the coastal grid refinement considered here is an unsolved problem in computational fluid dynamics, and second, it allows us to better assess the impact of the grid refinement. Yet, we are optimistic that a suitably chosen eddy parameterization will lead to additional improvements of our results, in particular for the general circulation and tracer distribution in the open ocean. The incorporation of subgridscale eddy activity was shown to impact temperature, salinity and sea ice formation in high latitudes (e.g. Knutti et al., 1999; Pradal & Gnanadesikan, 2014) as well as nutrient replenishment in the upper thermocline of oligotrophic subtropical waters (Oschlies, 2008; Doddridge & Marshall, 2018) and seasonal carbon drawdown in the eddy-rich Southern Ocean (Jersild et al., 2021). The sediment resuspension scheme of ICON-Coast accounts for the bottom layer thickness in the calculation of the sediment drag coefficient, thus accounting for the vertical grid resolution (Mathis et al., 2019). Also here, an improvement would be to include dependence on the horizontal grid scale as well.

Apart from a better representation of coastal carbon dynamics, higher resource demands of ICON-Coast compared to conventional global models with coarser resolution are justified by the benefit of having included all coastal areas of the world within a single consistent simulation, thus naturally accounting for two-way coupling of ocean-shelf feedback mechanisms at the global scale. Computational costs as well as data storage requirements of high-resolution simulations, though, can be substantially reduced by limiting the grid refinement to dedicated areas only. In Table 3, we contrast resource demands for simulations with ICON-O and ICON-Coast, run on the high-res grid presented here (80-10 km) as well as on a globally uniform 10 km grid. Because of the regionally applied grid refinement, the variable-resolution grid of ICON-Coast has less surface grid cells than the uniform-resolution grid by a factor of about 4.3. We conducted reference experiments at the current HPC system Mistral of the DKRZ, using 200 parallelized cpu nodes (see caption of Table 3 for specifications). The lower number of grid cells of the variable-resolution grid leads to a significant saving in computational cost, reducing the required real time for a simulation of 100 years with ICON-O from about 3 months to less than 1 month. The computational demands of ICON-Coast, however, increase by 25% due to the additionally implemented processes (section 2.2). About 30% of cost and time are associated with output writing, resulting in a total demand of 50 days for a 100-year simulation with ICON-Coast, including monthly

Table 3: Resource demands for simulations with ICON-O and ICON-Coast, when run on the high-res grid with variable mesh sizes of 80-10 km as well as on a globally uniform 10 km grid. The ICON-O run on the high-res grid differs from the ICON-Coast run only with respect to the additional processes implemented to ICON-Coast (see section 2.2). All simulations are performed using 200 nodes of the HPC system 'Mistral'. Each node of the used partition consists of 2x 18-core Intel Xeon E5-2695 v4 (Broadwell) processors with a speed of 2.1 GHz. To quantify the net computing load, we give turnover rates and computational costs also for simulations excluding model output. For runs on the variable-resolution grid, this setup corresponds to an efficiency of about 0.75 and 0.85 with and without output writing, respectively, compared to linear scaling.

Metric	ICON-O uni. 10 km	ICON-O var. 80-10 km	ICON-Coast var. 80-10 km
Wet surface cells	3,730,000	860,000	860,000
Turnover (no outp.)	1.16 yr d^{-1}	3.70 yr d^{-1}	2.78 yr d^{-1}
Turnover (w. outp.)	0.97 yr d^{-1}	2.50 yr d^{-1}	2.00 yr d^{-1}
Cost (no outp.)	413 knh $100yr^{-1}$	128 knh $100yr^{-1}$	172 knh $100yr^{-1}$
Cost (w. outp.)	492 knh $100yr^{-1}$	192 knh $100yr^{-1}$	240 knh $100yr^{-1}$
Storage	45.9 TB $100yr^{-1}$	9.0 TB $100yr^{-1}$	11.1 TB $100yr^{-1}$

2d and 3d gridded physical and biogeochemical standard output. Similarly, the regional grid refinement reduces the storage space required for the output by a factor of about 4. These specifications of ICON-Coast allow for reasonable experimental setups e.g. to study the anthropogenic perturbation of the marine carbon cycle, comprising a 50-yr spinup run and two 100-yr production runs. Longer spinup simulations spanning a few hundred years could be performed with the low-res grid configuration at comparable total cost.

5 Conclusions

In this paper, we have introduced ICON-Coast, the first global ocean-biogeochemistry model that uses a telescoping high resolution for an improved representation of coastal carbon dynamics. This approach enables for the first time a seamless incorporation of the global coastal ocean in model-based Earth system research. The broad agreement of simulated shelf-specific physical and biogeochemical processes with both observational products and high-resolution regional modeling studies demonstrates the large potential of ICON-Coast to be used for cross-cutting scientific applications. Linkages between carbon and nutrient transformation pathways in the open ocean, the transition zone to the continental shelves, and the near-coastal areas can be investigated that cannot be derived from isolated regional modeling studies. Examples are the importance of carbon sequestration, storage, and transport processes on the shallow shelves relative to the open ocean under different climatic conditions (G. G. Laruelle et al., 2018), or the fate of river inputs and their connection to interhemispheric carbon transport (Aumont et al., 2001; Resplandy et al., 2018). Sensitivity experiments can be used to explore the susceptibility of the coastal ocean environment to external perturbations across a range of spatiotemporal scales and interfaces (Ward et al., 2020).

The high quality of the model results shown here as well as the efficiency in computational cost and storage requirements verifies the strategy of a seamless connection of the open and coastal ocean via regional grid refinement and enhanced process representation as a pioneering approach for high-resolution modeling at the global scale. In view of the difficulties in reconciling prognostically shelf-specific processes in the sediment, water column, and at the air-sea interface, the model ICON-Coast, built on extended basic parameterizations of a global ocean-biogeochemistry model, is encouraging.

Already with the low-res version, spanning a horizontal mesh spacing of 160-20 km, we achieve unprecedented accuracy and level of detail in simulating governing processes of the

coastal carbon dynamics in low, middle and high latitudes, even on the seasonal time scale. Some features, such as the general circulation or net primary production, are comparable to results from state-of-the-art high-resolution regional model systems, and the incorporation of marine aggregates even exceeds the process representation of many established regional ecosystem models. We thus conclude that ICON-Coast represents a new tool to deepen our mechanistic understanding about the role of the land-ocean transition zone in the global carbon cycle, and to narrow related uncertainties in global future projections.

The development of this first version of ICON-Coast was guided by the consideration of coastal carbon dynamics. It is clear, however, that the scientific applications of such a model system are not restricted to topics related to the carbon cycle. The concept of ICON-Coast generally enables high-resolution modeling in the global coastal ocean, including the continental margin as the transition to the open ocean. Potential applications thus range from investigations of marine extreme events in coastal areas (e.g. storm surges, heat waves, hypoxia), and ocean-shelf exchange processes including feedback mechanisms, to scenario-based future projections of the coastal ocean physical and biogeochemical state, and sensitivity studies regarding the efficiency of various coastal management and eutrophication policies.

Data availability statement

The model code of ICON-Coast is available to individuals under licenses (https://mpimet.mpg.de/en/science/modeling-with-icon/code-availability). By downloading the ICON-Coast source code, the user accepts the license agreement. The source code of ICON-Coast used in this study as well as primary data used for producing the figures can be obtained from the Zenodo archive https://doi.org/10.5281/zenodo.6630352.

Acknowledgments

This work contributed to the subproject *A5 - The Land-Ocean Transition Zone* of Germany's Excellence Strategy EXC 2037 *CLICCS - Climate, Climatic Change, and Society* with project No 390683824, funded by the Deutsche Forschungsgemeinschaft (DFG, German Research Foundation). Computational resources were made available by the German Climate Computing Center (DKRZ) through support from the German Federal Ministry of Education and Research (BMBF). TI was supported by the European Union's *Horizon 2020* research and innovation program under grant agreement No 101003536 (*ESM2025 - Earth System Models for the Future*). We thank the associate editor Andreas Oschlies and two anonymous reviewers, whose comments helped improve and clarify this article.

Appendix A Supplementary figures

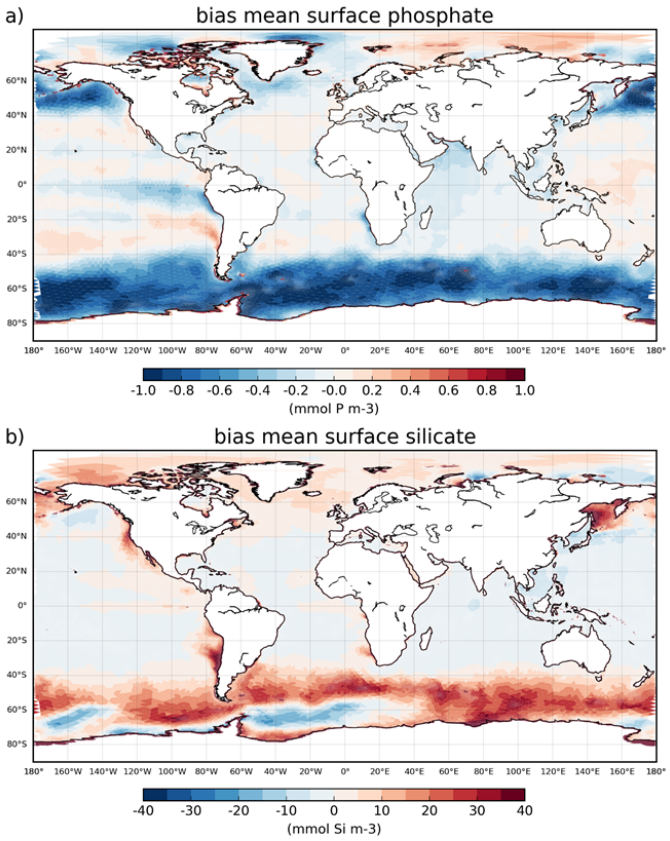

Figure A1: Global distribution of biases in annual surface phosphate (a) and silicate (b) concentrations, simulated with ICON-Coast low-res configuration. Biases are relative to World Ocean Atlas 2018 Boyer et al. (2018).

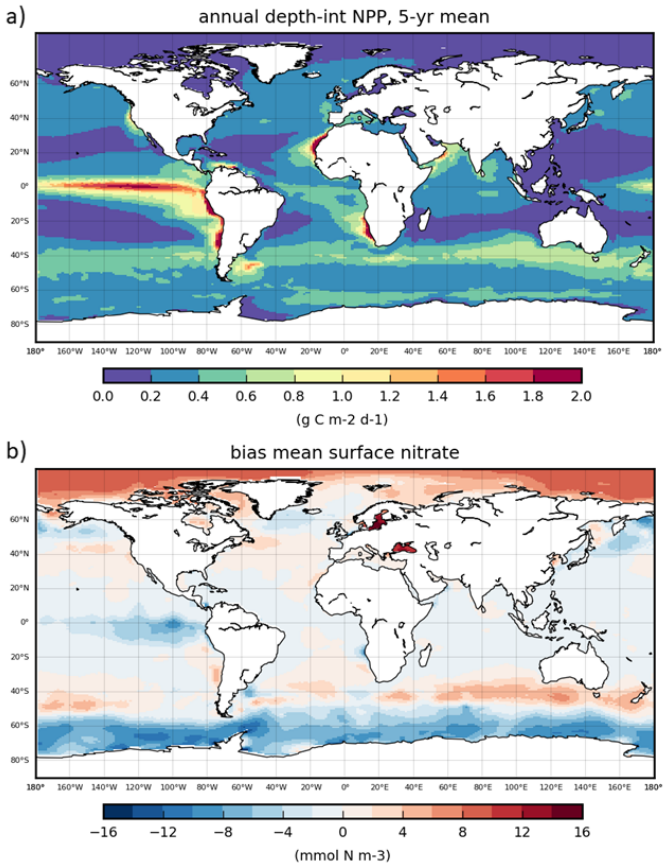

Figure A2: Global distribution of annual depth-integrated net primary production (a) and biases in annual surface nitrate concentration (b), simulated with MPI-ESM-LR. Biases are relative to World Ocean Atlas 2018 Boyer et al. (2018).

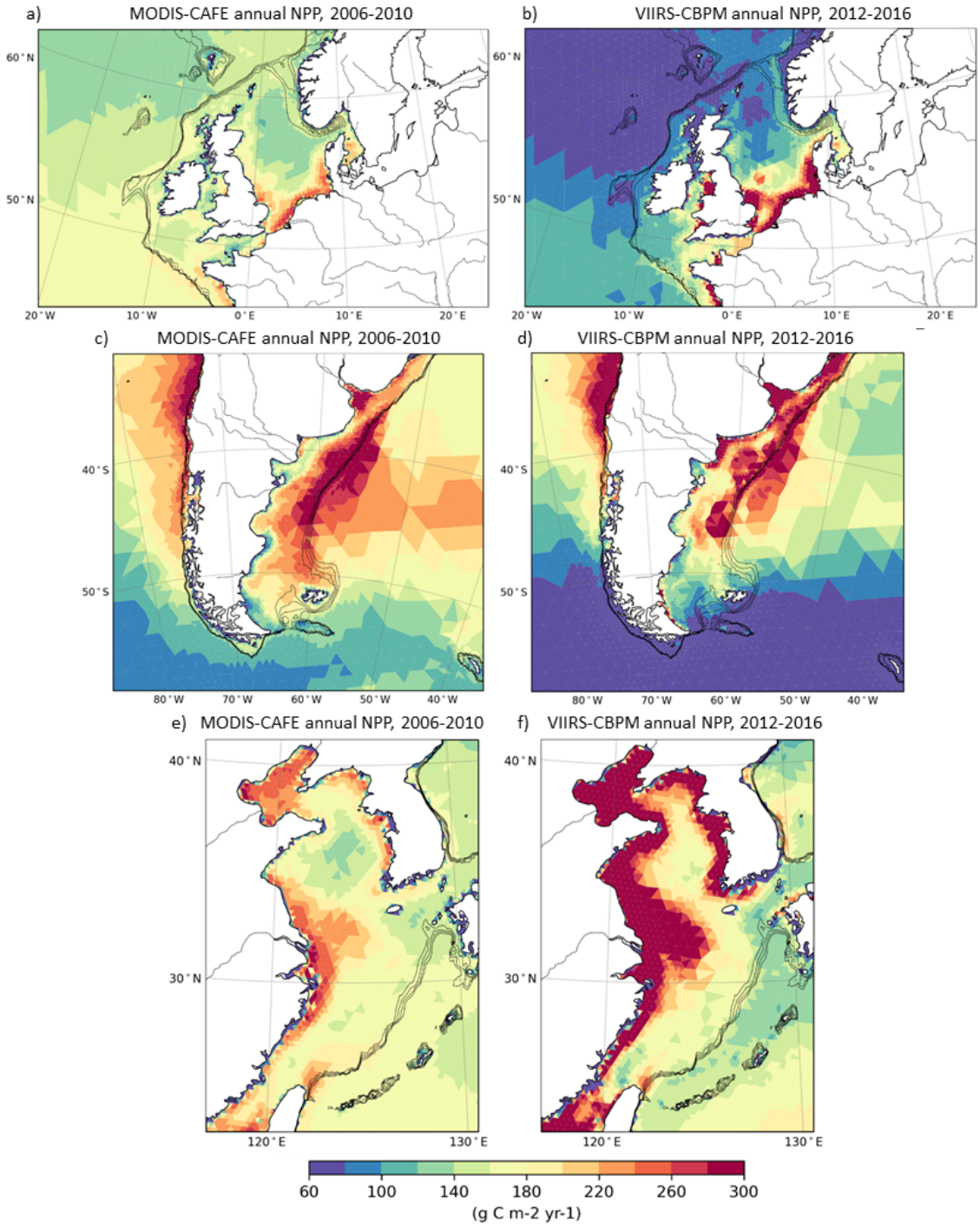

Figure A3: Annual satellite-derived net primary production on the Northwest European Shelf (a,b), Patagonian Shelf (c,d) and East China Shelf (e,f). MODIS-CAFE (Silsbe et al., 2016) product for the period 2006-2010 is shown in (a,c,e), VIIRS-CBPM (Westberry et al., 2008) product for 2012-2016 is shown in (b,d,f), as provided by the Ocean Productivity service (http://sites.science.oregonstate.edu/ocean.productivity/index.php). Data have been interpolated onto the low-res grid of ICON-Coast. Isobaths illustrate the shelf break at water depths of 200-500 m.

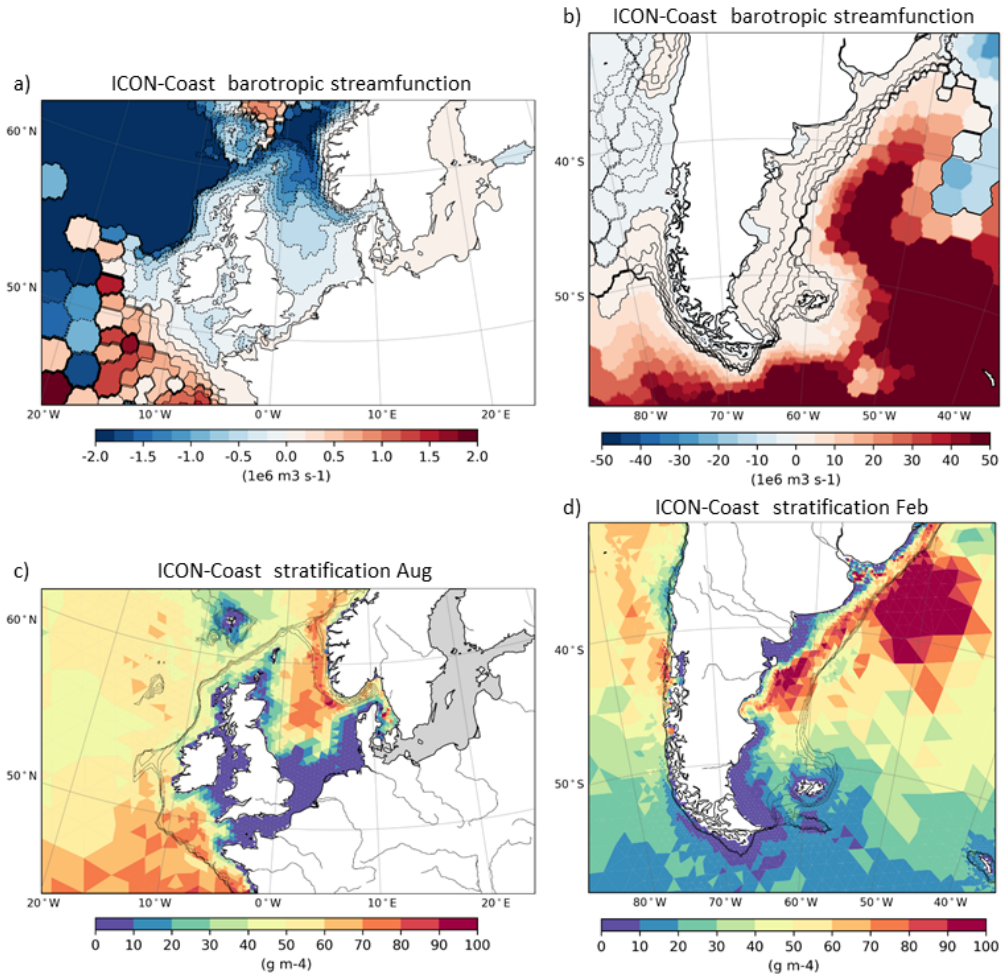

Figure A4: Shelf circulation and seasonal stratification simulated with ICON-Coast low-res configuration: Annual mean barotropic stream function on the Northwest European Shelf (a) and Patagonian Shelf (b). Increments of streamlines are 0.2 Sv for (a) and 0.5 Sv for (b). Hexagonal structures emerge from the calculation and mapping of net volume fluxes through the triangular grid cells. Strength of summer stratification (maximum vertical density gradient) on the Northwest European Shelf (c) and Patagonian Shelf (d). Isobaths illustrate the shelf break at water depths of 200-500 m.

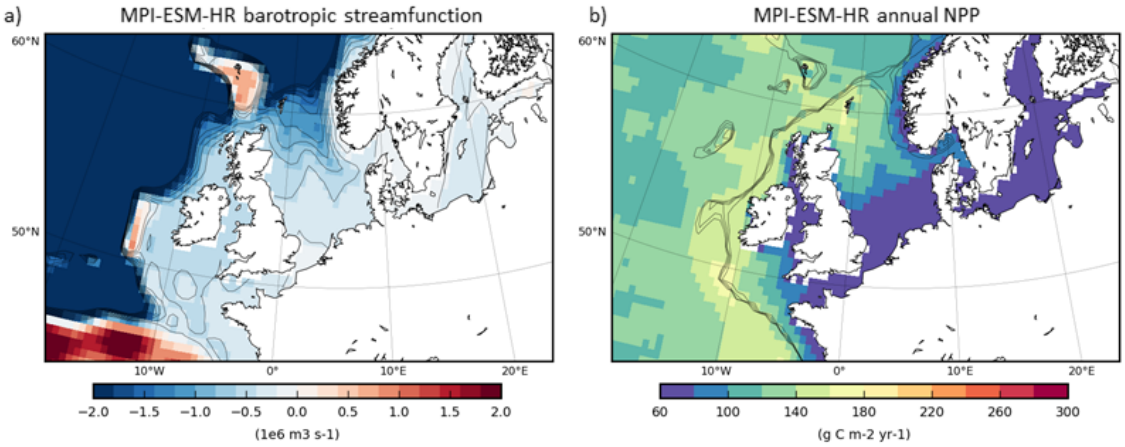

Figure A5: Annual mean barotropic stream function (a) and depth-integrated net primary production (b) on the Northwest European Shelf, simulated with MPI-ESM-HR. Note that the resolution in the shown region is only slightly higher than MPI-ESM-LR (Fig. 6c), due to different grid pole positions in the LR and HR setups. Increments of streamlines in (a) are 0.2 Sv. Isobaths in (b) illustrate the shelf break at water depths of 200-500 m.

References

Aarnos, H., Gélinas, Y., Kasurinen, V., Gu, Y., Puupponen, V. M., & Vähätalo, A. V. (2018). Photochemical Mineralization of Terrigenous DOC to Dissolved Inorganic Carbon in Ocean. *Global Biogeochemical Cycles*, *32*, 250-266. doi: 10.1002/2017GB005698

Acha, E. A., Mianzan, H. W., Guerrero, R. A., Favero, M., & Bava, J. (2004). Marine fronts at the continental shelves of austral South America: Physical and ecological processes. *Journal of Marine Systems*, *44*, 83-105. doi: 10.1016/j.jmarsys.2003.09.005

Acha, M., Mianzan, H., Guerrero, R., Carreto, J., Giberto, D., Montoya, N., & Carignan, M. (2008). An overview of physical and ecological processes in the Rio de la Plata Estuary. *Continental Shelf Research*, *28*, 1579-1588. doi: 10.1016/j.csr.2007.01.031

Algeo, T., & Herrmann, A. (2018). An ancient estuarine-circulation nutrient trap: The Late Pennsylvanian Midcontinent Sea of North America. *Geology*, *46*, 143-146. doi: 10.1130/G39804.1

Allen, J. I., Aiken, J., Anderson, T. R., Buitenhuis, E., Cornell, S., Geider, R. J., ... While, J. (2010). Marine ecosystem models for earth systems applications: The MarQUEST experience. *Journal of Marine Systems*, *81*, 19-33. doi: 10.1016/j.jmarsys.2009.12.017

Amiotte Suchet, P., & Probst, J. L. (1995). A global model for present-day atmospheric/soil CO2 consumption by chemical erosion of continental rocks (GEM-CO2). *Tellus B: Chemical and Physical Meteorology*, *47*, 273-280. doi: 10.3402/tellusb.v47i1-2.16047

Araujo, M., Noriega, C., & Lefèvre, N. (2014). Nutrients and carbon fluxes in the estuaries of major rivers flowing into the tropical Atlantic. *Front. Mar. Sci.*, *1*, 1-16. doi: 10.3389/fmars.2014.00010

Arndt, S., Jørgensen, B. B., Rowe, D. E. L., Middelburg, J. J., Pancost, R. D., & Regnier, P. (2013). Quantifying the degradation of organic matter in marine sediments: A review and synthesis. *Earth-Science Reviews*, *123*, 53-86. doi: 10.1016/j.earscirev.2013.02.008

Arrigo, K., van Dijken, G., & Long, M. (2008). Coastal Southern Ocean: A strong anthropogenic CO_2 sink. *Geophys. Res. Lett.*, *35*, 6 pp. doi: 10.1029/2008GL035624

Arrigo, K. R., & van Dijken, G. L. (2015). Continued increases in Arctic Ocean primary production. *Progr. Oceanogr.*, *136*, 60-70. doi: 10.1016/j.pocean.2015.05.002

Aumont, O., Orr, J. C., Monfray, P., Ludwig, W., Suchet, P. A., & Probst, J. L. (2001). Riverine-driven interhemispheric transport of carbon. *Global Biogeochem. Cy.*, *15*, 393-405. doi: 10.1029/1999GB001238

Babin, M., & Stramski, D. (2004). Variations in the mass-specific absorption coefficient of mineral particles suspended in water. *Limnology and Oceanography*, *49*, 756-767. doi: 10.4319/lo.2004.49.3.0756

Bai, Y., He, X., Pan, D., Chen, C. T. A., Kang, Y., Chen, X., & Cai, W. J. (2014). Summertime Changjiang River plume variation during 1998â€“2010. *Journal of Geophysical Research: Oceans*, *119*, 6238-6257. doi: 10.1002/2014JC009866

Bates, N. R. (2006). Air-sea CO_2 fluxes and the continental shelf pump of carbon in the Chukchi Sea adjacent to the Arctic Ocean. *J. Geophys. Res.*, *111*, 21 pp. doi: 10.1029/2005JC003083

Bates, N. R., & Mathis, J. T. (2009). The Arctic Ocean marine carbon cycle: evaluation of air-sea CO2 exchanges, ocean acidification impacts and potential feedbacks. *Biogeosciences*, *6*, 2433-2459. doi: 10.5194/bg-6-2433-2009

Bauer, J. E., Cai, W. J., Raymond, P. A., Bianchi, T. S., Hopkinson, C. S., & Regnier, P. A. G. (2013). The changing carbon cycle of the coastal ocean. *Nature*, *504*, 61-70. doi: 10.1038/nature12857

Becker, M., Olsen, A., Landschützer, P., Omar, A., Rehder, G., Rödenbeck, C., & Skjelvan, I. (2021). The northern European shelf as an increasing net sink for CO_2. *Biogeosciences*, *18*, 1127-1147. doi: 10.5194/bg-18-1127-2021

Behrens, J., & Bader, M. (2009). Efficiency considerations in triangular adaptive mesh refinement. *Phil. Trans. R. Soc. A.*, *367*, 4577-4589. doi: 10.1098/rsta.2009.0175

Berner, R. A., Lasaga, A. C., & Garrels, R. M. (1983). The carbonate-silicate geochem-

ical cycle and its effect on atmospheric carbon dioxide over the past 100 million years. *American Journal of Science*, *283*, 641-683. doi: 10.2475/ajs.283.7.641

Beusen, A. H. W., Bouwman, A. F., Dürr, H., Dekkers, A. L. M., & Hartmann, J. (2009). Global patterns of dissolved silica export to the coastal zone: Results from a spatially explicit global model. *Global Biogeochem. Cy.*, *23*, GB0A02. doi: 10.1029/2008GB003281

Beusen, A. H. W., Bouwman, A. F., Van Beek, L. P. H., Mogollón, J. M., & Middelburg, J. J. (2016). Global riverine N and P transport to ocean increased during the 20th century despite increased retention along the aquatic continuum. *Biogeosciences*, *13*, 2441-2451. doi: 10.5194/bg-13-2441-2016

Bianchi, A. A., Bianucci, L., Piola, A. R., Pino, D. R., Schloss, I., Poisson, A., & Balestrini, C. F. (2005). Vertical stratification and air-sea CO2 fluxes in the Patagonian shelf. *Journal of Geophysical Research: Oceans*, *110*, 11 pp. doi: 10.1029/2004JC002488

Birol, F., Fuller, N., Lyard, F., Cancet, M., Niño, F., Delebecque, C., ... Léger, F. (2017). Coastal applications from nadir altimetry: Example of the X-TRACK regional products. *Advances in Space Research*, *59*, 936-953. doi: 10.1016/j.asr.2016.11.005

Borges, D. B., A. V., & Frankignoulle, M. (2005). Budgeting sinks and sources of CO_2 in the coastal ocean: Diversity of ecosystems counts. *Geophys. Res. Lett.*, *32*, L14601. doi: 10.1029/2005GL023053

Bourgeois, T., Orr, J. C., Resplandy, L., Terhaar, J., Ethé, C., Gehlen, M., & Bopp, L. (2016). Coastal-ocean uptake of anthropogenic carbon. *Biogeosciences*, *13*, 4167-4185. doi: 10.5194/bg-13-4167-2016

Boyd, P. W., Sundby, S., & Pörtner, H. O. (2014). Cross-chapter box on net primary production in the ocean. In C. B. Field et al. (Eds.), *Climate change 2014: Impacts, adaptation, and vulnerability. part a: Global and sectoral aspects. contribution of working group ii to the fifth assessment report of the intergovernmental panel on climate change* (p. 133-136). Cambridge, United Kingdom and New York, NY, USA: Cambridge University Press.

Boyer, T. P., García, H. E., Locarnini, R. A., Zweng, M. M., Mishonov, A. V., Reagan, J. R., ... Smolyar, I. V. (2018). World Ocean Atlas 2018 (2005-2017). *NOAA National Centers for Environmental Information*, https://www.ncei.noaa.gov/archive/accession/NCEI-WOA18.

Brink, K. H. (2016). Cross-Shelf Exchange. *Annual Review of Marine Science*, *8*, 59-78. doi: 10.1146/annurev-marine-010814-015717

Buitenhuis, E. T., Hashioka, T., & Quéré, C. L. (2013). Combined constraints on global ocean primary production using observations and models. *Global Biogeochemical Cycles*, *27*, 847-858. doi: 10.1002/gbc.20074

Burdige, D. J. (2007). Preservation of Organic Matter in Marine Sediments: Controls, Mechanisms, and an Imbalance in Sediment Organic Carbon Budgets? *Chem. Rev.*, *107*, 467-485. doi: 10.1021/cr050347q

Bushinsky, S. M., Landschützer, P., Rödenbeck, C., Gray, A. R., Baker, D., Mazloff, M. R., ... Sarmiento, J. L. (2019). Reassessing Southern Ocean Air-Sea CO2 Flux Estimates With the Addition of Biogeochemical Float Observations. *Global Biogeochemical Cycles*, *33*, 1370-1388. doi: 10.1029/2019GB006176

Cadier, M., Gorgues, T., L'Helguen, S., Sourisseau, M., & Memery, L. (2017). Tidal cycle control of biogeochemical and ecological properties of a macrotidal ecosystem. *Geophys. Res. Lett.*, *44*, 8453-8462. doi: 10.1002/2017GL074173

Cai, W. J. (2011). Estuarine and coastal ocean carbon paradox: CO_2 sinks or sites of terrestrial carbon incineration? *Ann. Rev. Mar. Sci.*, *3*, 123-145. doi: 10.1146/annurev-marine-120709-142723

Cai, W. J., Chen, L., Chen, B., Gao, Z., Lee, S. H., Chen, J., ... Zhang, H. (2010). Decrease in the CO_2 Uptake Capacity in an Ice-Free Arctic Ocean Basin. *Science*, *329*, 556-559. doi: 10.1126/science.1189338

Campbell, J., Antoine, D., Armstrong, R., Arrigo, K., Balch, W., Barber, R., ... Yoder, J. (2002). Comparison of algorithms for estimating ocean primary production from surface chlorophyll, temperature, and irradiance. *Global Biogeochemical Cycles*, *16*, 15 pp. doi:

10.1029/2001GB001444

Canadell, J. G., Ciais, P., Dhakal, S., Dolman, H., Friedlingstein, P., Gurney, K. R., ... Raupach, M. R. (2010). Interactions of the carbon cycle, human activity, and the climate system: a research portfolio. *Current Opinion in Environmental Sustainability*, *2*, 301-311. doi: 10.1016/j.cosust.2010.08.003

Cao, Z., Yang, W., Zhao, Y., Guo, X., Yin, Z., Du, C., ... Dai, M. (2020). Diagnosis of CO2 dynamics and fluxes in global coastal oceans. *National Science Review*, *7*, 786-797. doi: 10.1093/nsr/nwz105

Capuzzo, E., Lynam, C. P., Barry, J., Stephens, D., Forster, R. M., Greenwood, N., ... Engelhard, G. H. (2018). A decline in primary production in the North Sea over 25 years, associated with reductions in zooplankton abundance and fish stock recruitment. *Global Change Biology*, *24*, 352-364.

Carless, S. J., Green, J. A. M., Pelling, H. E., & Wilmes, S. B. (2016). Effects of future sea-level rise on tidal processes on the Patagonian Shelf. *Journal of Marine Systems*, *163*, 113-124. doi: 10.1016/j.jmarsys.2016.07.007

Carr, M. E., Friedrichs, M. A. M., Schmeltz, M., Noguchi-Aita, M., Antoine, D., Arrigo, K. R., ... Yamanaka, Y. (2006). A comparison of global estimates of marine primary production from ocean color. *Deep Sea Research Part II: Topical Studies in Oceanography*, *53*, 741-770. doi: 10.1016/j.dsr2.2006.01.028

Carreto, J. I., Montoya, N. G., Carignan, M. O., Akselman, R., Acha, E. M., & Derisio, C. (2016). Environmental and biological factors controlling the spring phytoplankton bloom at the Patagonian shelf-break front - Degraded fucoxanthin pigments and the importance of microzooplankton grazing. *Progress in Oceanography*, *146*, 1-21. doi: 10.1016/j.pocean.2016.05.002

Chen, C., Liu, H., & Beardsley, R. C. (2003). An unstructured grid, finite-volume, three-dimensional, primitive equations ocean model: Application to coastal ocean and estuaries. *Journal of Atmospheric and Oceanic Technology*, *20*, 159-186. doi: 10.1175/1520-0426(2003)020⟨0159:AUGFVT⟩2.0.CO;2

Chen, H. W., Liu, C. T., Matsuno, T., Ichikawa, K., Fukudome, K., Yang, Y., ... Tsai, W. L. (2016). Temporal variations of volume transport through the Taiwan Strait, as identified by three-year measurements. *Cont. Shelf Res.*, *114*, 41-53. doi: 10.1016/j.csr.2015.12.010

Cheng, Y., Putrasahan, D., Beal, L., & Kirtman, B. (2016). Quantifying Agulhas Leakage in a High-Resolution Climate Model. *Journal of Climate*, *29*, 6881-6892. doi: 10.1175/JCLI-D-15-0568.1

Clark, M., Marsh, R., & Harle, J. (2021). Weakening and warming of the European Slope Current since the late 1990s attributed to basin-scale density changes. *Ocean Science Discussions*, 32 pp. doi: 10.5194/os-2021-60

Combes, V., & Matano, R. P. (2018). The Patagonian shelf circulation: Drivers and variability. *Progress in Oceanography*, *167*, 24-43.

Combes, V., Matano, R. P., & Palma, E. D. (2021). Circulation and cross-shelf exchanges in the northern shelf region of the southwestern Atlantic: Kinematics. *Journal of Geophysical Research: Oceans*, *126*, 16 pp. doi: 10.1029/2020JC016959

Compton, J., Mallinson, D., Glenn, C. R., Filippelli, G., Follmi, K., Shields, G., & Zanin, Y. (2000). Variations in the Global Phosphoruscycle. In *Marine authigenesis: From global to microbial.* SEPM Society for Sedimentary Geology. doi: 10.2110/pec.00.66.0021

Dai, M., Cao, Z., Guo, X., Zhai, W., Liu, Z., Yin, Z., ... Du, C. (2013). Why are some marginal seas sources of atmospheric CO2? *Geophysical Research Letters*, *40*, 2154-2158. doi: doi.org/10.1002/grl.50390

Dale, A. C., & Inall, M. E. (2015). Tidal mixing processes amid small-scale, deep-ocean topography. *Geophysical Research Letters*, *42*, 484-491. doi: 10.1002/2014GL062755

Danilov, S. (2010). On utility of triangular C-grid type discretization for numerical modeling of large-scale ocean flows. *Ocean Dynamics*, *60*, 1361-1369. doi: 10.1007/s10236-010-0339-6

Danilov, S., Wang, Q., Timmermann, R., Iakovlev, N., Sidorenko, D., Kimmritz, M., ...

Schröter, J. (2015). Finite-element sea ice model (FESIM), version 2. *Geosci. Model. Dev.*, *8*, 1747-1761. doi: 10.5194/gmd-8-1747-2015

Dee, D. P., Uppala, S. M., Simmons, A. J., Berrisford, P., Poli, P., Kobayashi, S., ... Vitart, F. (2011). The ERA-Interim reanalysis: configuration and performance of the data assimilation system. *Quarterly Journal of the Royal Meteorological Society*, *137*, 553-597. doi: 10.1002/qj.828

de Souza, M. M., Mathis, M., Mayer, B., Noernberg, M. A., & Pohlmann, T. (2020). Possible impacts of anthropogenic climate change to the upwelling in the South Brazil Bight. *Climate Dynamics*, *55*, 651-664. doi: 10.1007/s00382-020-05289-0

DeVries, T., & Weber, T. (2017). The export and fate of organic matter in the ocean: New constraints from combining satellite and oceanographic tracer observations. *Global Biogeochemical Cycles*, *31*, 535-555. doi: 10.1002/2016GB005551

Diesing, M., Kröger, S., Parker, R., Jenkins, C., Mason, C., & Weston, K. (2017). Predicting the standing stock of organic carbon in surface sediments of the North-West European continental shelf. *Biogeochemistry*, *135*, 183-200. doi: 10.1007/s10533-017-0310-4

Diesing, M., Thorsnes, T., & Bjarnadóttir, L. R. (2021). Organic carbon densities and accumulation rates in surface sediments of the North Sea and Skagerrak. *Biogeosciences*, *18*, 2139-2160. doi: 10.5194/bg-18-2139-2021

Dixit, S., van Cappellen, P., & van Bennekom, A. J. (2001). Processes controlling solubility of biogenic silica and pore water build-up of silicic acid in marine sediments. *Marine Chemistry*, *73*, 333-352. doi: 10.1016/S0304-4203(00)00118-3

Doddridge, E. W., & Marshall, D. P. (2018). Implications of Eddy Cancellation for Nutrient Distribution Within Subtropical Gyres. *Journal of Geophysical Research: Oceans*, *123*, 6720-6735. doi: 10.1029/2018JC013842

Duarte, C. M., Middelburg, J. J., & Caraco, N. (2005). Major role of marine vegetation on the oceanic carbon cycle. *Biogeosciences*, *2*, 1-8. doi: 10.5194/bg-2-1-2005

Dürr, H. H., Meybeck, M., Hartmann, J., Laruelle, G. G., & Roubeix, V. (2011). Global spatial distribution of natural riverine silica inputs to the coastal zone. *Biogeosciences*, *8*, 597-620. doi: 10.5194/bg-8-597-2011

Egbert, G. D., & Erofeeva, S. Y. (2002). Efficient inverse modeling of barotropic ocean tides. *J. Atmos. Ocean. Technol.*, *19*, 183-204. doi: 10.1175/1520-0426(2002)019⟨0183:EIMOBO⟩2.0.CO;2

Ekici, A., Beer, C., Hagemann, S., Boike, J., Langer, M., & Hauck, C. (2014). Simulating high-latitude permafrost regions by the JSBACH terrestrial ecosystem model. *Geoscientific Model Development*, *7*, 631-647. doi: 10.5194/gmd-7-631-2014

Eyring, V., Bony, S., Meehl, G. A., Senior, C. A., Stevens, B., Stouffer, R. J., & Taylor, K. E. (2016). Overview of the coupled model intercomparison project phase 6 (CMIP6) experimental design and organization. *Geoscient. Model. Dev.*, *9*, 1937-1958. doi: 10.5194/gmd-9-1937-2016

Fennel, K., Alin, S., Barbero, L., Evans, W., Bourgeois, T., Cooley, S., ... Wang, Z. A. (2019). Carbon cycling in the North American coastal ocean: a synthesis. *Biogeosciences*, *16*, 1281-1304. doi: 10.5194/bg-16-1281-2019

Fettweis, M., Baeye, M., Van der Zande, D., Van den Eynde, D., & Lee, B. J. (2014). Seasonality of floc strength in the southern North Sea. *Journal of Geophysical Research: Oceans*, *119*, 1911-1926. doi: 10.1002/2013JC009750

Fichot, C. G., & Benner, R. (2014). The fate of terrigenous dissolved organic carbon in a riverinfluenced ocean margin. *Global Biogeochemical Cycles*, *28*, 300-318. doi: 10.1002/2013GB004670

Franco, B. C., Palma, E. D., Combes, V., & Lasta, M. L. (2017). Physical processes controlling passive larval transport at the Patagonian Shelf Break Front. *Journal of Sea Research*, *124*, 17-25. doi: 10.1016/j.seares.2017.04.012

Francois, R., Honjo, S., Krishfield, R., & Manganini, S. (2002). Factors controlling the flux of organic carbon to the bathypelagic zone of the ocean. *Global Biogeochemical Cycles*, *16*, 20 pp. doi: 10.1029/2001GB001722

Franzo, A., Celussi, M., Bazzaro, M., Relitti, F., & Negro, P. D. (2019). Microbial processing of sedimentary organic matter at a shallow LTER site in the northern Adriatic Sea: an 8-year case study. *Nature Conservation*, *34*, 397-415. doi: 10.3897/natureconservation .34.30099

Frey, D., Piola, A., Krechik, V., Fofanov, D. V., Morozov, E. G., Silvestrova, K., ... Gladyshev, S. V. (2021). Direct Measurements of the Malvinas Current Velocity Structure. *Journal of Geophysical Research: Oceans*, *126*. doi: 10.1029/2020JC016727

Friedlingstein, P., O'Sullivan, M., Jones, M. W., Andrew, R. M., Hauck, J., Olsen, A., ... Zaehle, S. (2020). Global Carbon Budget 2020. *Earth System Science Data*, *12*, 3269-3340. doi: 10.5194/essd-12-3269-2020

Galy, V., Peucker-Ehrenbrink, B., & Eglinton, T. (2015). Global carbon export from the terrestrial biosphere controlled by erosion. *Nature*, *521*, 204-207. doi: 10.1038/nature14400

Gaspar, P., Grégoris, Y., & Lefevre, J. M. (1990). A simple eddy kinetic energy model for simulations of the oceanic vertical mixing: Tests at station Papa and long-term upper ocean study site. *Journal of Geophysical Research: Oceans*, *95*, 16179-16193. doi: 10.1029/JC095iC09p16179

Gattuso, J. P., Frankignoulle, M., & Wollast, R. (1998). Carbon and carbonate metabolism in coastal aquatic ecosystems. *Annual Review of Ecology and Systematics*, *29*, 405-434. doi: 10.1146/annurev.ecolsys.29.1.405

Gille, S. T., Metzger, E. J., & Tokmakian, R. (2004). Seafloor topography and ocean circulation. *Oceanography*, *17*, 47-54. doi: 10.5670/oceanog.2004.66

Giorgetta, M. A., Jungclaus, J., Reick, C. H., Legutke, S., Bader, J., Böttinger, M., ... Stevens, B. (2013). Climate and carbon cycle changes from 1850 to 2100 in MPI-ESM simulations for the Coupled Model Intercomparison Project phase 5. *Journal of Advances in Modeling Earth Systems*, *5*(3), 572-597.

Gloege, L., McKinley, G. A., Mouw, C. B., & Ciochetto, A. B. (2017). Global evaluation of particulate organic carbon flux parameterizations and implications for atmospheric pCO_2. *Global Biogeochem. Cycles*, *31*, 1192-1215. doi: 10.1002/2016GB005535

Gonçalves-Araujo, R., de Souza, M. S., Mendes, C. R. B., Tavano, V. M., & Garcia, C. A. E. (2016). Seasonal change of phytoplankton (spring vs. summer) in the southern Patagonian shelf. *Continental Shelf Research*, *124*, 142-152. doi: 10.1016/j.csr.2016.03.023

Graham, J. A., O'Dea, E., Holt, J., Polton, J., Hewitt, H. T., Furner, R., ... Mayorga Adame, C. G. (2018a). AMM15: a new high resolution NEMO configuration for operational simulation of the European north-west shelf. *Geoscientific Model Development*, *11*, 681-696. doi: 10.5194/gmd-11-681-2018

Graham, J. A., Rosser, J. P., O'Dea, E., & Hewitt, H. T. (2018b). Resolving Shelf Break Exchange Around the European Northwest Shelf. *Geophysical Research Letters*, *45*, 12386-12395.

Gregor, L., Lebehot, A. D., Kok, S., & Scheel Monteiro, P. M. (2019). A comparative assessment of the uncertainties of global surface ocean CO2 estimates using a machine-learning ensemble (CSIR-ML6 version 2019a) – have we hit the wall? *Geoscientific Model Development*, *12*, 5113-5136. doi: 10.5194/gmd-12-5113-2019

Gröger, M., Maier-Reimer, E., Mikolajewicz, U., Moll, A., & Sein, D. (2013). NW European shelf under climate warming: implications for open ocean - shelf exchange, primary production, and carbon absorption. *Biogeosciences*, *10*, 3767-3792.

Gruber, N. (2015). Ocean biogeochemistry: Carbon at the coastal interface. *Nature*, *517*(7533), 148-149. doi: 10.1038/nature14082

Guidi, L., Legendre, L., Reygondeau, G., Uitz, J., Stemmann, L., & Henson, S. A. (2015). A new look at ocean carbon remineralization for estimating deepwater sequestration. *Global Biogeochem. Cycles*, *29*, 1044-1059. doi: 10.1002/2014GB005063

Guihou, K., Piola, A. R., Palma, E. D., & Chidichimo, M. P. (2020). Dynamical connections between large marine ecosystems of austral South America based on numerical simulations. *Ocean Science*, *16*, 271-290. doi: 10.5194/os-16-271-2020

Guihou, K., Polton, J., Harle, J., Wakelin, S., O'Dea, E., & Holt, J. (2018). Kilometric Scale Modeling of the North West European Shelf Seas: Exploring the Spatial and Temporal Variability of Internal Tides. *Journal of Geophysical Research: Oceans*, *123*, 688-707. doi: 10.1002/2017JC012960

Gutjahr, O., Brüggemann, N., Haak, H., Jungclaus, J., Putrasahan, D., Lohmann, K., & von Storch, J. (2021). Comparison of ocean vertical mixing schemes in the Max Planck Institute Earth System Model (MPI-ESM1.2). *Geophysical Model Development*, *14*, 2317-2349. doi: 10.5194/gmd-14-2317-2021

Hagemann, S., & Dümenil-Gates, L. (2001). Validation of the hydrological cycle of ECMWF and NCEP reanalyses using the MPI hydrological discharge model. *Journal of Geophysical Research - Atmospheres*, *106*, 1503-1510.

Hagemann, S., Stacke, T., & Ho-Hagemann, H. T. M. (2020). High Resolution Discharge Simulations Over Europe and the Baltic Sea Catchment. *Frontiers in Earth Science*, *8*, 12 pp. doi: 10.3389/feart.2020.00012

Hallberg, R. (2013). Using a resolution function to regulate parameterizations of oceanic mesoscale eddy effects. *Ocean Modelling*, *72*, 92-103. doi: 10.1016/j.ocemod.2013.08.007

Hartmann, J., Jansen, N., Dürr, H. H., Kempe, S., & Köhler, P. (2009). Global CO2-consumption by chemical weathering: What is the contribution of highly active weathering regions? *Global and Planetary Change*, *69*, 185-194. doi: 10.1016/j.gloplacha.2009.07.007

Hátún, H., Azetsu-Scott, K., Somavilla, R., Rey, F., Johnson, C., Mathis, M., ... Ólafsson, J. (2017). The subpolar gyre regulates silicate concentrations in the North Atlantic. *Scientific Reports*, *7*(14576), 9 pp.

Hauck, J., Zeising, M., Quéré, C. L., Gruber, N., Bakker, D. C. E., Bopp, L., ... Séférian, R. (2020). Consistency and Challenges in the Ocean Carbon Sink Estimate for the Global Carbon Budget. *Frontiers in Marine Science*, *7*, 22 pp. doi: 10.3389/fmars.2020.571720

Heinze, C., Maier-Reimer, E., Winguth, A. M. E., & Archer, D. (1999). A global oceanic sediment model for long-term climate studies. *Global Biogeochem. Cycles*, *13*, 221-250.

Hewitt, H. T., Bell, M. J., Chassignet, E. P., Czaja, A., Ferreira, D., Griffies, S. M., ... Roberts, M. J. (2017). Will high-resolution global ocean models benefit coupled predictions on short-range to climate timescales? *Ocean Modelling*, *120*, 120-136. doi: 10.1016/j.ocemod.2017.11.002

Hewitt, H. T., Roberts, M., Mathiot, P., Biastoch, A., Blockley, E., Chassignet, E. P., ... Zhang, Q. (2020). Resolving and Parameterising the Ocean Mesoscale in Earth System Models. *Curr. Clim. Change Rep.*, *6*, 137-152. doi: 10.1007/s40641-020-00164-w

Hoch, K. E., Petersen, M. R., Brus, S. R., Engwirda, D., Roberts, A. F., Rosa, K. L., & Wolfram, P. J. (2020). MPAS-Ocean Simulation Quality for Variable-Resolution North American Coastal Meshes. *Journal of Advances in Modeling Earth Systems*, *12*, 23 pp. doi: 10.1029/2019MS001848

Holt, J., Butenschön, M., Wakelin, S. L., Artioli, Y., & Allen, J. I. (2012). Oceanic controls on the primary production of the northwest European continental shelf: model experiments under recent past conditions and a potential future scenario. *Biogeosciences*, *9*(1), 97-117.

Holt, J., Harle, J., Proctor, R., Michel, S., Ashworth, M., Batstone, C., ... Smith, G. (2009). Modelling the global coastal ocean. *Philosophical Transactions of the Royal Society A: Mathematical, Physical and Engineering Sciences*, *367*, 939-951. doi: 10.1098/rsta.2008.0210

Holt, J., Hyder, P., Ashworth, M., Harle, J., Hewitt, H. T., Liu, H., ... Wood, R. (2017). Prospects for improving the representation of coastal and shelf seas in global ocean models. *Geoscientific Model Development*, *10*, 499-523. doi: 10.5194/gmd-10-499-2017

Holt, J., & Proctor, R. (2008). The seasonal circulation and volume transport on the northwest European continental shelf: A fine-resolution model study. *J. Geophys. Res.*, *113*, 20 pp. doi: 10.1029/2006JC004034

Holt, J., Schrum, C., Cannaby, H., Daewel, U., Allen, I., Artioli, Y., ... Wakelin, S. (2016).

Potential impacts of climate change on the primary production of regional seas: A comparative analysis of five European seas. *Progress in Oceanography*, *140*, 91-115.

Hu, J., Kawamura, H., Li, C., Hong, H., & Jiang, Y. (2010). Review on current and seawater volume transport through the Taiwan Strait. *Journal of Oceanography*, *66*, 591-610. doi: 10.1007/s10872-010-0049-1

Hu, L. M., Lin, T., Shi, X. F., Yang, Z. S., Wang, H. J., Zhang, G., & Guo, Z. G. (2011). The role of shelf mud depositional process and large river inputs on the fate of organochlorine pesticides in sediments of the Yellow and East China seas. *Geophysical Research Letters*, *38*, 6 pp. doi: 10.1029/2010GL045723

Huang, W. J., Cai, W. J., Wang, Y., Lohrenz, S. E., & Murrell, M. C. (2015). The carbon dioxide system on the Mississippi River-dominated continental shelf in the northern Gulf of Mexico: 1. Distribution and air-sea CO_2 flux. *Journal of Geophysical Research: Oceans*, *120*, 1429-1445. doi: 10.1002/2014JC010498

Hurd, D. C. (1972). Factors affecting solution rate of biogenic opal in seawater. *Earth and Planetary Science Letters*, *15*, 411-417. doi: 10.1016/0012-821X(72)90040-4

Ilyina, T., Six, K. D., Segschneider, J., Maier-Reimer, E., Li, H., & Núñez-Riboni, I. (2013). The global ocean biogeochemistry model HAMOCC: Model architecture and performance as component of the MPI-Earth System Model in different CMIP5 experimental realizations. *Journal of Advances in Modeling Earth Systems*, *5*, 287-315.

Jersild, A., Delawalla, S., & Ito, T. (2021). Mesoscale eddies regulate seasonal iron supply and carbon drawdown in the Drake Passage. *Geophysical Research Letters*, *48*, e2021GL096020. doi: 10.1029/2021GL096020

Jiao, N., Liang, Y., Zhang, Y., Liu, J., Zhang, Y., Zhang, R., ... Zhang, S. (2018). Carbon pools and fluxes in the China Seas and adjacent oceans. *Science China Earth Sciences*, *61*, 1535-1563. doi: 10.1007/s11430-018-9190-x

Kahl, L. C., Bianchi, A. A., Osiroff, A. P., Pino, D. R., & Piola, A. R. (2017). Distribution of sea-air CO_2 fluxes in the Patagonian Sea: Seasonal, biological and thermal effects. *Continental Shelf Research*, *143*, 18-28. doi: 10.1016/j.csr.2017.05.011

Kaiser, K., Benner, R., & W., A. R. M. (2017). The fate of terrigenous dissolved organic carbon on the Eurasian shelves and export to the North Atlantic. *Scientific Reports*, *7*, 11 pp. doi: 10.1038/s41598-017-12729-1

Kamatani, A. (1982). Dissolution rates of silica from diatoms decomposing at various temperatures. *Marine Biology*, *68*, 91-96. doi: 10.1007/BF00393146

Kämpf, J. (2021). On the upslope sediment transport at continental margins. *Journal of Marine Systems*, *219*, 103546. doi: 10.1016/j.jmarsys.2021.103546

Kandasamy, S., & Nath, B. N. (2016). Perspectives on the Terrestrial Organic Matter Transport and Burial along the Land-Deep Sea Continuum: Caveats in Our Understanding of Biogeochemical Processes and Future Needs. *Front. Mar. Sci.*, *3*, 18 pp. doi: 10.3389/fmars.2016.00259

Karakaş, G., Nowald, N., Blaas, M., Marchesiello, P., Frickenhaus, S., & Schlitzer, R. (2006). High-resolution modeling of sediment erosion and particle transport across the northwest African shelf. *J. Geophys. Res.*, *111*, 13 pp. doi: 10.1029/2005JC003296

Kartadikaria, A. R., Watanabe, A., Nadaoka, K., Adi, N. S., Prayitno, H. B., Soemorumekso, S., ... Khasanah, E. N. (2015). CO_2 sink/source characteristics in the tropical Indonesian seas. *Journal of Geophysical Research: Oceans*, *120*, 7842-7856. doi: 10.1002/2015JC010925

Kastner, S. E., Horner-Devine, A. R., & Thomson, J. (2018). The influence of wind and waves on spreading and mixing in the Fraser River plume. *Journal of Geophysical Research: Oceans*, *123*, 6818-6840. doi: 10.1029/2018JC013765

Ke, Z., & Yankovsky, A. (2010). The Hybrid Kelvin-Edge Wave and Its Role in Tidal Dynamic. *Journal of Physical Oceanography*, *40*, 2757-2767. doi: 10.1175/2010JPO4430.1

Kealoha, A. K., Shamberger, K. E. F., DiMarco, S. F., Thyng, K. M., Hetland, R. D., Manzello, D. P., ... Enochs, I. C. (2020). Surface Water CO_2 variability in the Gulf of

Mexico (1996-2017). *Scientific Reports*, *10*, 13 pp. doi: 10.1038/s41598-020-68924-0

Kerimoglu, O., Voynova, Y. G., Chegini, F., Brix, H., Callies, U., Hofmeister, R., ... van Beusekom, J. E. E. (2020). Interactive impacts of meteorological and hydrological conditions on the physical and biogeochemical structure of a coastal system. *Biogeosciences*, *17*, 5097-5127. doi: 10.5194/bg-17-5097-2020

Kitidis, V., Shutler, J. D., Ashton, I., Warren, M., Brown, I., Findlay, H., ... Nightingale, P. D. (2019). Winter weather controls net influx of atmospheric CO2 on the north-west European shelf. *Scientific Reports*, *9*, 11 pp. doi: 10.1038/s41598-019-56363-5

Kloster, S., Feichter, J., Maier-Reimer, E., Six, K. D., Stier, P., & Wetzel, P. (2006). DMS cycle in the marine ocean-atmosphere system - A global model study. *Biogeosciences*, *3*, 29-51.

Knutti, R., Stocker, T. F., & Wright, D. G. (1999). The Effects of Subgrid-Scale Parameterizations in a Zonally Averaged Ocean Model. *Journal of Physical Oceanography*, *30*, 2738-2752.

Korn, P. (2017). Formulation of an unstructured grid model for global ocean dynamics. *J. Comput. Phys.*, *339*, 525-552. doi: 10.1016/j.jcp.2017.03.009

Korn, P. (2018). A structure-preserving discretization of ocean parametrizations on unstructured grids. *Ocean Modelling*, *132*, 73-90. doi: 10.1016/j.ocemod.2018.10.002

Korn, P., & Linardakis, L. (2018). A conservative discretization of the shallow-water equations on triangular grids. *J. Comput. Phys.*, *375*, 871â€“900. doi: 10.1016/j.jcp .2018.09.002

Koul, V., Schrum, C., Düsterhus, A., & Baehr, J. (2019). Atlantic Inflow to the North Sea Modulated by the Subpolar Gyre in a Historical Simulation With MPI-ESM. *Journal of Geophysical Research: Oceans*, *124*, 1807-1826. doi: 10.1029/2018JC014738

Krumins, V., Gehlen, M., Arndt, S., Cappellen, P. V., & Regnier, P. (2013). Dissolved inorganic carbon and alkalinity fluxes from coastal marine sediments: model estimates for different shelf environments and sensitivity to global change. *Biogeosciences*, *10*, 371-398. doi: 10.5194/bg-10-371-2013

Kühn, W., Pätsch, J., Thomas, H., Borges, A. V., Schiettecatte, L.-S., Bozec, Y., & Prowe, A. E. F. (2010). Nitrogen and carbon cycling in the North Sea and exchange with the North Atlantic - A model study, Part II: Carbon budget and fluxes. *Continental Shelf Research*, *30*, 1701-1716.

Kulk, G., Platt, T., Dingle, J., Jackson, T., Jönsson, B. F., Bouman, H. A., ... Sathyendranath, S. (2020). Primary Production, an Index of Climate Change in the Ocean: Satellite-Based Estimates over Two Decades. *Remote Sensing*, *12*, 26 pp. doi: 10.3390/ rs12050826

Kwon, E. Y., Primeau, F., & Sarmiento, J. L. (2009). The impact of remineralization depth on the air-sea carbon balance. *Nature Geoscience*, *2*, 630-635. doi: 10.1038/ngeo612

Lacroix, F., Ilyina, T., & Hartmann, J. (2020). Oceanic CO_2 outgassing and biological production hotspots induced by pre-industrial river loads of nutrients and carbon in a global modeling approach. *Biogeosciences*, *17*, 55-88. doi: 10.5194/bg-17-55-2020

Lacroix, F., Ilyina, T., Laruelle, G. G., & Regnier, P. (2021a). Reconstructing the Preindustrial Coastal Carbon Cycle Through a Global Ocean Circulation Model: Was the Global Continental Shelf Already Both Autotrophic and a CO2 Sink? *Global Biogeochemical Cycles*, *35*, e2020GB006603. doi: 10.1029/2020GB006603

Lacroix, F., Ilyina, T., Mathis, M., Laruelle, G. G., & Regnier, P. (2021b). Historical Increases in Land-Derived Nutrient Inputs May Alleviate Effects of a Changing Physical Climate on the Oceanic Carbon Cycle. *Global Change Biology*, in press. doi: 10.1111/ gcb.15822

Landschützer, P., Gruber, N., & Bakker, D. C. E. (2016). Decadal variations and trends of the global ocean carbon sink. *Global Biogeochemical Cycles*, *30*, 1396-1417. doi: 10.1002/2015GB005359

Laruelle, G., Lauerwald, R., Pfeil, B., & Regnier, P. (2014). Regionalized global budget of the CO_2 exchange at the air-water interface in continental shelf seas. *Global Biogeochem-*

ical Cycles, *28*(11), 1199-1214. doi: 10.1002/2014GB004832

Laruelle, G. G., Cai, W. J., Hu, X., Gruber, N., Mackenzie, F. T., & Regnier, P. (2018). Continental shelves as a variable but increasing global sink for atmospheric carbon dioxide. *Nature Communications*, *9*, 11 pp. doi: 10.1038/s41467-017-02738-z

Laruelle, G. G., Dürr, H. H., Slomp, C. P., & Borges, A. V. (2010). Evaluation of sinks and sources of CO_2 in the global coastal ocean using a spatially-explicit typology of estuaries and continental shelves. *Geophysical Research Letters*, *37*, L15607. doi: 10.1029/2010GL043691

Laufkötter, C., John, J. G., Stock, C. A., & Dunne, J. P. (2017). Temperature and oxygen dependence of the remineralization of organic matter. *Global Biogeochem. Cycles*, *31*, 1038-1050. doi: 10.1002/2017GB005643

Laufkötter, C., Vogt, M., Gruber, N., Aita-Noguchi, M., Aumont, O., Bopp, L., ... Völker, C. (2015). Drivers and uncertainties of future global marine primary production in marine ecosystem models. *Biogeosciences*, *12*, 6955-6984. doi: 10.5194/bg-12-6955-2015

Lavelle, J. W., Thurnherr, A. M., Mullineaux, L. S., McGillicuddy, D. J., & Ledwell, J. R. (2012). The Prediction, Verification, and Significance of Flank Jets at Mid-Ocean Ridges. *Oceanography*, *25*, 277-283.

Lee, T. R., Wood, W. T., & Phrampus, B. J. (2019). A Machine Learning (kNN) Approach to Predicting Global Seafloor Total Organic Carbon. *Global Biogeochemical Cycles*, *33*, 37-46. doi: 10.1029/2018GB005992

Legge, O., Johnson, M., Hicks, N., Jickells, T., Diesing, M., Aldridge, J., ... Williamson, P. (2020). Carbon on the Northwest European Shelf: Contemporary Budget and Future Influences. *Frontiers in Marine Science*, *7*, 23 pp. doi: 10.3389/fmars.2020.00143

Lemmen, C. (2018). North Sea Ecosystem-Scale Model-Based Quantification of Net Primary Productivity Changes by the Benthic Filter Feeder Mytilus edulis. *Water*, *10*, 18 pp. doi: 10.3390/w10111527

Li, G., Gao, P., Wang, F., & Liang, Q. (2004). Estimation of ocean primary productivity and its spatio-temporal variation mechanism for East China Sea based on VGPM model. *Journal of Geographical Sciences*, *14*, 32-40. doi: 10.1007/BF02873088

Li, M., Peng, C., Wang, M., Xue, W., Zhang, K., Wang, K., ... Zhu, Q. (2017). The carbon flux of global rivers: A re-evaluation of amount and spatial patterns. *Ecological Indicators*, *80*, 40-51. doi: 10.1016/j.ecolind.2017.04.049

Li, M., Peng, C., Zhou, X., Yang, Y., Guo, Y., Shi, G., & Zhu, Q. (2019). Modeling Global Riverine DOC Flux Dynamics From 1951 to 2015. *Journal of Advances in Modeling Earth Systems*, *11*, 514-530. doi: 10.1029/2018MS001363

Li, Z., von Storch, J. S., & Müller, M. (2017). The K1 internal tide simulated by a 1/10° OGCM. *Ocean Modelling*, *113*, 145-156. doi: 10.1016/j.ocemod.2017.04.002

Lie, H. J., & Cho, C. H. (2016). Seasonal circulation patterns of the Yellow and East China Seas derived from satellite-tracked drifter trajectories and hydrographic observations. *Progress in Oceanography*, *146*, 121-141. doi: 10.1016/j.pocean.2016.06.004

Liu, F., Su, J., Moll, A., Krasemann, H., X. Chen, T. P., & Wirtz, K. (2014). Assessment of the summer-autumn bloom in the Bohai Sea using satellite images to identify the roles of wind mixing and light conditions. *Journal of Marine Systems*, *129*, 303-317. doi: 10.1016/j.jmarsys.2013.07.007

Liu, X., Dunne, J. P., Stock, C. A., Harrison, M. J., Adcroft, A., & Resplandy, L. (2019). Simulating Water Residence Time in the Coastal Ocean: A Global Perspective. *Geophysical Research Letters*, *46*, 13910-13919. doi: 10.1029/2019GL085097

Liu, Z., & Gan, J. (2016). Open boundary conditions for tidally and subtidally forced circulation in a limited-area coastal model using the Regional Ocean Modeling System (ROMS). *Journal of Geophysical Research: Oceans*, *121*, 6184-6203. doi: 10.1002/2016JC011975

Liu, Z., Gan, J., Hu, J., Wu, H., Cai, Z., & Deng, Y. (2021). Progress on circulation dynamics in the East China Sea and southern Yellow Sea: Origination, pathways, and destinations of shelf currents. *Progress in Oceanography*, *193*, 102553. doi: 10.1016/

j.pocean.2021.102553

Liu, Z., Zhang, W., Xiong, X., & Zhu, S. (2021). Observational characteristics and dynamic mechanism of low-salinity water lens for the offshore detachment of the Changjiang River diluted water in August 2006. *Acta Oceanologica Sinica*, *40*, 34-45. doi: 10.1007/s13131-021-1710-9

Locarnini, R. A., Mishonov, A. V., Antonov, J. I., Boyer, T. P., Garcia, H. E., Baranova, O. K., ... Seidov, D. (2013). World Ocean Atlas 2013, Volume 1: Temperature. *Levitus, S., Mishonov, A. (Eds.), NOAA Atlas NESDIS*, *73*, 40 pp.

Loebl, M., Colijn, F., van Beusekom, J. E. E., Baretta-Bekker, J. G., Lancelot, C., Philippart, C. J. M., ... Wiltshire, K. H. (2009). Recent patterns in potential phytoplankton limitation along the Northwest European continental coast. *Journal of Sea Research*, *61*, 34-43. doi: 10.1016/j.seares.2008.10.002

Logemann, K., Linardakis, L., Korn, P., & Schrum, C. (2021). Global tide simulations with ICON-O: testing the model performance on highly irregular meshes. *Ocean Dynamics*, *71*, 43-57. doi: 10.1007/s10236-020-01428-7

Lønborg, C., Álvarez Salgado, X. A., Letscher, R. T., & Hansell, D. A. (2018). Large Stimulation of Recalcitrant Dissolved Organic Carbon Degradation by Increasing Ocean Temperatures. *Front. Mar. Sci.*, *4*, 11 pp. doi: 10.3389/fmars.2017.00436

Luisetti, T., Ferrini, S., Grilli, G., Jickells, T. D., Kennedy, H., Kröger, S., ... Tyllianakis, E. (2020). Climate action requires new accounting guidance and governance frameworks to manage carbon in shelf seas. *Nature Communications*, *11*, 4599. doi: 10.1038/s41467-020-18242-w

Luo, X. (2014). Phytoplankton community and primary productivity in the Yellow Sea and East China Sea. In *Marine biodiversity and ecosystem dynamics of the northwest pacific ocean* (p. 13 pp). Science Press Beijing.

Maerz, J., Hofmeister, R., van der Lee, E. M., Gräwe, U., Riethmüller, R., & Wirtz, K. W. (2016). Maximum sinking velocities of suspended particulate matter in a coastal transition zone. *Biogeosciences*, *13*, 4863-4876. doi: 10.5194/bg-13-4863-2016

Maerz, J., Six, K. D., Stemmler, I., Ahmerkamp, S., & Ilyina, T. (2020). Microstructure and composition of marine aggregates as co-determinants for vertical particulate organic carbon transfer in the global ocean. *Biogeosciences*, *17*, 1765-1803. doi: 10.5194/bg-17-1765-2020

Maier-Reimer, E., Kriest, I., Segschneider, J., & Wetzel, P. (2005). The Hamburg Ocean Carbon Cycle Model HAMOCC5.1 - Technical Description Release 1.1. *Berichte zur Erdsystemforschung*, *14*, 50 pp. (Max Planck Institute for Meteorology, Hamburg, Germany)

Marrec, P., Cariou, T., Macé, E., Morin, P., Salt, L. A., Vernet, M., ... Bozec, Y. (2015). Dynamics of air-sea CO_2 fluxes in the northwestern European shelf based on voluntary observing ship and satellite observations. *Biogeosciences*, *12*, 5371-5391. doi: 10.5194/bg-12-5371-2015

Marsaleix, P., Auclair, F., & Estournel, C. (2006). Considerations on Open Boundary Conditions for Regional and Coastal Ocean Models. *Journal of Atmospheric and Oceanic Technology*, *23*, 1604-1613. doi: 10.1175/JTECH1930.1

Marsh, R., Haigh, I. D., Cunningham, S. A., Inall, M. E., Porter, M., & Moat, B. I. (2017). Large-scale forcing of the European Slope Current and associated inflows to the North Sea. *Ocean Science*, *13*, 315-335.

Mathis, M., Elizalde, A., & Mikolajewicz, U. (2018). Which complexity of regional climate system models is essential for downscaling anthropogenic climate change in the Northwest European Shelf? *Climate Dynamics*, *50*, 2637-2659.

Mathis, M., Elizalde, A., & Mikolajewicz, U. (2019). The future regime of Atlantic nutrient supply to the Northwest European Shelf. *J. Mar. Syst.*, *189*, 98-115. doi: 10.1016/j.jmarsys.2018.10.002

Mathis, M., Elizalde, A., Mikolajewicz, U., & Pohlmann, T. (2015). Variability patterns of the general circulation and sea water temperature in the North Sea. *Prog. Oceanog.*, *135*,

91-112.

Mathis, M., Mayer, B., & Pohlmann, T. (2013). An uncoupled dynamical downscaling for the North Sea: Method and evaluation. *Ocean Modelling*, *72*, 153-166.

Mauritsen, T., Bader, J., Becker, T., Behrens, J., Bittner, M., Brokopf, R., ... Roeckner, E. (2019). Developments in the MPI-M Earth System Model version 1.2 (MPI-ESM1.2) and its response to increasing CO_2. *Journal of Advances in Modeling Earth Systems*, *11*, 998-1038. doi: 10.1029/2018MS001400

Mayer, B., Rixen, T., & Pohlmann, T. (2018). The Spatial and Temporal Variability of Air-Sea CO_2 Fluxes and the Effect of Net Coral Reef Calcification in the Indonesian Seas: A Numerical Sensitivity Study. *Frontiers in Marine Science*, *5*, 19 pp. doi: 10.3389/fmars.2018.00116

Meybeck, M. (1982). Carbon, Nitrogen, and Phosphorus Transport by World Rivers. *Am. J. Sci.*, *282*, 401-450. doi: 10.2475/ajs.282.4.401

Meybeck, M., & Vörösmarty, C. (1999). Global Transfer of Carbon by Rivers. *Global Change Newsletters*, *IGBP Newsletter No. 37*, 18-19.

Middelburg, J. J., Soetaert, K., & Hagens, M. (2020). Ocean Alkalinity, Buffering and Biogeochemical Processes. *Reviews of Geophysics*, *58*, e2019RG000681. doi: 10.1029/2019RG000681

Moat, B. I., Frajka-Williams, E., Smeed, D., Rayner, D., Sanchez-Franks, A., Johns, W. E., ... Collins, J. (2020). Atlantic meridional overturning circulation observed by the RAPID-MOCHA-WBTS (RAPID-Meridional Overturning Circulation and Heatflux Array-Western Boundary Time Series) array at 26N from 2004 to 2018 (v2018.2). *British Oceanographic Data Centre, National Oceanography Centre, NERC, UK*. doi: 10/d3z4

Moll, A. (1998). Regional distribution of primary production in the North Sea simulated by a three-dimensional model. *Journal of Marine Systems*, *16*, 151-170.

Müller, W. A., Jungclaus, J. H., Mauritsen, T., Baehr, J., Bittner, M., Budich, R., ... Marotzke, J. (2018). A Higher-resolution Version of the Max Planck Institute Earth System Model (MPI-ESM1.2-HR). *Journal of Advances in Modeling Earth Systems*, *10*, 1383-1413. doi: 10.1029/2017MS001217

Muller-Karger, F. E., Varela, R., Thunell, R. C., Luerssen, R., Hu, C., & Walsh, J. J. (2005). The importance of continental margins in the global carbon cycle. *Geophys. Res. Letters*, *32*, L01602. doi: 10.1029/2004GL021346

Najjar, R. G., Jin, X., Louanchi, F., Aumont, O., Caldeira, K., Doney, S. C., ... Yool, A. (2007). Impact of circulation on export production, dissolved organic matter, and dissolved oxygen in the ocean: Results from Phase II of the Ocean Carbon-cycle Model Intercomparison Project (OCMIP-2). *Global Biogeochemical Cycles*, *21*, 22 p. doi: 10.1029/2006GB002857

Nellemann, C., Corcoran, E., Duarte, C., Valdes, L., Young, C., Fonseca, L., & Grimsditch, G. (2009). Blue Carbon - The Role of Healthy Oceans in Binding Carbon. *A Rapid Response Assessment. United Nations Environment Programme*.

Oguz, T., Macias, D., , & Tintore, J. (2015). Ageostrophic frontal processes controlling phytoplankton production in the Catalano-Balearic Sea (Western Mediterranean). *PLoS One*, *10*, 22 pp. doi: 10.1371/journal.pone.0129045

O'Meara, T., Gibbs, E., & Thrush, S. F. (2018). Rapid organic matter assay of organic matter degradation across depth gradients within marine sediments. *Methods Ecol. Evol.*, *9*, 245-253. doi: 10.1111/2041-210X.12894

Oschlies, A. (2008). Eddies and Upper-Ocean Nutrient Supply. *Geophysical Monograph Series*, *177*, 115-130. doi: 10.1029/177GM09

Pain, C. C., Piggott, M. D., Goddard, A. J. H., Fang, F., Gorman, G. J., Marshall, D. P., ... de Oliveira, C. R. E. (2005). Three-dimensional unstructured mesh ocean modelling. *Ocean Modelling*, *10*, 5-33. doi: 10.1016/j.ocemod.2004.07.005

Painter, S. C., Hartman, S. E., Kivimäe, C., Salt, L. A., Clargo, N. M., Bozec, Y., ... Allen, S. R. (2016). Carbon exchange between a shelf sea and the ocean: The Hebrides Shelf, west of Scotland. *Journal of Geophysical Research: Oceans*, *121*, 4522-4544. doi:

10.1002/2015JC011599

Painting, S. J., Collingridge, K. A., Durand, D., Grémare, A., Créach, V., Arvanitidis, C., & Bernard, G. (2020). Marine monitoring in Europe: is it adequate to addressenvironmental threats and pressures? *Ocean Sci.*, *16*, 235-252. doi: 10.5194/os-16-235-2020

Palastanga, V., Slomp, C. P., & Heinze, C. (2011). Long-term controls on ocean phosphorus and oxygen in a global biogeochemical model. *Global Biogeochemical Cycles*, *25*, 19 pp. doi: 10.1029/2010GB003827

Park, G. H., Wanninkhof, R., Doney, S. C., Takahashi, T., Lee, K., Feely, R. A., ... Lima, I. (2010). Variability of global air-sea CO2 fluxes over the last three decades. *Tellus*, *62B*, 352-368. doi: 10.1111/j.1600-0889.2010.00498.x

Pätsch, J., Burchard, H., Dieterich, C., Gräwe, U., Gröger, M., Mathis, M., ... Eden, C. (2017). An evaluation of the North Sea circulation in global and regional models relevant for ecosystem simulations. *Ocean Modelling*, *116*, 70-95. doi: 10.1016/j.ocemod.2017.06.005

Paulsen, H., Ilyina, T., Six, K. D., & Stemmler, I. (2017). Incorporating a prognostic representation of marine nitrogen fixers into the global ocean biogeochemical model HAMOCC. *Journal of Advances in Modeling Earth Systems*, *9*, 438-464. doi: 10.1002/2016MS000737

Piggott, M. D., Pain, C. C., Gorman, G. J., Marshall, D. P., & Killworth, P. D. (2008). Unstructured Adaptive Meshes for Ocean Modeling. In M. W. Hecht & H. Hasumi (Eds.), *Ocean modeling in an eddying regime* (p. 383-408). American Geophysical Union (AGU). doi: 10.1029/177GM22

Pimenta, F. M., Campos, E. J. D., Miller, J. L., & Piola, A. R. (2005). A numerical study of the Plata River plume along the southeastern South American continental shelf. *Braz. J. Oceanogr.*, *53*, 129-146.

Piola, A. R., Palma, E. D., Bianchi, A. A., Castro, B. M., Dottori, M., Guerrero, R. A., ... Saraceno, M. (2018). Physical Oceanography of the SW Atlantic Shelf: A Review. In M. Hoffmeyer, M. Sabatini, F. Brandini, D. Calliari, & S. N. (Eds.), *Plankton Ecology of the Southwestern Atlantic* (p. 37-56). Springer, Cham. doi: 10.1007/978-3-319-77869-3_2

Pipko, I. I., Pugach, S. P., Semiletov, I. P., Anderson, L. G., Shakhova, N. E., Gustafsson, O., ... Dudarev, O. V. (2017). The spatial and interannual dynamics of the surface water carbonate system and air-sea CO_2 fluxes in the outer shelf and slope of the Eurasian Arctic Ocean. *Ocean Science*, *13*, 997-1016. doi: 10.5194/os-13-997-2017

Poulain, P. M., & Centurioni, L. (2015). Direct measurements of World Ocean tidal currents with surface drifters. *J. Geophys. Res. Oceans*, *120*, 6986-7003. doi: 10.1002/2015JC010818

Pradal, M. A., & Gnanadesikan, A. (2014). How does the Redi parameter for mesoscale mixing impact global climate in an Earth System Model? *Journal of Advances in Modeling Earth Systems*, *6*, 586-601. doi: 10.1002/2013MS000273

Provoost, P., Braeckman, U., van Gansbeke, D., Moodley, L., Soetaert, K., Middelburg, J. J., & Vanaverbeke, J. (2013). Modelling benthic oxygen consumption and benthic-pelagic coupling at a shallow station in the southern North Sea. *Estuarine, Coastal and Shelf Science*, *120*, 1-11. doi: 10.1016/j.ecss.2013.01.008

Provoost, P., van Heuven, S., Soetaert, K., Laane, R. W. P. M., & Middelburg, J. J. (2010). Seasonal and long-term changes in pH in the Dutch coastal zone. *Biogeosciences*, *7*, 3869-3878. doi: 10.5194/bg-7-3869-2010

Quante, M., Colijn, F., Bakker, J. P., Härdtle, W., Heinrich, H., Lefebvre, C., ... Tölle, M. H. (2016). Introduction to the Assessment - Characteristics of the Region. In M. Quante & F. Colijn (Eds.), *North Sea Region Climate Change Assessment* (p. 175-217). Springer Berlin - Heidelberg.

Randelhoff, A., Holding, J., Janout, M., Sejr, M. K., Babin, M., Tremblay, J. E., & Alkire, M. B. (2020). Pan-Arctic Ocean Primary Production Constrained by Turbulent Nitrate Fluxes. *Frontiers in Marine Science*, *7*, 15 pp. doi: 10.3389/fmars.2020.00150

Regnier, P., Friedlingstein, P., Ciais, P., Mackenzie, F. T., Gruber, N., Janssens, I. A., ... Thullner, M. (2013). Anthropogenic perturbation of the carbon fluxes from land to ocean.

Nature Geoscience, *6*, 597-607. doi: 10.1038/ngeo1830

Remacle, J. F., & Lambrechts, J. (2018). Fast and robust mesh generation on the sphere - Application to coastal domains. *Computer-Aided Design*, *103*, 14-23. (25th International Meshing Roundtable Special Issue: Advances in Mesh Generation) doi: 10.1016/j.cad .2018.03.002

Resplandy, L., Keeling, R. F., Rödenbeck, C., Stephens, B. B., Khatiwala, S., Rodgers, K. B., ... Tans, P. P. (2018). Revision of global carbon fluxes based on a reassessment of oceanic and riverine carbon transport. *Nat. Geosci.*, *11*, 504-509. doi: 10.1038/ s41561-018-0151-3

Reynaud, J. Y., & Dalrymple, R. (2012). Shallow-Marine Tidal Deposits. In R. A. J. Davis & R. W. Dalrymple (Eds.), *Principles of tidal sedimentology* (p. 335-369). Springer Science and Business Media B. V. doi: 10.1007/978-94-007-0123-6_13

Richardson, K., & Bendtsen, J. (2019). Vertical distribution of phytoplankton and primary production in relation to nutricline depth in the open ocean. *Mar. Ecol. Progr. Ser.*, *620*, 33-46. doi: 10.3354/meps12960

Ridgwell, A. J., Watson, A. J., & Archer, D. E. (2002). Modeling the response of the oceanic Si inventory to perturbation, and consequences for atmospheric CO_2. *Global Biogeochemical Cycles*, *16*, 26 pp. doi: 10.1029/2002GB001877

Rippeth, T. P., Lincoln, B. J., Kennedy, H. A., Palmer, M. R., Sharples, J., & Williams, C. A. J. (2014). Impact of vertical mixing on sea surface pCO_2 in temperate seasonally stratified shelf seas. *J. Geophys. Res. Oceans*, *119*, 3868-3882. doi: 10.1002/ 2014JC010089

Roobaert, A., Laruelle, G. G., Landschützer, P., Gruber, N., Chou, L., & Regnier, P. (2019). The spatiotemporal dynamics of the sources and sinks of CO_2 in the global coastal ocean. *Global Biogeochemical Cycles*, *33*, 1693-1714. doi: 10.1029/2019GB006239

Schartau, M., Riethmüller, R., Flöser, G., van Beusekom, J. E. E., Krasemann, H., Hofmeister, R., & Wirtz, K. (2019). On the separation between inorganic and organic fractions of suspended matter in a marine coastal environment. *Progress in Oceanography*, *171*, 231-250. doi: 10.1016/j.pocean.2018.12.011

Schmidt, S., Neumann, B., Waweru, Y., Durussel, C., Unger, S., & Visbeck, M. (2017). SDG14 Conserve and Sustainably Use the Oceans, Seas and Marine Resources for Sustainable Development. In D. J. Griggs, M. Nilsson, A. Stevance, & D. McCollum (Eds.), *A guide to sdg interactions: from science to implementation* (p. 174-218). International Council for Science (ICSU), Paris. doi: 10.24948/2017.01

Séférian, R., Berthet, S., Yool, A., Palmiéri, J., Bopp, L., Tagliabue, A., ... Yamamoto, A. (2020). Tracking Improvement in Simulated Marine Biogeochemistry Between CMIP5 and CMIP6. *Curr. Clim. Change Rep.*, *6*, 95-119. doi: 10.1007/s40641-020-00160-0

Sein, D., Mikolajewicz, U., Gröger, M., Fast, I., Cabos, I., Pinto, J., ... Jacob, D. (2015). Regionally coupled atmosphere-ocean-sea ice-marine biogeochemistry model ROM. Part I: Description and validation. *J. Adv. Model. Earth Syst.*, *7*, 268-304.

Sein, D. V., Koldunov, N. V., Danilov, S., Wang, Q., Sidorenko, D., Fast, I., ... Jung, T. (2017). Ocean modeling on a mesh with resolution following the local Rossby radius. *Journal of Advances in Modeling Earth Systems*, *9*, 2601-2614. doi: 10.1002/2017MS001099

Seitzinger, S. P., Mayorga, E., Bouwman, A. F., Kroeze, C., Beusen, A. H. W., Billen, G., ... Harrison, J. A. (2010). Global river nutrient export: A scenario analysis of past and future trends. *Global Biogeochemical Cycles*, *24*, 16 pp. doi: 10.1029/2009GB003587

Silsbe, G. M., Behrenfeld, M. J., Halsey, K. H., Milligan, A. J., & Westberry, T. K. (2016). The CAFE model: A net production model for global ocean phytoplankton. *Global Biogeochemical Cycles*, *30*, 1756-1777. doi: GlobalBiogeochemicalCycles

Simmons, H. L., Jayne, S. R., St. Laurent, L. C., & Weaver, A. J. (2004). Tidally driven mixing in a numerical model of the ocean general circulation. *Ocean Modelling*, *6*, 245-263. doi: 10.1016/S1463-5003(03)00011-8

Six, K. D., & Maier-Reimer, E. (1996). Effects of plankton dynamics on seasonal carbon fluxes in an ocean general circulation model. *Global Biogeochem. Cycles*, *10*, 559-583.

Small, R., Campbell, T., Teixeira, J., Carniel, S., Smith, T., Dykes, J., ... Allard, R. (2011). Air-Sea Interaction in the Ligurian Sea: Assessment of a Coupled Ocean-Atmosphere Model Using In Situ Data from LASIE07. *Monthly Weather Review*, *139*, 1785-1808. doi: 10.1175/2010MWR3431.1

Song, J., Qu, B., Li, X., Yuan, H., Li, N., & Duan, L. (2018). Carbon sinks/sources in the Yellow and East China Seas - Air-sea interface exchange, dissolution in seawater, and burial in sediments. *Science China Earth Sciences*, *61*, 1583-1593. doi: 10.1007/s11430-017-9213-6

Stolpovsky, K., Dale, A. W., & Wallmann, K. (2015). Toward a parameterization of global-scale organic carbon mineralization kinetics in surface marine sediments. *Global Biogeochemical Cycles*, *29*, 812-829. doi: 10.1002/2015GB005087

Stuhne, G. R., & Peltier, W. R. (2009). An unstructured C-grid based method for 3-D global ocean dynamics: Free-surface formulations and tidal test cases. *Ocean Modelling*, *28*, 97-105. doi: 10.1016/j.ocemod.2008.11.005

Su, J., Tian, T., Krasemann, H., Schartau, M., & Wirtz, K. (2015). Response patterns of phytoplankton growth to variations in resuspension in the German Bight revealed by daily MERIS data in 2003 and 2004. *Oceanologia*, *57*, 328-341. doi: 10.1016/j.oceano.2015.06.001

Sündermann, J., & Pohlmann, T. (2011). A brief analysis of North Sea physics. *Oceanologia*, *53*(3), 663-689.

Takahashi, T., Sutherland, S. C., Wanninkhof, R., Sweeney, C., Feely, R. A., Chipman, D. W., ... de Baar, H. J. (2009). Climatological mean and decadal change in surface ocean pCO2, and net sea-air CO2 flux over the global oceans. *Deep Sea Research Part II: Topical Studies in Oceanography*, *56*, 554-577. doi: 10.1016/j.dsr2.2008.12.009

Tamburini, F., & Föllmi, K. B. (2009). Phosphorus burial in the ocean over glacial-interglacial time scales. *Biogeosciences*, *6*, 501-513. doi: 10.5194/bg-6-501-2009

Tan, S., & Shi, G. (2006). Satellite-derived primary productivity and its spatial and temporal variability in the China seas. *Journal of Geographical Sciences*, *16*, 447-457. doi: 10.1007/s11442-006-0408-4

Tan, S., & Shi, G. (2012). The relationship between satellite-derived primary production and vertical mixing and atmospheric inputs in the Yellow Sea cold water mass. *Continental Shelf Research*, *48*, 138-145. doi: 10.1016/j.csr.2012.07.015

Taylor, K., Stouffer, R. J., & Meehl, G. A. (2012). An overview of CMIP5 and the experiment design. *Bull. Am. Meteorol. Soc.*, *93*, 485-498. doi: 10.1175/BAMS-D-11-00094.1

Terhaar, J., Lauerwald, R., Regnier, P., Gruber, N., & Bopp, L. (2021). Around one third of current Arctic Ocean primary production sustained by rivers and coastal erosion. *Nature Communications*, *12*, 10 pp. doi: 10.1038/s41467-020-20470-z

Thévenin, M. R., Pereira, J., & Lessa, G. C. (2019). Shelf-break upwelling on a very narrow continental shelf adjacent to a western boundary current formation zone. *Journal of Marine Systems*, *194*, 52-65. doi: 10.1016/j.jmarsys.2019.02.008

Thomas, H., Bozec, Y., Elkalay, K., & de Baar, H. J. W. (2004). Enhanced Open Ocean Storage of CO_2 from Shelf Sea Pumping. *Science*, *304*(5673), 1005-1008.

Toffoli, A., & Bitner-Gregersen, E. M. (2017). Types of Ocean Surface Waves, Wave Classification. In J. Carlton, P. Jukes, & Y. Choo (Eds.), *Encyclopedia of maritime and offshore engineering* (p. 1-8). John Wiley & Sons, Ltd. doi: 10.1002/9781118476406.emoe077

Tréguer, P. J., & De La Rocha, C. L. (2013). The World Ocean Silica Cycle. *Annual Review of Marine Science*, *5*, 477-501. doi: 10.1146/annurev-marine-121211-172346

Tréguer, P. J., Sutton, J. N., Brzezinski, M., Charette, M. A., Devries, T., Dutkiewicz, S., ... Rouxel, O. (2021). Reviews and syntheses: The biogeochemical cycle of silicon in the modern ocean. *Biogeosciences*, *18*, 1269-1289. doi: 10.5194/bg-18-1269-2021

Tseng, C. M., Liu, K. K., Gong, G. C., Shen, P. Y., & Cai, W. J. (2011). CO_2 uptake in the East China Sea relying on Changjiang runoff is prone to change. *Geophysical Research Letters*, *38*, 6 pp. doi: 10.1029/2011GL049774

van Cappellen, P., Dixit, S., & van Beusekom, J. (2002). Biogenic silica dissolution in the oceans: Reconciling experimental and field-based dissolution rates. *Global Biogeochemical Cycles*, *16*, 10 pp. doi: 10.1029/2001GB001431

van Leeuwen, S., Tett, P., Mills, D., & van der Molen, J. (2015). Stratified and nonstratified areas in the North Sea: Long-term variability and biological and policy implications. *J. Geophys. Res. Oceans*, *120*, 4670-4686. doi: 10.1002/2014JC010485

Vantrepotte, V., Loisel, H., Dessailly, D., & Mériaux, X. (2012). Optical classification of contrasted coastal waters. *Remote Sensing of Environment*, *123*, 306-323. doi: 10.1016/j.rse.2012.03.004

Violante, R. A., Paterlini, C. M., Marcolini, S. I., Costa, I. P., Cavallotto, J. L., Laprida, C., ... Osterrieth, M. L. (2014). The Argentine continental shelf: Morphology, sediments, processes and evolution since the last glacial maximum. *Geological Society Memoir*, *41*, 55-68. doi: 10.1144/M41.6

Volk, T., & Hoffert, M. I. (1985). Ocean Carbon Pumps: Analysis of Relative Strengths and Efficiencies in Ocean-Driven Atmospheric CO_2 Changes. In E. Sundquist & W. Broecker (Eds.), *The carbon cycle and atmospheric co$_2$: Natural variations archean to present* (p. 99-110). American Geophysical Union (AGU). doi: 10.1029/GM032p0099

Wallmann, K. (2010). Phosphorus imbalance in the global ocean? *Global Biogeochem. Cycles*, *24*, 12 pp. doi: 10.1029/2009GB003643

Wang, S., Dieterich, C., Döscher, R., Höglund, A., Hordoir, R., Meier, H. E. M., ... Schimanke, S. (2015). Development and evaluation of a new regional coupled atmosphere-ocean model in the North Sea and Baltic Sea. *Tellus A*, *67*, 20 pp. doi: 10.3402/tellusa.v67.24284

Ward, N. D., Bianchi, T. S., Medeiros, P. M., Seidel, M., Richey, J. E., Keil, R. G., & Sawakuchi, H. O. (2017). Where Carbon Goes When Water Flows: Carbon Cycling across the Aquatic Continuum. *Frontiers in Marine Science*, *4*, 27 pp. doi: 10.3389/fmars.2017.00007

Ward, N. D., Megonigal, J. P., Bond-Lamberty, B., Bailey, V. L., Butman, D., Canuel, E. A., ... Windham-Myers, L. (2020). Representing the function and sensitivity of coastal interfaces in Earth system models. *Nature Communications*, *11*, 14 pp. doi: 10.1038/s41467-020-16236-2

Weber, T., Cram, J. A., Leung, S. W., DeVries, T., & Deutsch, C. (2016). Deep ocean nutrients imply large latitudinal variation. *PNAS*, *113*, 8606-8611. doi: 10.1073/pnas.1604414113

Weller, H., Browne, P., Budd, C., & Cullen, M. (2016). Mesh adaptation on the sphere using optimal transport and the numerical solution of a Monge-Ampère type equation. *Journal of Computational Physics*, *308*, 102-123. doi: 10.1016/j.jcp.2015.12.018

Westberry, T., Behrenfeld, M., Siegel, D., & Boss, E. (2008). Carbon-based primary productivity modeling with vertically resolved photoacclimation. *Glob.Biogeochem. Cycles*, *22*, GB2024. doi: 10.1029/2007GB003078

Williams, C., Sharples, J., Mahaffey, C., & Rippeth, T. (2013). Wind-driven nutrient pulses to the subsurface chlorophyll maximum in seasonally stratified shelf seas. *Geophysical Research Letters*, *40*, 1-6. doi: 10.1002/2013GL058171

Wilson, R. J., & Heath, M. R. (2019). Increasing turbidity in the North Sea during the 20th century due to changing wave climate. *Ocean Science*, *15*, 1615-1625. doi: 10.5194/os-15-1615-2019

Wu, H., Wu, T., Shen, J., & Zhu, J. (2018). Dynamics of the Changjiang River Plume. In X. S. Liang & Y. Zhang (Eds.), *Coastal Environment, Disaster, and Infrastructure - A Case Study of China's Coastline.* London, UK.

Wu, R., Lin, J., & Li, B. (2016). Spatial and Temporal Variability of Sea Surface Temperature in Eastern Marginal Seas of China. *Advances in Meteorology*, *2016*, 1-9. doi: 10.1155/2016/3820720

Xie, F., Tao, Z., Zhou, X., Lv, T., & Wang, J. (2019). Spatial and Temporal Variations of Particulate Organic Carbon Sinking Flux in Global Ocean from 2003 to 2018. *Remote*

Sens., *11*, 20 pp. doi: 10.3390/rs11242941

Xue, P., Malanotte-Rizzoli, P., Wei, J., & Eltahir, E. (2020). Coupled Ocean-Atmosphere Modeling Over the Maritime Continent: A Review. *Journal of Geophysical Research: Oceans*, *125*. doi: 10.1029/2019JC014978

Yang, S., Song, B., Ye, S., Laws, E., He, L., Li, J., ... Behling, H. (2019). Large-scale pollen distribution in marine surface sediments from the Bohai Sea, China: Insights into pollen provenance, transport, deposition, and coastal-shelf paleoenvironment. *Progress in Oceanography*, *178*, 17 pp. doi: 10.1016/j.pocean.2019.102183

Yang, S., Wang, Z., Dou, Y., & Shi, X. (2014). A review of sedimentation since the Last Glacial Maximum on the continental shelf of eastern China. *Geological Society, London, Memoirs*, *41*, 293-303. doi: 10.1144/M41.21

Yao, Z., He, R., Bao, X., Wu, D., & Song, J. (2012). M2 tidal dynamics in Bohai and Yellow Seas: a hybrid data assimilative modeling study. *Ocean Dynamics*, *62*, 753-769. doi: 10.1007/s10236-011-0517-1

Yasunaka, S., Murata, A., Watanabe, E., Chierici, M., Fransson, A., van Heuven, S., ... Wanninkhof, R. (2016). Mapping of the air-sea CO_2 flux in the Arctic Ocean and its adjacent seas: Basin-wide distribution and seasonal to interannual variability. *Polar Science*, *10*, 323-334. doi: 10.1016/j.polar.2016.03.006

Yasunaka, S., Siswanto, E., Olsen, A., Hoppema, M., Watanabe, E., Fransson, A., ... Mathis, J. T. (2018). Arctic Ocean CO_2 uptake: an improved multiyear estimate of the air-sea CO_2 flux incorporating chlorophyll *a* concentrations. *Biogeosciences*, *15*, 1643-1661. doi: 10.5194/bg-15-1643-2018

Yuan, D., Zhu, J., Li, C., & Hu, D. (2008). Cross-shelf circulation in the Yellow and East China Seas indicated by MODIS satellite observations. *Journal of Marine Systems*, *70*, 134-149. doi: 10.1016/j.jmarsys.2007.04.002

Yvon-Durocher, G., Caffrey, J. M., Cescatti, A., Dossena, M., del Giorgio, P., Gasol, J. M., ... Allen, A. P. (2012). Reconciling the temperature dependence of respiration across timescales and ecosystem types. *Nature*, *487*, 472-476. doi: 10.1038/nature11205

Zhang, W., & Wirtz, K. (2017). Mutual dependence between sedimentary organic carbon and infaunal macrobenthos resolved by mechanistic modeling. *Journal of Geophysical Research: Biogeosciences*, *122*, 2509-2526. doi: 10.1002/2017JG003909

Zhao, C., Daewel, U., & Schrum, C. (2019). Tidal impacts on primary production in the North Sea. *Earth Syst. Dynam.*, *10*, 287-317. doi: 10.5194/esd-10-287-2019

Zhou, Y., Evans, C., Chen, Y., Chang, K., & Martin, P. (2021). Extensive remineralization of peatland-derived dissolved organic carbon and acidification in the Sunda Shelf Sea, Southeast Asia. *Earth and Space Science Open Archive*, 67 pp. doi: 10.1002/essoar.10506636.1

Zhou, Z. X., Yu, R. C., Sun, C., Feng, M., & Zhou, M. J. (2019). Impacts of Changjiang River Discharge and Kuroshio Intrusion on the Diatom and Dinoflagellate Blooms in the East China Sea. *Journal of Geophysical Research: Oceans*, *124*, 5244-5257. doi: 10.1029/2019JC015158

Zhu, J., Wu, H., & Li, L. (2015). Hydrodynamics of the Changjiang Estuary and Adjacent Seas. In J. Zhang (Ed.), *Ecological continuum from the changjiang (yangtze river) watersheds to the east china sea continental margin* (p. 19-45). Springer International Publishing Switzerland. doi: 10.1007/978-3-319-16339-0_2

Zweng, M. M., Reagan, J. R., Antonov, J. I., Locarnini, R. A., Mishonov, A. V., Boyer, T. P., ... Biddle, M. M. (2013). World Ocean Atlas 2013, Volume 2: Salinity. *Levitus, S., Mishonov, A. (Eds.), NOAA Atlas NESDIS*, *74*, 39 pp.